

TABLE OF CONTENTS

	Page
INTRODUCTION	1
CHAPTER 1 CONTEXT, LITERATURE REVIEW, OBJECTIVES AND ORIGINALITIES OF RESEARCH	3
1.1 Context and literature review	3
1.1.1 Aero-Thermodynamic (AT) evolution.....	4
1.1.2 Chemical process	5
1.2 Objectives and originalities of research.....	9
1.2.1 Research objectives.....	9
1.2.2 Research originalities.....	9
CHAPTER 2 GOVERNING EQUATIONS AND NUMERICAL MODELING	11
2.1 Governing equations	11
2.1.1 Mathematical governing equations.....	11
2.1.2 Numerical governing equations in STAR-CCM+	14
2.2 Numerical modeling.....	26
2.2.1 HPT design and meshing	27
2.2.2 Computational fluid dynamic (CFD) and chemical modeling.....	32
CHAPTER 3 AERO-THERMODYNAMIC AND CHEMICAL PROCESS INTERACTIONS IN AN AXIAL HIGH PRESSURE TURBINE.....	39
3.1 Introduction.....	39
3.2 Aero-Thermodynamic and chemical process interactions in an axial high pressure turbine.....	41
3.2.1 Baseline 1D, 2D full HPT flow path calculation	42
3.2.2 Formation and distribution of NO _x and SO _x throughout of stator and rotor blade	47
3.2.3 Chemical effects on flow variation.....	51
3.2.4 Effect of 3D blade profile, radial spacing, and rotor speed combinations on the HPT performance	54
3.3 Conclusion	57
CHAPTER 4 EVALUATION OF THE RELATIONSHIP BETWEEN AERO-THERMODYNAMIC PROCESS AND OPERATIONAL PARAMETERS IN THE AXIAL HIGH PRESSURE TURBINE.....	59
4.1 Introduction.....	59
4.2 Aero-Thermodynamic losses in HPT.....	61
4.3 Evaluation of the relationship between aero-thermodynamic process and operational parameters.....	64
4.3.1 Influence of initial temperature field in cruise and take-off.....	65

4.3.2	Influence of rotor speed in two cases: operating cruise and maximum rotor speed.....	69
4.3.3	Effect of cooling at rotor blade.....	73
4.3.4	Non-uniformities of thermal field distribution in the spatial HPT	78
4.4	Conclusion	81
CHAPTER 5	3-D MODELING OF TRANSFORMATION OF AEROSOL POLLUTANTS IN THE HIGH PRESSURE TURBINE.....	83
5.1	Introduction.....	83
5.2	Evolution of N-, S-, O-, H- and C-containing gas species in the HPT	85
5.2.1	Evolution of nitrogen species.....	85
5.2.2	Evolution of sulfur species.....	88
5.2.3	Evolution of hydrogen, oxygen species and carbon oxides.....	90
5.3	Inadequacies of 1-D, 2-D and 3-D analyses on chemical change.....	93
5.4	Conclusion	100
	CONCLUSION AND RECOMMENDATIONS	103
	LIST OF BIBLIOGRAPHICAL REFERENCES.....	105

LIST OF TABLES

	Page
Table 2.1	Initial aero-thermodynamic conditions32
Table 2.2	Neutral gas species initial conditions.....32
Table 2.3	Chemical mechanism for the HPT34
Table 3.1	Inlet to exit comparisons of \overline{X}_{NO_x,SO_x}49
Table 4.1	Effects of initial temperature change, of rotor speed change and cooling system77
Table 5.1	Inlet to outlet comparisons of \overline{X}_k for 1-D estimations, X_k for 2-D solutions99
Table 5.2	Inlet to outlet comparisons of \overline{X}_k for 2-D simulation and \overline{X}_k for 3-D turbine calculations.....100

LIST OF FIGURES

	Page
Figure 1.1	Temperature and pressure evolution in the intra-engine of an aircraft engine Taken from Starik et al. (2002, p. 10) and Lukachko et al. (1998, p. 16163)....5
Figure 2.1	Decomposition schema for an interior face gradient17
Figure 2.2	Decomposition schema for a boundary face gradient.....18
Figure 2.3	Basic blade parameters (a) and beta- (b), theta- (c), thickness- (c) function of blade axial distance for rotor blade.....28
Figure 2.4	Fluid domain structure of one stator and two rotor blades (a), and HPT complete structure (b)29
Figure 2.5	Mesh structure of periodic surfaces (a) and appreciation of bad elements for improvement of the mesh quality (b)30
Figure 2.6	Four blocks to control the mesh quality at the LE, TE of stator and rotor30
Figure 2.7	Schema of the process for improving the mesh quality31
Figure 3.1	Temperature- (a1), pressure- (b1) and velocity- (c1) evolution and temperature- (a2), pressure- (b2) and velocity- (c2) value distribution in stator and rotor blades at the 50 % of the span43
Figure 3.2	The three-dimensional flow field in the end wall region Taken from Goldstein et al. (1988, p. 864).....44
Figure 3.3	Temperature, pressure and velocity evolution in the flow from the combustor exit to the HPT exit46
Figure 3.4	Baseline calculation results of \overline{X}_{NO_x}47
Figure 3.5	NO evolution (a) and NO value distribution (b) at the 50 % of the span48
Figure 3.6	Baseline calculation results of \overline{X}_{SO_x}50
Figure 3.7	Variation of the temperature as a function of the axial distance with and without chemical reactions51
Figure 3.8	Variation of the pressure as a function of the axial distance with and without chemical reactions.....52

Figure 3.9	Variation of the flow velocity as a function of the axial distance with and without chemical reactions	53
Figure 3.10	Temperature evolution at the 5 % (a), 50 % (b), and 95 % (c) of the span	54
Figure 3.11	Turbulent kinetic energy (TKE) evolution at the 5 % (a), 50 % (b), 95 % (c) of the span	55
Figure 3.12	X_{NO} distributions at 5 % (a), 50 % (b), and 95 % (c) of the span.....	55
Figure 3.13	Temperature evolution at 5 %, 50 %, and 95 % of the span.....	56
Figure 3.14	NO evolution at 5 %, 50 %, and 95 % of the span	57
Figure 4.1	Temperature and pressure evolutions in the HPT.....	62
Figure 4.2	Temperature, pressure and velocity evolution from the combustor exit to the HPT exit.....	63
Figure 4.3	Temperature evolutions in two cases of initial temperatures: cruise (1341K) (a) and take-off (1554.5 K) (b) at the 50% of the span	66
Figure 4.4	Temperature distributions (a, b) and temperature variations (c) in two cases of initial temperatures: cruise (1341K) and take-off (1554.5 K).....	67
Figure 4.5	Variations of the pressure as a function of the axial distance in two cases of initial temperatures: cruise (1341K) and take-off (1554.5 K).....	68
Figure 4.6	Variations of the velocity as a function of the axial distance in two cases of initial temperatures: cruise (1341K) and take-off (1554.5 K)	68
Figure 4.7	Turbulent kinetic energy (TKE) evolution in two cases of initial temperatures: cruise (1341K) and take - off (1554 K).....	69
Figure 4.8	Temperature distributions (a, b) and temperature variations (c) in two cases of rotor speed: 8500 rpm and maximum 15183 rpm.....	70
Figure 4.9	Pressure distributions (a, b) and pressure variations (c) in two cases of rotor speed: 8500 rpm and maximum 15183 rpm.....	71
Figure 4.10	Velocity distributions (a, b) and velocity variations (c) in two cases of rotor speed: 8500 rpm and maximum 15183 rpm.....	72
Figure 4.11	Temperature of rotor blade surfaces in two cases: no cooling (a) and cooling (b) at 870 K.....	73
Figure 4.12	Cooling effect on temperature field	74

Figure 4.13	Temperature variations as a function of the axial distance in two cases: cooling with rotor blade temperature at 870 K and without cooling	75
Figure 4.14	Pressure variations as a function of the axial distance in two cases: cooling with rotor blade temperature at 870 K and without cooling	76
Figure 4.15	Isovalues of thermic field in the turbine following four zones: 1341.1 K-1200 K (a), 1200 K- 1100 K (b), 1100 K- 1000 K (c) and 843.13 K- 1000 K (d)	79
Figure 4.16	Simple model predicted (Eq. 4.5) of temperature isovalue line along the rotor pressure surface	80
Figure 5.1	Temperature, pressure and velocity evolution from the combustor exit to the HPT exit	85
Figure 5.2	N-containing gas species mole fractions (nitric oxides and nitric acids) at the 50% span	87
Figure 5.3	Baseline calculation results of \overline{X}_{NO_x}	88
Figure 5.4	S-containing oxide gas species mole fractions ((a), (b) and (c)) at the 50% span	89
Figure 5.5	Baseline calculation results of \overline{X}_{SO_x}	90
Figure 5.6	O-, H- and C-containing gas species mole fractions at the 50% span	91
Figure 5.7	Baseline calculation results of \overline{X}_{CO} , \overline{X}_{OH} , \overline{X}_{H_2O} , \overline{X}_{H_2} and \overline{X}_{N_2}	92
Figure 5.8	Generalized trends of gas species in the HPT	93
Figure 5.9	X_{CO_2} distributions of 1-D estimation and 2-D solutions at the 50 % span	95
Figure 5.10	X_{CO_2} distributions at the 5 % (a), 50 % (b), and 95 % (c) span	95
Figure 5.11	CO_2 evolution at the 5 %, 50 %, and 95 % span	96
Figure 5.12	NO evolutions at the 5 %, 50 %, and 95 % span	96
Figure 5.13	HNO_3 evolution at the 5 %, 50 %, and 95 % span	97
Figure 5.14	SO_2 evolution at the 5 %, 50 %, and 95 % span	97

XVIII

Figure 5.15 SO_3 evolution at the 5 %, 50 %, and 95 % span98

Figure 5.16 OH evolution at the 5 %, 50 %, and 95 % span.....98

LIST OF ABBREVIATIONS

2D/3D	Two/Three Dimensional
AT	Aero-Thermodynamic
CFD	Computational Fluid Dynamic
Fig.	Figure
HPT	High Pressure Turbine
IPCC	The Intergovernmental Panel on Climate Change
LE	Leading Edge
Q1D	Quasi One-Dimensional
TE	Trailing Edge
TKE	Turbulent Kinetic Energy
UHC	Unburned Hydrocarbon
<i>Atm</i>	Atmospheric conditions
Eq.	Equation

LIST OF SYMBOLS

C	Length of chord
P	Pressure
P_{inlet}	Pressure at the HPT inlet
P_{outlet}	Pressure at the HPT outlet
P_{static}	Static pressure
P_{total}	Total pressure
$P(x)$	Pressure as a function of the axial distance
$\bar{P}(x)$	Average pressure as a function of the axial distance
R	Radius
S	Pitch of blades
S / C	Ratio of chord
T	Temperature
T_c	Temperature of the cooling air
T_g	Temperature of the hot gas stream
T_{hub}	Temperature at hub surface
T_{inlet}	Temperature at the HPT inlet
T_{iso}	Temperature of isovalue
T_m	Temperature of rotor blade
T_{outlet}	Temperature at the HPT outlet
T_{tip}	Temperature at tip surface

T_{total}	Total temperature
$T(x)$	Temperature as a function of the axial distance
$T(x), \bar{T}(x)$	Temperature/ Average temperature as a function of the axial distance
V	Velocity
V_{inlet}	Velocity at the HPT inlet
V_{outlet}	Velocity at the HPT outlet
$V(x)$	Velocity as a function of the axial distance
$\bar{V}(x)$	Average velocity as a function of the axial distance
W_z	Axial velocity
X_k	Mole fraction of specie k
\bar{X}_k	Average mole fraction of specie k
δ	Radial displacement of streak temperature
Ω	Rotational speed
η	Cooling effectiveness
ϕ	Flow coefficient
ζ	Enthalpy loss coefficient

INTRODUCTION

Aeronautics contribute to climate change and degradation of air quality around airports through its emissions of greenhouse gases (CO_2 , water vapor), pollutant gaseous and its particulate emissions (soot, organic aerosols ...). In addition, fuels from this transportation sector are mainly fossil fuels. The environmental situation as well as the fear of a future fossil fuel shortage push many researchers to study the reduction of pollutant emissions and use of alternative renewable fuels. In this context, numerous studies are carried out on turbomachines, completed mainly by modeling and numerical simulations for a better understanding aerothermodynamic and chemical transformations. It is recognized that today less carbon monoxide (CO) and less unburned hydrocarbons (UHC) are produced; however, aircraft engines emit nitrogen oxides (NO_x), sulfur oxides (SO_x) (responsible of acid rain, smog and respiratory disorders) as well as soot (suspected to be carcinogenic) in greater quantity [1-3]. Different systems have been developed to reduce the latter pollutants (NO_x , SO_x and soot) as well as developments in combustor and turbine technology. However, the future concerning reduction of emissions from engines is more a matter of understanding physico-chemical processes using technologies or developing new fuels. At this level, modeling and simulation of physico-chemical evolutions and turbulence in the high pressure turbine (HPT) seem to be a feasible option, which justifies this project.

The study aims to improve knowledge of aero-thermodynamic process in different operational conditions of engine, interactions of aero-thermodynamic and chemical process, and the formation and transformation of aerosol precursors (pollutant gases and particles) in aircraft engines. The prediction of engine performance and pollutant species by numerical modeling for realistic aeronautical engine configurations is a challenge whose importance will increase in the next years. The main objective is to develop numerical models allowing to evaluate the aerothermodynamic and chemical processes relating to the transformation of the pollutant species in different operations of the high pressure turbine of aircraft engine. In particular, the main studied pollutants that have an impact on the environment are NO_x , SO_x , soot particles and aerosols.

To achieve this goal, the specific objectives of the project are established:

- model and simulate the operation of the turbine and interactions of aerothermodynamic and chemical processes in the HPT,
- analyze the aerothermodynamic process in the different operational conditions,
- quantify pollutant emissions according to the chemical kinetic models used.

In this research, we bring new insights about 3D design of the HPT, dissimilarities of aerothermodynamic and chemical transformations for multi-rows turbine (stator-rotor), as functions of operational parameters. We also investigate the evaluation of the effects of 3D geometry, rotation speed as well as cooling systems on the behavior of the flow by using the turbulence modeling strategy RANS. In order to achieve these goals, our design process as follows: i) the HPT conception of gas turbine is performed by the module BLADE GEN, ii) the STAR-CCM+ (CD-ADAPCO) software is used to model and simulate the processes, and iii) the results are executed and analyzed with an in-house Matlab routine, and compared with that reported in the literature.

CHAPTER 1

CONTEXT, LITERATURE REVIEW, OBJECTIVES AND ORIGINALITIES OF RESEARCH

1.1 Context and literature review

To understand the works that has already been done in the literature and theirs related results and to be able to give ideas and original methods, a literature review on these topics is presented in this chapter.

In this context, the synthesis reports of 1999, 2001 and more recent ones of 2007, prepared by the IPCC (the Intergovernmental Panel on Climate Change) have shown that the real effect of aeronautics on the climate could potentially be 2 to 3 times higher than that estimated from the greenhouse effect of the CO₂ emitted.

Nevertheless, the current estimations contain very important uncertainties, which reach nearly 50% of the values presented in various international works according to the IPCC reports. These uncertainties are mainly due to the lack of knowledge about the mechanisms of formation of pollutants emitted by aviation (NO_x, SO_x, soot, aerosols ...) and the influences of the flow during this process. A large number of approaches for reducing the environmental impact as well as increasing the engine performance that the aviation industry has been proposed. In this context, many researchers attempted to investigate the aero-thermodynamic and chemical processes in the combustor and the nozzle. However, the studies on the turbine components are very scarce due to various reasons : i) complex geometry of multi-row turbomachinery; ii) influences of rotor speed and cooling systems; iii) complex chemical kinetic moduls at high temperature and pressure, and iv) expensive cost of 3D modeling to simultaneously simulate the aero-thermodynamic and chemical processes in this part of the aircraft engine.

1.1.1 Aero-Thermodynamic (AT) evolution

The aero-thermodynamic process in the aircraft engine is a complex process and depends on initial conditions (temperature, pressure, velocity and turbulence), boundary conditions near wall surfaces (cooling systems...), operational function parameters (initial temperature field, rotor speed...), and blade geometry profile. Recent works have addressed this problem but they are mainly based on theoretical calculations or numerical calculations 1D or 2D but very few of them in 3D.

Starik et al. [4] and Lukachko et al. [5, 6] directly used results from AT process experiments (see Fig.1.1) to calculate the evolution of chemical species by 1D and 2D calculations. Fig. 1.1 shows a 1D diagram of the simple gradient of temperature and pressure in the intra-engine of an aircraft engine; it is considered that in the HPT, temperature and pressure have a negative gradient, linked to the losses in HPT which will be discussed in the next chapters. Rose et al. [7] realized 2D calculations using URANS method to study AT process in a rotor row axial turbine. Nevertheless, the effect of multi-rows (stator-rotor), 3D geometry and operational functions of the HPT has not been discussed. For 3D simulations, Lampart et al. [8] calculated the AT parameters in 3D flow of a turbine. The authors modified the blade profiles to increase the flow efficiency. However, the research was studied with a small blade number (3 stator and rotor blades), the cooling effects and operational function influences were still not discussed. Concerning experiments, Yilmaz et al. [9] estimated the relation between exhaust gas temperature and operational parameters in the CFM 56 engine, and Wey et al. (APEX project) [10, 11] measured the emissions and temperature of exhaust gases as a function of operational conditions. However, the AT process of intra-engine was not considered.

It is necessary to have a complete vision about AT process, based on 3D calculations at different operational conditions that will be highlighted in this thesis research.

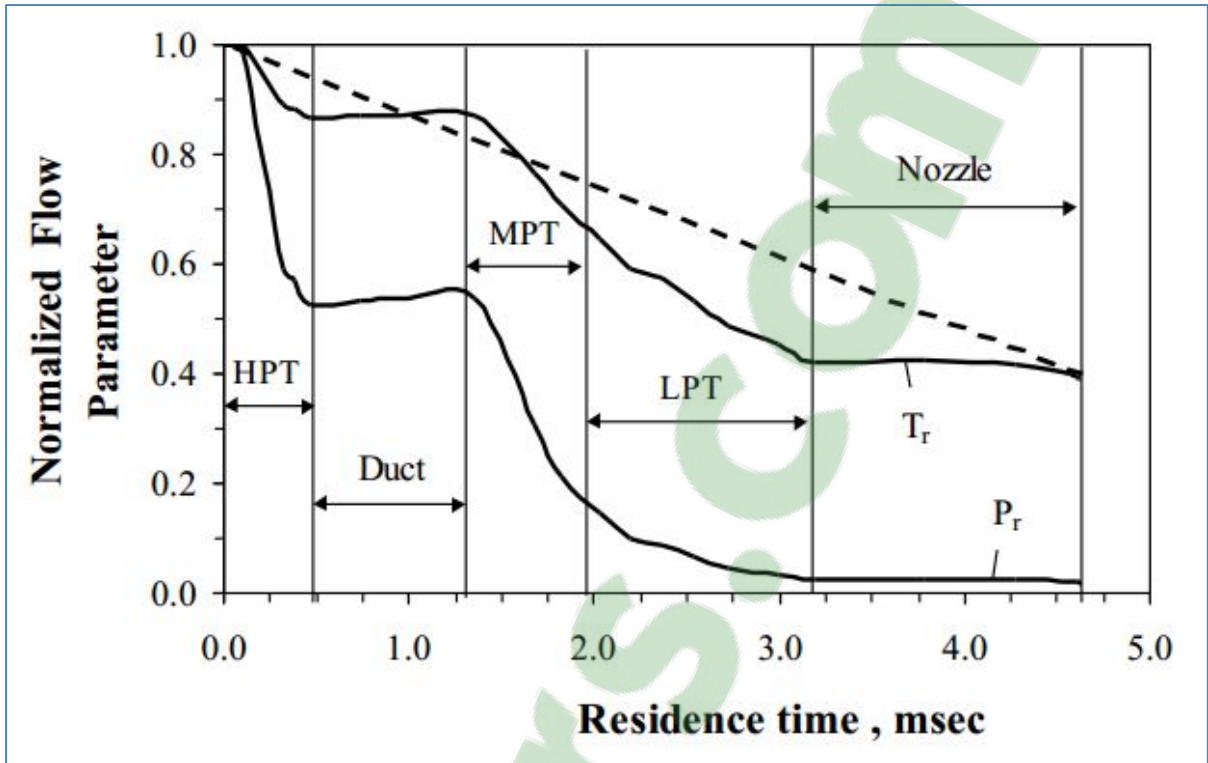


Figure 1.1 Temperature and pressure evolution in the intra-engine of an aircraft engine
Taken from Starik et al. (2002, p. 10) and Lukachko et al. (1998, p. 16163)

1.1.2 Chemical process

The investigation of chemical process in the HPT contains a big challenge because of the complexity of kinetic chemistry in the 3D complex flow, relating to the moving blade at high temperature and high pressure. Similar to the AT process, there is a limited works on the 3D numerical calculations by computer simulation.

In this context, for 0D, quasi-1D (Q1D) and 1D simulations, some authors : Moniruzzaman [12], Bisson [13] and Starik [4, 14] used one of these simulations to study the chemical process in a HPT. These authors argued and explained the transformations of aerosol precursors and particles in post-combustor (turbine and nozzle). Nevertheless, the HPT was replaced by a reactor; this means that the effects of 3D flow, multi-row turbomachinery and

source term of rotation of rotor were still not considered. For 1D and 2D simulations, Lukachko et al. [5, 6] calculated the evolutions of chemical species in a row of blade with a chemical package at high temperature and pressure. However, the authors simulated this process in a single blade row. Therefore, the influences of multi-rows, moving blade and dissimilarly of evolution of species in 3D flows have not been performed.

To better understand the formation and the transformation of pollutants, most studies have focused on the principal gas aerosol precursors and soot particles, described as follows:

- Unburned hydrocarbons (UHC)

The existence of UHC (CH_4 , R-OH ...) is due to an incomplete combustion relating to a short resident time, locals lacked oxygen (rich zones) and a low temperature, reducing chemical kinetics. To more complete combustion and reduce emissions, the increase of oxygen, presented in the fuels, would be indispensable. It is also observed that the increase of temperature in the engine can decrease CO and UHC [15].

According to the IPCC, the UHC aviation emission is one of principal sources from the worldwide transport. In this research, UHC evolutions will be considered from the initial conditions to the transformation in the HPT.

- Nitrogen oxides

The family of nitrogen oxides includes the following compounds: nitrogen monoxide (NO), nitrogen dioxide (NO_2), nitrous oxide (N_2O), dinitrogen tetroxide (N_2O_4), dinitrogen trioxide (N_2O_3). Among them, the main toxic gases are the NO and the NO_2 (grouped under NO_x), two odorous and toxic gases with low dose; mucosal irritation begins as soon as their content (by volume) exceeds 0.0013%. In atmospheric chemistry, NO_x gases play an important role in the formation of smog, producing the brown haze often observed over cities, particularly during the summer time (during high-temperature), more environmental problems are caused by NO_x pollution. In the presence of rain, nitrogen oxides form nitric acid, contributing to the

acid rain problem. Additionally, NO_x deposition in the oceans provides phytoplankton with nutrients, worsening the problem of red tides and other harmful algae blooms. Today, NO_x is emitted in a large quantity by transport and industry.

The production of the nitrogen oxides takes place at high temperatures. Four main methods have been identified to reduce NO_x emissions: i) reducing residence time, ii) increasing dilution, iii) using cleaner fuels and iv) improving fuel injection [15]. In the HPT, these processes may occur at high temperature and high dilution relating moving blade. Thus, understanding NO_x transformation is crucial in the NO_x evolution in the intra-engine.

- Sulfur oxides

There are more than 30 sulfur oxides (S_nO_m) of which two common sulfur compounds are sulfur dioxide (SO_2) and sulfur trioxide (SO_3). The most common sulfur oxide is sulfur dioxide; sulfur trioxide is an intermediate product during the manufacture of sulfuric acid. Sulfur dioxide is a colorless gas with a penetrating, choking odor. Excessive exposure to sulfur dioxide may cause health effects on the eye, lung and throat. Sulphur dioxide is toxic to a variety of plants and may produce visible signs of injury and/or reduce yields of certain crops. Sulfur dioxide gas dissolves in the water droplets in clouds causing the rain to be more acidic than usual. The main emission source of sulfur dioxide is the burning of fossil fuels. Transport vehicles and domestic boilers, as well as natural sources such as active volcanoes and forest fires, release sulfur dioxide. Concerning the air transport, the gas continues to increase in the stratosphere because of the intensification of this type of transport [1]. It is clear that the sulfur oxide emissions depend on the chemical reactions taking place in the engine [16].

It is now realized that sulfur compounds travel long distances in the upper atmosphere and can cause damage far from the original source. Therefore the objective must be to reduce total emissions.

- Particles

Particulate Matter (PM) emitted by aeronautical engines includes the organic soluble fraction as well as the insoluble fraction that mainly comprises soot. The soot is a set of chemical compounds, resulting from the incomplete combustion of fossil fuels (gasoline, diesel, fuel oil, kerosene, coal) or biomass (wood, plants). The soot is in the form of solid or tarry substance having blackish appearance. The soot particles emitted by incomplete combustions are composed of elemental carbon (EC), also called carbon black (CB), present in the form of graphite microcrystals, and organic compounds (called OC: organic carbon) [17]. In the exhaust gas, the soot is fine particulate matters with diameter less than 1 μm [18]. The tiny particles are able to travel deeply into the respiratory tract, reaching the lungs. Exposure to fine particles can cause short-term health effects such as eye, nose, throat and lung irritation, coughing, sneezing, runny nose and shortness of breath. Studies also suggest that long term exposure to fine particulate matter may be associated with increased rates of chronic bronchitis, reduced lung function and increased mortality from lung cancer and heart disease. The studies also shows that while carbon dioxide may be the No.1 contributor to rising global temperatures, black carbon has emerged as an important No.2.

In the intra-engine, it is demonstrated that the formation of soot strongly depends on the variation of temperature and dilution ratio. This formation also depends on the oxygen presence in the combustion which promotes rather the oxidation of soot than its formation [17].

The formation and transformation of soot particles, nitrogen oxides, sulfur oxides and other chemical species in the HPT relating to moving blade at high temperature and pressure are complex processes. In this research, the soot evolution is presented generally; evolution of O-, H-, C-containing gas species and gas pollutants such as nitrogen, sulfur compounds are investigated in detail.

1.2 Objectives and originalities of research

1.2.1 Research objectives

The study aims to improve knowledge of aero-thermodynamic process in different operational conditions of engine, interactions of aero-thermodynamic and chemical process, as well as the formation and transformation of aerosol precursors (pollutant gases and particles) in aircraft engines. The prediction of engine performance and pollutant species by numerical modeling for realistic aeronautical engine configurations is a big challenge and becomes more important in the next decades. The main objective is to develop numerical models allowing to evaluate the aerothermodynamic and chemical processes relating to the transformation of the pollutant species in different operations of the high pressure turbine of aircraft engines. In particular, the main studied pollutants that have an impact on the environment are NO_x , SO_x , soot particles and aerosols.

To achieve this goal, the specific objectives of the project are:

- model and simulate the operation of the turbine and interactions of aero-thermodynamic and chemical processes in the HPT,
- analyze the aero-thermodynamic process in the different operational functions,
- quantify pollutant emissions according to the chemical kinetic models used.

1.2.2 Research originalities

In the assessment of the current state-of-the-art presented and the reminder of project objectives, it is possible to demonstrate the originalities of this research.

First of all, we present here, for the first time, the designs, the computer simulations, the tridimensional calculations (3D CFD) of the interactions of AT parameters under various operational conditions of an aircraft engine by using refined mesh system and using more than one million iterations to solve equations in the HPT. Our research provides also an

overview of high resolution topographic images of the distribution of AT parameters in a multi-row turbomachinery.

Secondly, this work brings, for the first time, new insights into the study of aerothermodynamic processes, formation of nitrate and sulfate aerosols, and investigates the influences of chemical processes on aero-thermodynamic. We also shed light on effect of 3D blade profile, radial spacing, and rotor speed on the performance of the HPT.

Finally, this study provides precise investigation of chemical process in the turbine which is now challenging because of the complexity of transformation process in complex flows relating to the moving blade at high temperature and high pressure. We show here, this is the first published model on studying of 3D chemical formations inside a HPT and for the first time, to able to compare three numerical solutions (1D, 2D and 3D calculations) of transformation of trace species inside an aircraft engine.

The main results of these important works will be presented in detail in the next chapters of this thesis.

CHAPTER 2

GOVERNING EQUATIONS AND NUMERICAL MODELING

2.1 Governing equations

2.1.1 Mathematical governing equations

To solve governing equations, the RANS approach (Reynolds-Averaged Navier-Stokes equations) and the $k - \varepsilon$ model (two equations) were used in the STAR-CCM+ code because of its advantages of robustness, computational cost and accuracy.

The turbulence models seek to solve a modified set of transport equations by introducing averaged and fluctuating components. For example, a velocity U_i may be divided into an average component, $\overline{U_i}$, and a time varying component, u_i : $U_i = \overline{U_i} + u_i$. For compressible flows, the averaging is actually weighted by density (Favre-averaging), but for the sake of simplicity, the following equations are written:

The governing equations of continuity and momentum are described below in three dimensions (x, y, z) [18, 19]:

$$\frac{\partial \rho}{\partial t} + \frac{\partial}{\partial x_j} (\rho U_j) = 0 \quad (2.1)$$

$$\frac{\partial \rho U_i}{\partial t} + \frac{\partial}{\partial x_j} (\rho U_i U_j) = -\frac{\partial p}{\partial x_i} + \frac{\partial}{\partial x_j} (\tau_{ij} - \overline{\rho u_i u_j}) + S_M \quad (2.2)$$

where τ is the molecular stress tensor (including both normal and shear components of the stress); $\overline{\rho u_i u_j}$ is the source term of the rotor speed, for a N_b - blade rotor, the rotor source term to be added to the discretized momentum equation is:

$$S_M = \frac{N_b \Delta \varphi}{2\pi} (-F) \quad (2.3)$$

where, $\Delta\varphi$ is the distance that a blade would travel while traversing through a control volume and \overline{F} is the instantaneous force acting on that control volume, which depends on the velocity field. The source term is averaged over 2π to account for the fact that the rotor has been modeled [20, 21]. The term $\frac{\partial}{\partial x_j}(\tau_{ij} - \rho \overline{u_i u_j})$ represents the work due to viscous stresses, referred to as the viscous work term is small, and is negligible in the present work [22-27].

The Reynolds averaged energy equation is:

$$\frac{\partial \rho h_{tot}}{\partial t} - \frac{\partial p}{\partial t} + \frac{\partial}{\partial x_j}(\rho U_j h_{tot}) = \frac{\partial}{\partial x_j} \left(\lambda \frac{\partial T}{\partial x_j} \right) + \frac{\partial}{\partial x_j} \left[U_j (\tau_{ij} - \rho \overline{u_i u_j}) \right] \quad (2.4)$$

where h_{tot} is the total enthalpy, related to the static enthalpy $h(T, p)$ by:

$$h_{tot} = h + \frac{1}{2} U_j U_j \quad (2.5)$$

Similarly, the additional variable Φ (temperature, pressure) may be divided into an average component, $\overline{\Phi}$, and a time varying component, φ . After dropping the bar for averaged quantities, except for products of fluctuating quantities, the additional variable equation becomes

$$\frac{\partial \rho \Phi}{\partial t} + \frac{\partial}{\partial x_j}(\rho U_j \Phi) = \frac{\partial}{\partial x_j} \left(\Gamma \frac{\partial \Phi}{\partial x_j} - \rho \overline{u_j \varphi} \right) + S_\Phi \quad (2.6)$$

where $\overline{\rho u_j \varphi}$ is the Reynol flux.

In the cases with chemical reactions, the equation of transport for component i with mass fraction Y_i is then:

$$\frac{\partial \rho Y_i}{\partial t} + \frac{\partial}{\partial x_j} (\rho U_j Y_i) = \frac{\partial}{\partial x_j} \left(\Gamma_{ieff} \frac{\partial Y_i}{\partial x_j} \right) + S_i \quad (2.7)$$

where

$$\Gamma_{ieff} = \Gamma_i + \frac{\mu_t}{Sc_i} \quad (2.8)$$

Γ_i is the molecular diffusion coefficient, Sc_i is the turbulent Schmidt number, S_i , for component i can be computed as the sum of the rate of progress for all the elementary reactions in which component i participates.

The conservation of energy equation for multicomponent fluids is expressed as:

$$\frac{\partial \rho H}{\partial t} - \frac{\partial p}{\partial t} + \frac{\partial}{\partial x_j} (\rho U_j H) = \frac{\partial}{\partial x_j} \left(\lambda \frac{\partial T}{\partial x_j} + \sum_i^{N_c} \Gamma_i h_i \frac{\partial Y_i}{\partial x_j} + \frac{\mu_t}{Pr_t} \frac{\partial h}{\partial x_j} \right) + S_E \quad (2.9)$$

where H, h are the total enthalpy and static enthalpy $h(T, p, Y_i)$ of species i , respectively;

N_c is the total number of components; Pr_t is turbulent Prandtl number; S_E is the energy source term due to chemical reaction determined by:

$$S_E = - \sum_i \frac{h_i^\circ}{M_i} R_i \quad (2.10)$$

where h_i° is the enthalpy of formation of species i and R_i is the volumetric rate of creation of species i .

2.1.2 Numerical governing equations in STAR-CCM+

2.1.2.1 Transport equations

The Navier-Stokes equations in Star-CCM+ for steady state with the finite volume method are presented in following form:

The equation

$$\sum_f [\rho\phi(u \cdot \mathbf{a} - G)]_f = \sum_f (\Gamma \nabla \phi \cdot \mathbf{a})_f + (S_\phi V)_0 \quad (2.11)$$

represents the transport of a scalar quantity ϕ to a cell-centered control volume for cell-0 where Γ , $\nabla \phi$ and \mathbf{a} represent the face diffusivity, gradient, and area vector, respectively G is the grid flux that is computed from the mesh motion as in Eq.2.12:

$$G = u_g \cdot \mathbf{a}_f \quad (2.12)$$

where u_g is the grid velocity and \mathbf{a}_f is the face area.

While the scalar quantity ϕ in a continuum, Eq.2.11 is written in a integral equation:

$$\int_A \rho\phi(u - u_g) \cdot d\mathbf{a} = \int_A \Gamma \nabla \phi \cdot d\mathbf{a} + \int_V S_\phi dV \quad (2.13)$$

where u_g is cell velocity.

The terms in the Eq.2.11 are, from left to right, the convective flux, the diffusive flux, and the volumetric source term.

The following sections describe the approximations that are employed when writing each term of this discrete equation as functions of the cell variables.

2.1.2.2 Convection, diffusion and source terms

Convection Term

The convective term at a face is discretized as follows:

$$[\phi \rho(\mathbf{u} \cdot \mathbf{a} - G)]_f = (\dot{m} \phi)_f = \dot{m}_f \phi_f \quad (2.14)$$

where ϕ_f and \dot{m}_f are the scalar values and mass flow rates at the face, respectively.

The manner in which the face value ϕ_f is computed from the cell values has a profound effect on the stability and accuracy of the numerical scheme. Several schemes which are commonly used are First-Order Upwind, Second-Order Upwind and Central-Differencing. In this research, we use Second-Order Upwind for the convection term because of the accuracy of this scheme in comparison with First-Order Upwind and more convergence for RANS approach and for the flow in the HPT in comparison with Central-Differencing scheme.

For a second-order upwind scheme, the convective flux is computed as:

$$(\dot{m} \phi)_f = \begin{cases} \dot{m}_f \phi_{f,0} & \text{for } \dot{m}_f \geq 0 \\ \dot{m}_f \phi_{f,1} & \text{for } \dot{m}_f < 0 \end{cases} \quad (2.15)$$

where the face values $\phi_{f,0}$ and $\phi_{f,1}$, are linearly interpolated from the cell values on either side of the face as follows:

$$\phi_{f,0} = \phi_0 + \mathbf{s}_0 \cdot (\Delta \phi)_{r,0} \quad (2.16)$$

$$\phi_{f,1} = \phi_1 + \mathbf{s}_1 \cdot (\Delta \phi)_{r,1} \quad (2.17)$$

where:

$$\mathbf{s}_0 = \mathbf{x}_f - \mathbf{x}_0 \quad (2.18)$$

$$\mathbf{s}_1 = \mathbf{x}_f - \mathbf{x}_1 \quad (2.19)$$

and $(\Delta\phi)_{r,0}$ and $(\Delta\phi)_{r,1}$ are the limited reconstruction gradients in cells 0 and 1, respectively.

The advantage of this scheme over the First-Order Upwind is that it is nominally second-order accurate. However, the fact that the reconstruction gradients are limited helps to reduce local extrema and thus introduces more dissipation than a Central-Differencing scheme. Clearly, the accuracy of this scheme is always as good or better than the First-Order Upwind scheme. The downside is that, in some situations, the reduced numerical dissipation can result in poorer convergence properties than a first-order convection. Generally, the poorer convergence is an acceptable trade-off.

Diffusion Term

Let D_f be the discrete form of the diffusion term:

$$D_f = \sum_f (\Gamma \nabla \phi \cdot \mathbf{a})_f \quad (2.20)$$

where Γ , $\nabla \phi$ and \mathbf{a} represent the face diffusivity, gradient, and area vector, respectively.

Interior Face

To obtain an accurate second-order expression for an interior face gradient that implicitly involves the cell values ϕ_0 and ϕ_1 , the following decomposition is used:

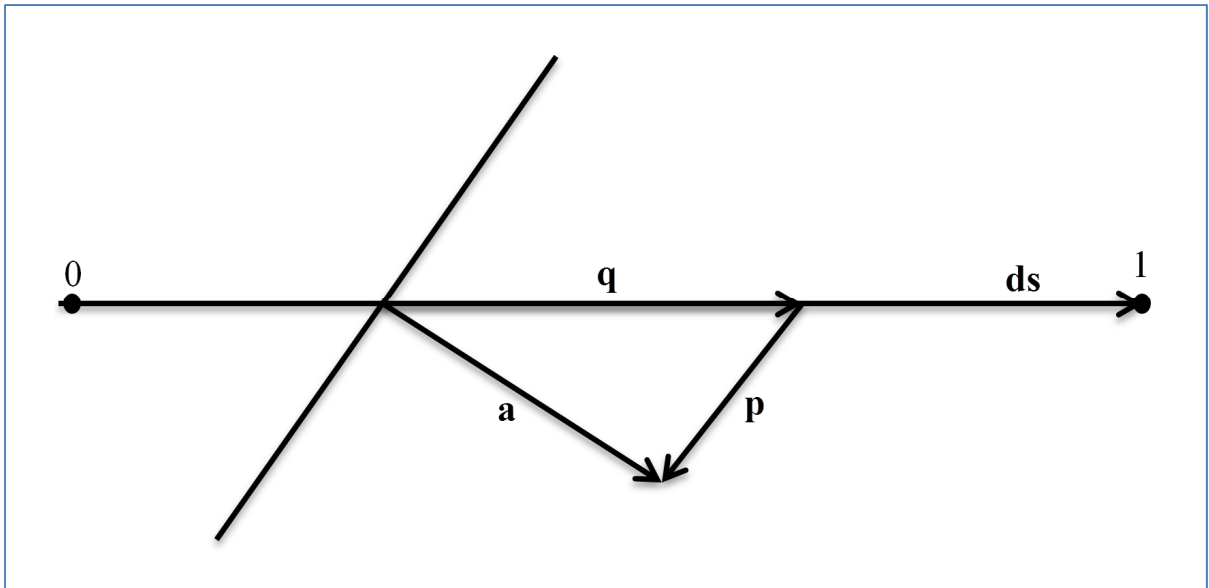


Figure 2.1 Decomposition schema for an interior face gradient

$$\nabla \phi_f = (\phi_1 - \phi_0) \mathbf{a} + \overline{\nabla \phi} - (\overline{\nabla \phi} \cdot \mathbf{ds}) \mathbf{a} \quad (2.21)$$

where:

$$\mathbf{a} = \frac{\mathbf{a}}{\mathbf{a} \cdot \mathbf{ds}} \quad (2.22)$$

$$\mathbf{ds} = \mathbf{x}_1 - \mathbf{x}_0 \quad (2.23)$$

$$\overline{\nabla \phi} = \frac{(\nabla \phi_0 + \nabla \phi_1)}{2} \quad (2.24)$$

The diffusion flux at an interior face can then be written:

$$D_f = \Gamma_f \nabla \phi_f \cdot \mathbf{a} = \Gamma_f [(\phi_1 - \phi_0) \mathbf{a} \cdot \mathbf{a} + \overline{\nabla \phi} \cdot \mathbf{a} - (\overline{\nabla \phi} \cdot \mathbf{ds}) \mathbf{a} \cdot \mathbf{a}] \quad (2.25)$$

Where Γ_f is a suitable average value (normally a harmonic average) of the cell values.

The second and third terms in Eq.2.25 represent the boundary secondary gradient (or cross-diffusion) contribution. In Star-CCM+, to prevent non-physical solutions the angle between \mathbf{a} and \mathbf{ds} is not greater than 90 degrees. A diagnostic tool that is provided in STAR-CCM+ allows this angle (termed skewness angle) to be computed in degrees and stored in adjacent cells. These terms can be optionally omitted, in which case Eq.2.25 reduces to:

$$D_f \approx \Gamma_f [(\phi_f - \phi_0) \alpha \cdot \mathbf{a}] \quad (2.26)$$

Boundary face

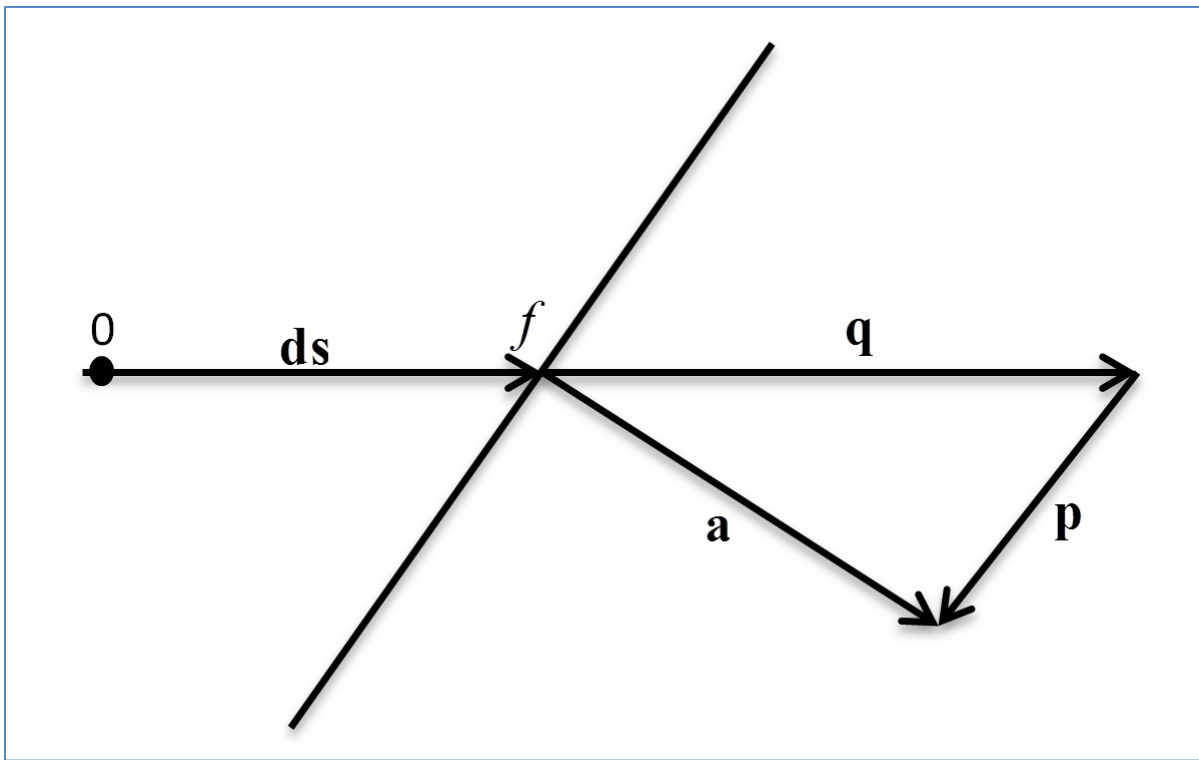


Figure 2.2 Decomposition schema for a boundary face gradient

A similar decomposition is used at a boundary face:

$$D_f = \Gamma_f \nabla \phi_f \cdot \mathbf{a} = \Gamma_f [(\phi_f - \phi_0) \alpha \cdot \mathbf{a} + \nabla \phi_0 \cdot \mathbf{a} - (\nabla \phi_0 \cdot \mathbf{ds}) \alpha \cdot \mathbf{a}] \quad (2.27)$$

Similar to interior faces, again, the angle between \mathbf{a} and \mathbf{ds} for boundary faces has to be greater than 0 and not greater than 90 degrees, to prevent non-physical solutions. The second and third terms in Eq.2.27 can be optionally neglected, in which case Eq.2.27 reduces to:

$$D_f \approx \Gamma_f [(\phi_f - \phi_0) \alpha \cdot \mathbf{a}] \quad (2.28)$$

Source Term

The source term $(S_\phi V)_0$ in Eq.2.11 where S_ϕ , evaluated at the cell centroid, and the cell volume, V is the simplest formulation consistent with a second-order discretization.

2.1.2.3 RANS Turbulence Model

To obtain the Reynolds-Averaged Navier-Stokes (RANS) equations, the Navier-Stokes equations for the instantaneous velocity and pressure fields are decomposed into a mean value and a fluctuating component. The averaging process may be thought of as time averaging for steady-state situations and ensemble averaging for repeatable transient situations. The resulting equations for the mean quantities are essentially identical to the original equations, except that an additional term now appears in the momentum transport equation. This additional term is a tensor quantity, known as the Reynolds stress tensor, which has the following definition:

$$\mathbf{T}_t \equiv -\overline{\rho \mathbf{v}' \mathbf{v}'} = -\rho \begin{pmatrix} \overline{u'u'} & \overline{u'v'} & \overline{u'w'} \\ \overline{u'v'} & \overline{v'v'} & \overline{v'w'} \\ \overline{u'w'} & \overline{v'w'} & \overline{w'w'} \end{pmatrix} \quad (2.29)$$

The challenge is thus to model the Reynolds stress tensor \mathbf{T}_t of Eq.2.29 in terms of the mean flow quantities, and hence provide closure of the governing equations. A basic approach using in STAR-CCM+ is Eddy viscosity models.

Eddy viscosity models use the concept of a turbulent viscosity μ_t to model the Reynolds stress tensor as a function of mean flow quantities.

The most common model is known as the Boussinesq approximation:

$$\mathbf{T}_t = 2\mu_t\mathbf{S} - \frac{2}{3}(\mu_t\nabla\cdot\mathbf{v} + \rho k)\mathbf{I} \quad (2.30)$$

where \mathbf{S} is the strain tensor:

$$\mathbf{S} = \frac{1}{2}(\nabla\mathbf{v} + \nabla\mathbf{v}^T) \quad (2.31)$$

While some simpler models rely on the concept of mixing length to model the turbulent viscosity in terms of mean flow quantities (similar to the Smagorinsky subgrid scale model used in LES), the eddy viscosity models in STAR-CCM+ solve additional transport equations for scalar quantities that enable the turbulent viscosity μ_t to be derived. These include the following turbulence model: K-Epsilon model.

2.1.2.4 Resolution

In Star-CCM+, for the case of the transport of a simple scalar, the finite volume discretization methods can be applied to discretize and solve these transport equations. The solution domain is subdivided into a finite number of small control volumes, corresponding to the cells of a computational grid. Discrete versions of the integral form of the continuum transport equations are applied to each control volume. The objective is to obtain a set of linear algebraic equations, with the total number of unknowns in each equation system corresponding to the number of cells in the grid. (If the equations are non-linear, iterative techniques that rely on suitable linearization strategies must be employed.) The resulting linear equations are then solved with an algebraic multigrid solver.

However, in the more complex cases such as the processes in the high-pressure turbine, based on finite volume methods, the implicit iteration methods and algebraic multigrid methods are popularly used: the implicit iteration methods used to linearize and assemble the algebraic equation systems; and the algebraic multigrid methods used to iteratively solve the discrete linear systems.

Implicit iteration methods

For the implicit iteration methods, the discretization approach results in the coefficients of a linear equation system being obtained. This system is solved implicitly, in an iterative fashion. The algebraic system for the transported variable ϕ at iteration $k+1$ is written implicitly as:

$$a_p \phi_p^{k+1} + \sum_{n \neq p} a_n \phi_n^{k+1} = b \quad (2.32)$$

where the summation is over all the neighbors n of cell p . The right-hand side, b , represents the explicit (that is, evaluated with the results from iteration k) contributions to the discretized equation. The coefficients a_n and a_p are obtained directly from the discretized terms (convective, diffusive and source term).

The Eq.2.32 can directly be solved for the unknowns ϕ^{k+1} , it is instead cast into “delta” form. Defining $\Delta\phi_p = \phi_p^{k+1} - \phi_p^k$, the Eq.2.32 becomes:

$$\frac{a_p}{\omega} \Delta\phi_p + \sum_n a_n \Delta\phi_n = b - a_p \phi_p^k - \sum_n a_n \phi_n^k \quad (2.33)$$

where ω is the under-relaxation factor. The right-hand side:

$$r = b - a_p \phi_p^k - \sum_n a_n \phi_n^k \quad (2.34)$$

is termed the residual, and represents the discretized form of the original equation (Eq.2.11) at iteration k . By definition, then, the residual becomes zero when the discretized equation is satisfied exactly.

For linear phenomena such as constant-property solid conduction, the linear system needs only be constructed and solved only once. In most situation of fluid dynamics, however, the system is non-linear. In this case, an iterative solution is required. There are two levels of iteration: an outer iteration loop controlling the solution update and an inner loop governing the iterative solution of the linear system. Since the outer iterations are repeated multiple times, it is sufficient to solve the linear system only approximately at each iteration.

Algebraic multigrid methods

Concerning the algebraic multigrid methods, for the linear systems, the equation:

$$\mathbf{Ax} = \mathbf{b} \quad (2.35)$$

represents the algebraic equations for each computational cell. The matrix \mathbf{A} represents the coefficients of the linear system (for example, the coefficients a_p and a_n on the left-hand side of Eq.2.33, the vector \mathbf{x} represents the unknowns ($\Delta \phi$ in Eq.2.33 in each cell), and vector \mathbf{b} represents the residuals (see Eq.2.34) from each cell.

Basic Iterative Methods

Typically, the matrix \mathbf{A} is sparse that is untenable for practical problems involving large grids. It is therefore preferable to use an efficient iterative method, such as the algebraic multigrid method in STAR-CCM+. The most basic iterative methods are Jacobi and Gauss-Seidel iteration. These methods involve visiting each cell in sequence, and updating the value of x_i in each cell i using the coefficients of its n neighbor cells as follows:

$$x_i = \frac{1}{A_{i,i}} \left(b - \sum_{\text{neighbors } n} A_{i,n} x_n \right) \quad (2.36)$$

The difference between Jacobi and Gauss-Seidel iteration is subtle: Jacobi uses the “old” values of x_n , while Gauss-Seidel uses the available values that have been updated, resulting in better convergence.

The ILU (Incomplete Lower-Upper) method, Saad [28], which was used for this research solves iteratively for \mathbf{x}^{k+1} using:

$$\mathbf{A}(\mathbf{x}^{k+1} - \mathbf{x}^k) = b - \mathbf{A}\mathbf{x}^k \quad (2.37)$$

where

$$\mathbf{A} \approx \mathbf{LU} = (\mathbf{D} + \mathbf{L}_A)(\mathbf{I} + \mathbf{D}^{-1}\mathbf{U}_A) \quad (2.38)$$

where \mathbf{I} is the identity matrix, \mathbf{L}_A and \mathbf{U}_A are the lower and upper triangular matrices of the original matrix \mathbf{A} , and \mathbf{D} is a diagonal matrix. The ILU method is more computationally expensive but more robust than the Gauss-Seidel method.

Multigrid Methods

The primitive iteration methods that are described above, while relatively simple to implement, exhibit relatively slow convergence characteristics. They tend to be only effective at removing high-frequency (rapidly varying) components of the error. This effectivity suggests that some of the work could be done on a coarse grid. Computations on coarse grids are much less costly and the Gauss-Seidel method converges four times faster on a grid half as fine. Multigrid algorithms do this using the following steps:

- Agglomerate cells to form coarse grid levels.
- Transfer the residual from a fine level to a coarser level (known as restriction).

- Transfer the correction from a coarse level back to a finer level (known as prolongation).

Multigrid algorithms can be divided into two types: geometric and algebraic.

- Geometric multigrid uses the grid geometry and the discrete equation at the coarse level to arrive at the linear system that is to be solved on that level.
- Algebraic multigrid derives a coarse level system without reference to the underlying grid geometry or discrete equations. The coarse-grid equations are derived from arithmetic combinations of the fine-grid coefficients.

Since it is not always straightforward to obtain suitable discrete equations on the coarse levels, algebraic multigrid (AMG) is clearly at an advantage. Therefore, it is used for the solution in STAR-CCM+ for this research.

Concerning the case with the chemical reactions, species transport formulation is written as follows:

$$\oint_{\partial V} \rho Y_i (u - u_g) \cdot d\mathbf{a} = \oint_{\partial V} \left[J_i + \frac{\mu_t}{\sigma_t} \nabla Y_i \right] \cdot d\mathbf{a} + \int_V S_{Y_i} dV \quad (2.39)$$

where i is the component index, ρ is the overall density, $dV = \chi dV$ where χ is the void fraction, $d\mathbf{a} = \chi d\mathbf{a}$, u is the velocity, u_g is the grid velocity, μ_t is the turbulent dynamic viscosity, σ_t is the turbulent Schmidt number ($\sigma_t=0.9$), the mass fraction $Y_i = m_i / m_m$ of species i in mixture m , S_{Y_i} is a user specified region source term for species i and J_i is the diffusive flux.

For multi-component diffusion, the diffusive flux for component i becomes a function of the mass fractions for all components:

$$J_i = \rho \sum_{j=1}^N D_{i,j} \nabla Y_j \quad (2.40)$$

$D_{i,j}$ is the molecular diffusivity and represents the multi-component diffusion coefficients which are calculated using the Maxwell-Stefan equations. These equations define the diffusive flux implicitly as a function of mole fraction gradients, which are given as:

$$\nabla X_i = \frac{M_w}{\rho} \sum_{j=1, j \neq i}^N \left(\frac{X_i J_j}{M_j \mathcal{D}_{i,j}} - \frac{X_j J_i}{M_i \mathcal{D}_{i,j}} \right) \quad (2.41)$$

$\mathcal{D}_{i,j}$ represents the binary diffusion coefficient between component i and j ; the mole fraction $X_i = Y_i W_m / W_i$ of the species i in a mixture m , where Y_i is the species mass fraction, W_m is the molecular weight of the mixture, and W_i is the molecular weight of the species. Writing these equations in matrix form gives:

$$[B] \nabla Y = [A] J \quad (2.42)$$

where $[B]$ represents the mapping from mass fraction gradients to mole fraction gradients and $[A]$ represents the Maxwell-Stefan equations. By inverting $[A]$ and multiplying by the matrix $[B]$, the multi-component diffusion coefficients are calculated.

$$D_{i,j} = \rho \sum_{k=1}^N A_{i,k}^{-1} B_{k,j} \quad (2.43)$$

For N components, STAR-CCM+ solves transport equations for all species and ensures that all mass fractions sum to 1.

For the case of multi-components of this research, an additional term is added to the diffusive flux, J_j , for each component. In the case that multi-component diffusion is activated, the diffusive flux can be calculated as [29]:

$$J_i = \rho \left[\sum_{j=1}^N D_{i,j} \nabla Y_j \right] + \rho \frac{D_{i,T}}{T} \nabla T \quad (2.44)$$

where $D_{i,T}$ is the thermal diffusion coefficient for component i and is computed based on the thermal diffusion ratio. The thermal diffusion ratio between component i and component j proposed by Warnatz et al.[30] is given as:

$$K_{T,ij} = \frac{15}{2} \frac{(2A_{i,j}^* + 5)(6C_{i,j}^* - 5)}{A_{i,j}^*(16A_{i,j}^* - 12B_{i,j}^* + 55)} \frac{M_i - M_j}{M_i + M_j} X_i X_j \quad (2.45)$$

where $A_{i,j}^*$, $B_{i,j}^*$ and $C_{i,j}^*$ are three ratios of collision integrals between component i and component j , their polynomials have been fit to tables [30, 31]. Using the thermal diffusion ratio, the thermal diffusion coefficient for component i is given as:

$$D_{i,T} = D_{i,m} \frac{M_i}{M_w} \sum_{j=1}^N K_{T,ij} \quad (2.46)$$

where $D_{i,m}$ is the effective molecular diffusivity of component i into the mixture, M_i is the molecular weight of component i , and M_w is the mean molecular weight of the mixture.

Based on the same steps to solve Eq.2.11, Eq.2.39 is solved in STAR-CCM+ to precise the evolution of components and the chemical process.

2.2 Numerical modeling

In this section, we describe the 3D HPT aero-thermodynamic and emission model which was developed in this study. The design of HPT and the modeling of mesh system are discussed briefly in Section 2.2.1. The governing equations are summarized in Section 2.2.2 Section 2.2.3 presents the aero-thermodynamic and chemical modeling.

2.2.1 HPT design and meshing

2.2.1.1 HPT design

The design of rotor and stator blades for high pressure turbine (HPT) remains a challenge in the field due to the complexity of HPT blade profile [32]. The first studies were realized by Demeulenaere [33] and Yershov [34, 35] and then further studied by several authors [36-41] in which the fundamental parameters of turbine were started by the use of 2D and 3D conceptions. In this work, we focus on CFM56 engine, which is among the most popular aircraft engines. This engine has been simulated and tested by several researchers [10, 11, 42-44]. This paper also used the findings of previous studies to build a high pressure turbine (HPT) in CFM56 engine by Blade Gen conception module. First, the rotor and stator geometry were built. Next, the blade surface was constructed.

In the order of conception, the main angles of the rotor (horizontal angle of blade profile - beta and vertical angle of blade profile - theta) were implemented (Fig.2.3a). The theta and beta functions, as a function of the rotor blade axial distances, are shown in Fig.2.3b, c where these angle functions are illustrated at 0 %, 50 % and 100 % of the span. To define the blade geometry, the blade thickness as a function of blade axial distance is defined (Fig.2.3 d). The length (C) and the ratio of chord (S/C) (S is the pitch of blades) were set to 46.069 and 2.396 respectively. The general dimension at two cylindrical surfaces (hub and shroud), leading edge (LE), and trailing edge (TE) were also implemented: $R_{LE-Hub} = 254$ mm, $R_{LE-Shroud} = 360$ mm, and $R_{TE-Shroud} = 360$ mm (where R is a radius). For a CFM56 engine type, the number of rotor blades of HPT is equal to 83. Based on these dimensions, the total rotor profile structure is identified.

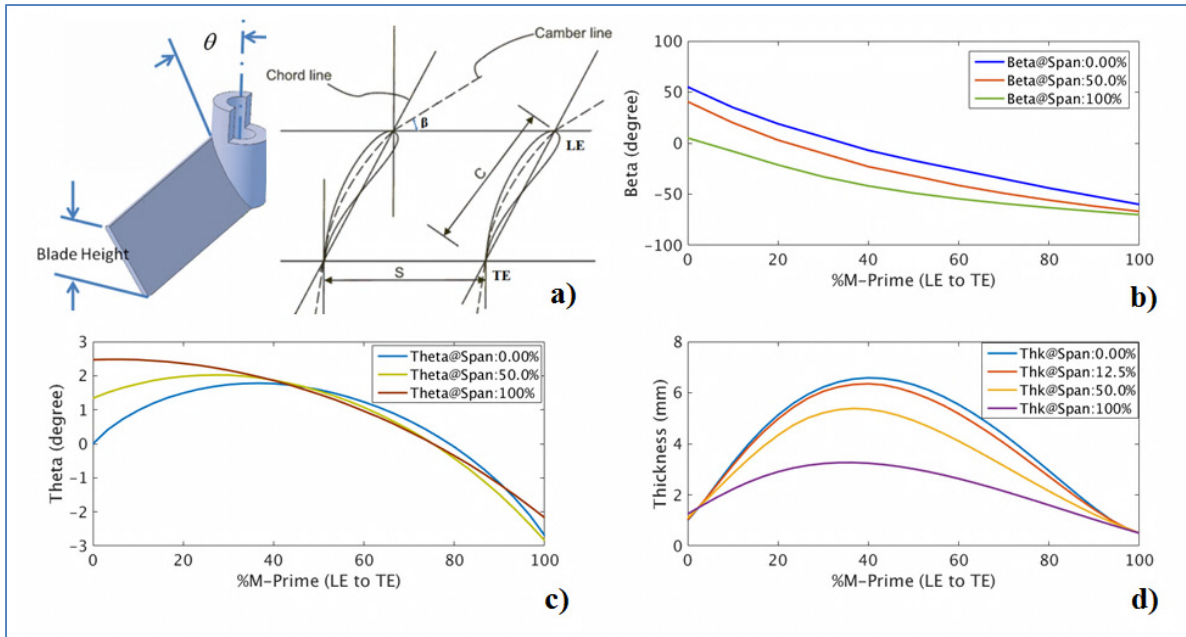


Figure 2.3 Basic blade parameters (a) and beta- (b), theta- (c), thickness- (c) function of blade axial distance for rotor blade

This process was repeated for the stator, with $R_{LE-Hub} = 254$ mm, $R_{LE-Shroud} = 356$ mm, and $R_{TE-Shroud} = 360$ mm; the length of the chord $C = 71.713$ and the ratio of chord $S/C = 0.518$; the number of stator blades of HPT is equal to 43. With this information, the stator blade profile and the total stator profile structure were obtained.

Then, performing of the assembly of stator and rotor allowed obtaining the complete structure of the HPT as shown in Fig.2.4.

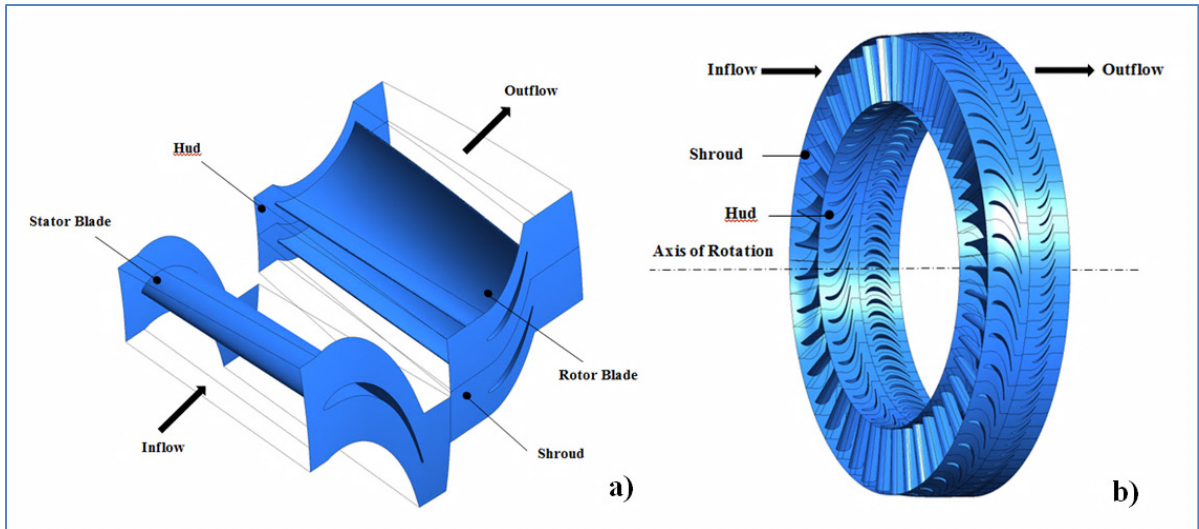


Figure 2.4 Fluid domain structure of one stator and two rotor blades (a), and HPT complete structure (b)

2.2.1.2 Meshing

During the simulation of this work, approximately 6 million polyhedral unstructured mesh types were used. The unstructured meshes are especially suitable for complex geometries, such as turbine blades [32, 45]. This approach has several advantages over structured meshing for the current applications, including the case of automation and the ability to concentrate the mesh points in the region of the blades.

To simplify computation, or reduce blade passage numbers, circumferentially periodic boundary conditions are applied at the domain faces coincident with neglected adjacent blades as shown in Fig.2.5 a [26, 45-47]. For multi-row turbomachinery, a mixture of sliding and mixing planes can be used to increase accuracy and reduce computational cost [48]. In this study, the outlet of the stator blade fluid domain, associated with the rotor blade inlet, was coupled (called a “mixing plane”) [49, 50]. The stator/rotor interactions are accounted for through exchange of averaged aero-thermodynamic parameters.

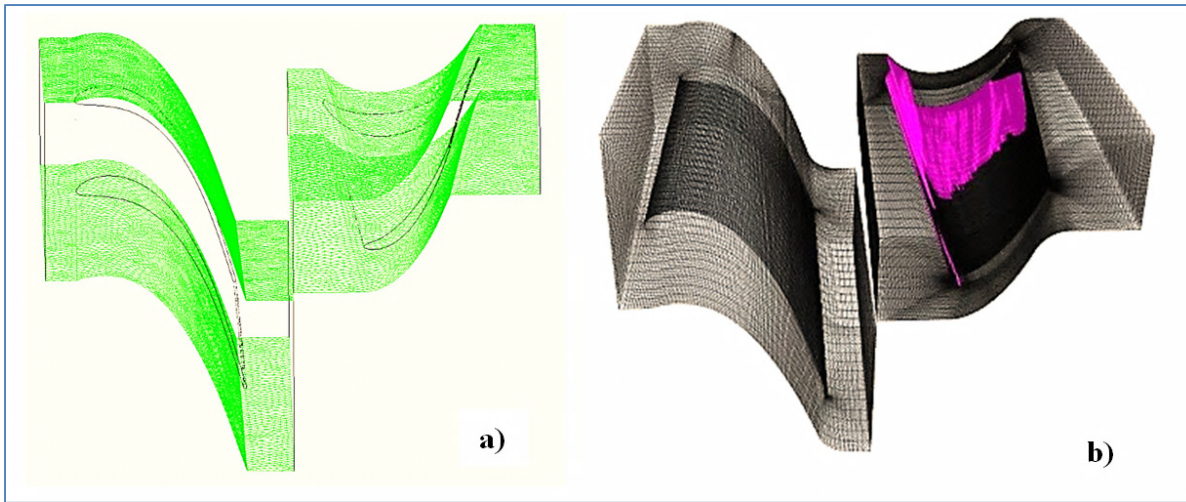


Figure 2.5 Mesh structure of periodic surfaces (a) and appreciation of bad elements for improvement of the mesh quality (b)

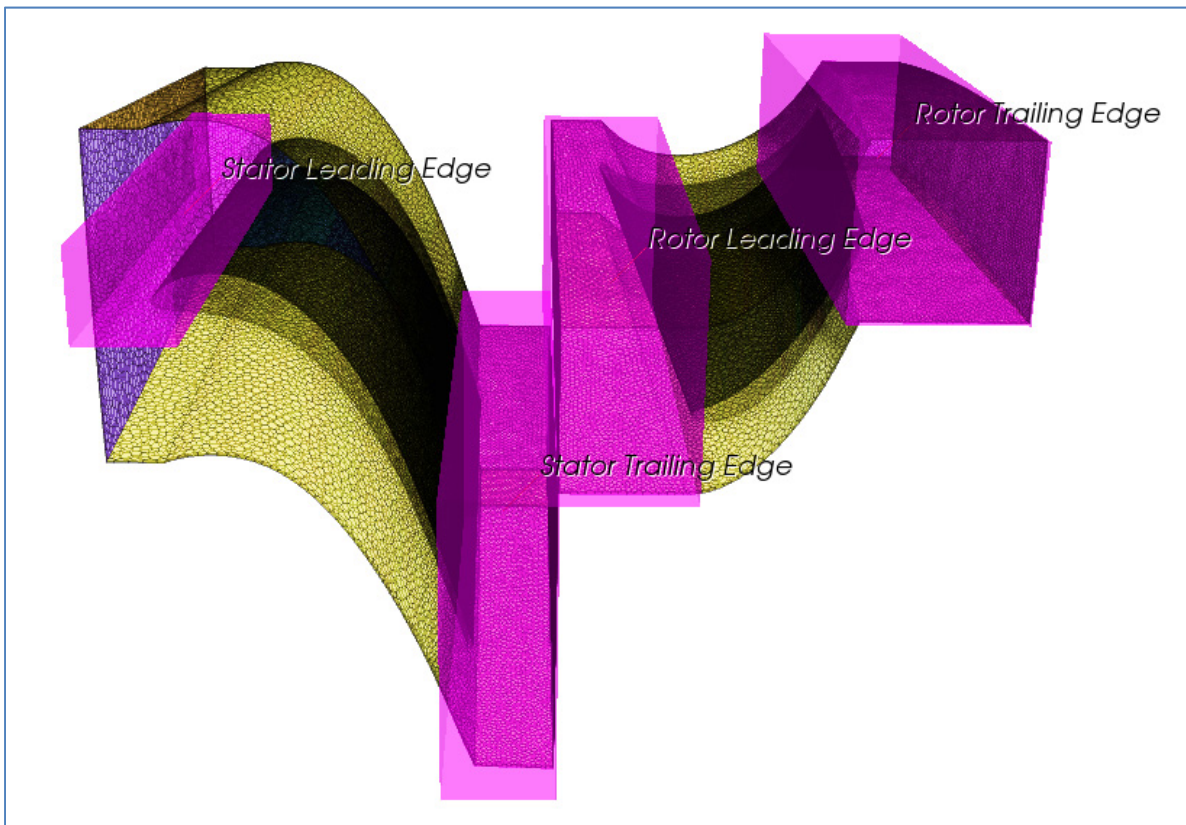


Figure 2.6 Four blocks to control the mesh quality at the LE, TE of stator and rotor

It was demonstrated in the literature [40-43] that the mesh quality affected both efficiency and accuracy of the computational fluid dynamic (CFD) solution. Meshes with distorted elements have made the computation more difficult and less accurate. In this research, to obtain the mesh system in high quality, the identification of surface smoothing, uniform size and transferring angles of the elements are carried out in accordance with recent publications [51-55]. The distortion elements in the mesh were identified, as shown in Fig.2.5b. Then, the geometry parameters of the HPT (theta, beta, thickness) and its meshing element parameters (maximum size, minimum size, maximum volume, minimum volume, refining percentage) were rechecked and might be changed, respectively. Four blocks at the LE, TE of stator and rotor were established to control the mesh quality by refining meshes around these four zones (see Fig.2.6). Consequently, the mesh system was modified and re-meshed until the distortion elements were disappeared and the quality of the mesh system was improved completely. This process was described in detail in the following figure:

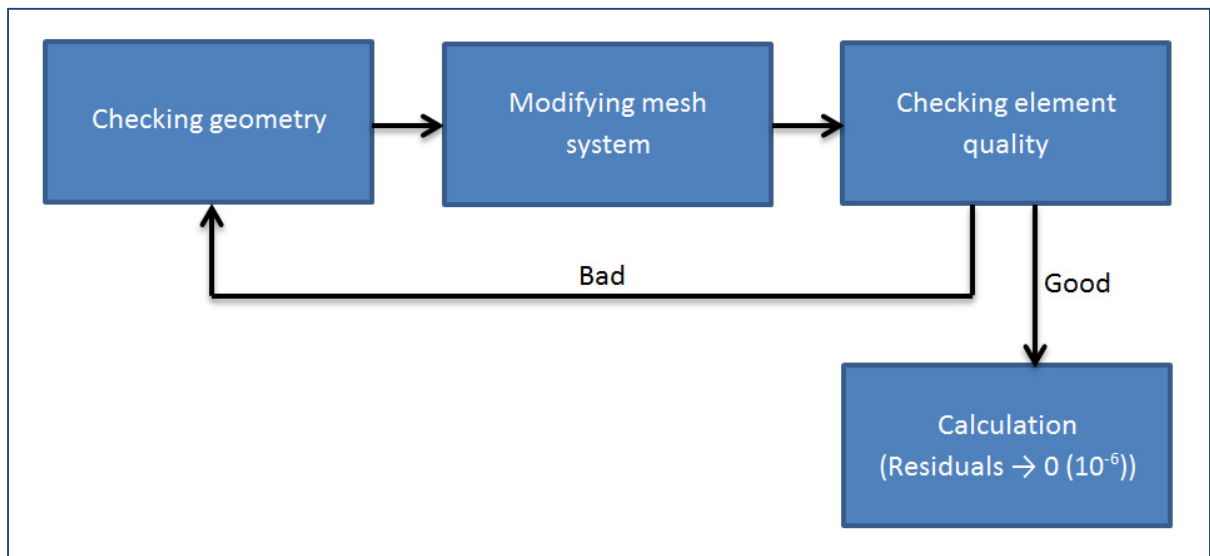


Figure 2.7 Schema of the process for improving the mesh quality

2.2.2 Computational fluid dynamic (CFD) and chemical modeling

The CFD calculations reported in this paper have been performed on a stage stator-rotor domain and computations are realized using an implicit solver and a coupled flow model to solve the RANS equations. The coupled flow model solves the conservation equations for mass, momentum and energy, simultaneously. One advantage of this formulation is its robustness for solving flows with dominant source terms, such as rotation [56, 57].

Table 2.1 Initial aero-thermodynamic conditions

Parameter	Value	Parameter	Value
P_{static} (kPa)	3.092	Velocity (m/s)	100
P_{total} (kPa)	3.113	Turbulence intensity	0.10
T_{total} (K)	1341	Turbulent length Scale (m)	0.01
Rotor speed (rpm)	8500		

Table 2.2 Neutral gas species initial conditions

Species	ppmv	Species	ppmv
NO	130	O ₂	130000
NO ₂	14.5	OH	60.0
NO ₃	4.320E-5	HO ₂	8.310E-1
HNO	1.200E-2	H ₂ O ₂	2.520E-2
HNO ₂	1.400E-1	H	7.580E-3
HNO ₃	4.710E-4	H ₂	2.490E-1
N ₂ O	0.00	N	0.00
SO	1.360E-3	H ₂ O	47800
SO ₂	10.6	CO	201
SO ₃	3.320E-1	N ₂	772000
C	5.86	CO ₂	50300
O	1.47		

The current calculations use the high-resolution (Second-order Upwind) advection scheme because of its advantages of accuracy in comparison with First-order Upwind and Central scheme, especially for the complex propagation of 3D flow in the turbine [58]. Initial value of temperature, pressure, velocity, and turbulent rates at the stator inlet and rotor speed were set in the Table 2.1; the turbulent rates were chosen [6, 10, 59]; the parameters of flow at the HPT outlet were calculated basing on results of previous mesh elements. The type of wall treatment implemented herein, has been proposed by Coull [32] and Goldstein [60], the walls are considered adiabatic: no heat transfer with the fluid near the walls. The components of velocities are zero at the walls (no-slip condition). In STAR-CCM+, to have advantages from both high- y^+ wall treatment (low cost of calculation but it is unlikely that significant error results from y^+ values as low as 12) and low- y^+ wall treatment (more accuracy of calculation but use this treatment only if the entire mesh is fine enough for y^+ to be approximately 1 or less), all y^+ wall treatment was used in this research. All y^+ wall treatment is a hybrid approach and was designed to give results similar to the low- y^+ treatment as $y^+ \rightarrow 0$ (approximately 1-5 and less) and to the high- y^+ treatment for $y^+ \geq 30$ (30-40). Nevertheless, in the calculation process, automatically the high or low- y^+ wall treatment is used, depending on regions near the walls of the HPT. Consequently, the calculation process has a good accuracy with a lower cost of calculation.

With respect to the chemical modeling, the species in the high pressure turbine (HPT) include NO_x , as well as SO_x , CO, and species associated with HO_x kinetics. Oxidative processes of interest in the HPT occur as exhaust gases from the high temperatures and pressures above 1000 K and above 6 atm [5, 6, 61]. To adapt the conditions of high temperature and pressure in the HPT, the full chemical mechanism used for the computations was truncated from larger chemical set, developed by Lukachko et al. [5, 6] and Mueller et al. [62] and based on the previous studies [63-67] and laboratory experiments [68]. Neutral gas species initial conditions can be found in Table 2.2. A reaction list has been described in Table 2.3.

In the framework of this study, we concentrate on the formation of NO_x and SO_x , in particular, the formation of SO_3 and NO_2 (sources contribute to production of sulfuric acid

and nitric acid as follows: $\text{SO}_3 + \text{H}_2\text{O} \leftrightarrow \text{H}_2\text{SO}_4$ and $\text{NO}_2 + \text{OH} \leftrightarrow \text{HNO}_3$). The formations of chemical species are complex due to the interactions between dilution zones (form of HPT geometry), aero-thermodynamic conditions, and conversion of chemical species in the oxidative processes [5, 62, 68]. Concerning SO_x , aero-thermodynamically, SO_2 is favored at higher, near flame temperature (above 1200 K); and SO_3 is favored at intermediate temperature [6]. Increase in oxygen concentration and pressure may enhance the formation of SO_3 [69, 70]. Recent modeling results demonstrated that at high pressures, where the fractional conversion of NO to NO_2 increases, SO_3 formation occurs via $\text{SO}_2 + \text{NO}_2 \leftrightarrow \text{SO}_3 + \text{NO}$ and at lower pressures, SO_3 appears through $\text{SO}_2 + \text{O}(\text{+ M}) \leftrightarrow \text{SO}_3(\text{+ M})$ [62]. Thus, at high pressure, the conversion of NO to NO_2 directly linked to conversion of SO_2 to SO_3 and kinetic coupling of NO_x and SO_x chemistry significantly reduces SO_2 . Concerning NO_x , similar to SO_x , O and OH are central to NO_x chemistry [5]. NO_2 was produced via $\text{NO} + \text{O} \leftrightarrow \text{NO}_2$; $\text{NO}_2 + \text{O} \leftrightarrow \text{NO} + \text{O}_2$; $\text{HONO} + \text{OH} \leftrightarrow \text{NO}_2 + \text{H}_2\text{O}$. However, the formation of NO_2 is typically dominated by $\text{NO} + \text{HO}_2 \leftrightarrow \text{NO}_2 + \text{OH}$ [5].

Table 2.3 Chemical mechanism for the HPT

Reaction ^a	A, Mole.cm.s.k	b	E _A , Cal.mole ⁻¹
$\text{H}_2 + \text{M} \leftrightarrow \text{H} + \text{H} + \text{M}^b$	4.57E+19	-1.4	104000.0
$\text{O} + \text{H}_2\text{O} \leftrightarrow \text{OH} + \text{OH}$	2.97E+06	2.0	13400.0
$\text{O} + \text{H}_2 \leftrightarrow \text{H} + \text{OH}$	5.06E+04	2.7	6290.0
$\text{O} + \text{O} + \text{M} \leftrightarrow \text{O}_2 + \text{M}^b$	6.17E+15	-0.5	0.0
$\text{H} + \text{O}_2 \leftrightarrow \text{O} + \text{OH}$	1.94E+14	0.0	16440.0
$\text{H} + \text{O}_2 + \text{M} \leftrightarrow \text{HO}_2 + \text{M}^b$	4.52E+13	0.0	0.0
$\text{H} + \text{O} + \text{M} \leftrightarrow \text{OH} + \text{M}^b$	4.72E+18	-1.0	0.0
$\text{OH} + \text{H}_2 \leftrightarrow \text{H}_2\text{O} + \text{H}$	2.16E+08	1.5	3430.0
$\text{OH} + \text{H} + \text{M} \leftrightarrow \text{H}_2\text{O} + \text{M}^b$	2.21E+22	-2.0	0.0
$\text{HO}_2 + \text{O} \leftrightarrow \text{O}_2 + \text{OH}$	1.75E+13	0.0	-397.0
$\text{HO}_2 + \text{H} \leftrightarrow \text{H}_2 + \text{O}_2$	6.62E+13	0.0	2130.0
$\text{HO}_2 + \text{H} \leftrightarrow \text{OH} + \text{OH}$	1.69E+14	0.0	874.0
$\text{HO}_2 + \text{OH} \leftrightarrow \text{H}_2\text{O} + \text{O}_2$	1.90E+16	-1.0	0.0
$\text{HO}_2 + \text{HO}_2 \leftrightarrow \text{H}_2\text{O}_2 + \text{O}_2^c$	4.20E+14	0.0	11980.0

Table 2.3 Chemical mechanism for the HPT (continued)

Reaction ^a	A, Mole.cm.s.k	b	E _A , Cal.mole ⁻¹
HO ₂ + HO ₂ ↔ H ₂ O ₂ + O ₂ ^c	1.30E+11	0.0	-1629.0
H ₂ O ₂ ↔ OH + OH	2.95E+14	0.0	48460.0
H ₂ O ₂ + O ↔ OH + HO ₂	9.64E+06	2.0	3970.0
H ₂ O ₂ + H ↔ H ₂ O + OH	1.00E+13	0.0	3590.0
H ₂ O ₂ + H ↔ HO ₂ + H ₂	4.82E+13	0.0	7950.0
H ₂ O ₂ + OH ↔ H ₂ O + HO ₂ ^c	1.00E+12	0.0	0.0
H ₂ O ₂ + OH ↔ H ₂ O + HO ₂ ^c	5.80E+14	0.0	9557.0
CO + O + M ↔ CO ₂ + M ^b	1.80E+10	0.0	2380.0
CO + O ₂ ↔ CO ₂ + O	2.53E+12	0.0	47700.0
CO + OH ↔ CO ₂ + H	1.50E+07	1.3	-765.0
CO + HO ₂ ↔ CO ₂ + OH	5.80E+13	0.0	22930.0
N + O ₂ ↔ NO + O	6.40E+09	1.0	6280.0
N + OH ↔ NO + H	3.80E+13	0.0	0.0
N + HO ₂ ↔ NO + OH	1.00E+13	0.0	2000.0
N + CO ₂ ↔ NO + CO	1.90E+11	0.0	3400.0
N + NO ↔ N ₂ + O	3.27E+12	0.3	0.0
N + NO ₂ ↔ NO + NO	4.00E+12	0.0	0.0
N + NO ₂ ↔ N ₂ O + O	5.00E+12	0.0	0.0
N + NO ₂ ↔ N ₂ + O ₂	1.00E+12	0.0	0.0
N + HNO ↔ N ₂ O + H	5.00E+10	0.5	3000.0
N + N ₂ O ↔ N ₂ + NO	1.00E+13	0.0	19870.0
NO + M ↔ N + O + M ^b	9.64E+14	0.0	148400.0
NO + O ↔ NO ₂	1.30E+15	-0.8	0.0
NO + H ↔ HNO	1.52E+15	-0.4	0.0
NO + OH ↔ HONO	1.99E+12	0.0	-721.0
HO ₂ + NO ↔ NO ₂ + OH	2.11E+12	0.0	-479.0
NO ₂ + O ↔ O ₂ + NO	3.91E+12	0.0	-238.0
NO ₂ + O ↔ NO ₃	1.33E+13	0.0	0.0
NO ₂ + H ↔ NO + OH	1.32E+14	0.0	361.6
NO ₂ + OH ↔ HNO ₃	2.41E+13	0.0	0.0
NO ₂ + CO ↔ CO ₂ + NO	9.03E+13	0.0	33780.0
NO ₂ + NO ₂ ↔ NO ₃ + NO	9.64E+9	0.7	20920.0
NO ₂ + NO ₂ ↔ 2NO + O ₂	1.63E+12	0.0	26120.0

Table 2.3 Chemical mechanism for the HPT (continued)

Reaction ^a	A, Mole.cm.s.k	b	E _A , Cal.mole ⁻¹
HNO + O ₂ ↔ NO + HO ₂	1.00E+13	0.0	25000.0
HNO + O ↔ OH + NO	1.81E+13	0.0	0.0
HNO + H ↔ H ₂ + NO	1.81E+13	0.0	993.5
HNO + OH ↔ H ₂ O + NO	1.00E+13	0.0	993.5
HNO + NO ↔ N ₂ O + OH	2.00E+12	0.0	26000.0
HNO + NO ₂ ↔ HONO + NO	6.02E+11	0.0	1987.0
HNO + HNO ↔ H ₂ O + N ₂ O	8.51E+08	0.0	3080.0
HONO + O ↔ OH + NO ₂	1.20E+13	0.0	5961.0
HONO + H ↔ H ₂ + NO ₂	1.20E+13	0.0	7352.0
HONO + OH ↔ H ₂ O + NO ₂	1.26E+10	1.0	135.1
N ₂ O + M ↔ N ₂ + O + M ^b	7.91E+10	0.0	56020.0
N ₂ O + O ↔ O ₂ + N ₂	1.00E+14	0.0	28000.0
N ₂ O + O ↔ 2NO	1.00E+14	0.0	28000.0
N ₂ O + H ↔ N ₂ + OH ^c	2.53E+10	0.0	4550.0
N ₂ O + H ↔ N ₂ + OH ^c	2.23E+14	0.0	16750.0
N ₂ O + OH ↔ HO ₂ + N ₂	2.00E+12	0.0	40000.0
N ₂ O + CO ↔ N ₂ + CO ₂	5.01E+13	0.0	44000.0
SO + O ₂ ↔ SO ₂ + O	1.44E+11	0.0	4740.0
SO + SO ₃ ↔ SO ₂ + SO ₂	1.20E+09	0.0	0.0
SO + NO ₂ ↔ SO ₂ + NO	8.43E+12	0.0	0.0
SO + OH ↔ SO ₂ + H	5.18E+13	0.0	0.0
SO ₂ + M ↔ SO + O + M	2.90E+16	0.0	117180.0
SO ₂ + NO ₂ ↔ SO ₃ + NO	6.31E+12	0.0	27176.0
SO ₃ + M ↔ SO ₂ + O + M	3.16E+15	0.0	63750.0
SO ₃ + H ↔ SO ₂ + OH	0.49E+02	2.69	23800.0

Note:

Read 4.57E+19 as $4.57 \cdot 10^{19}$; $k_f = AT^b e^{(-E_A/R_gT)}$

^a All reactions are reversible

^b Third body efficiencies incorporated. For reactions (1), (4), (6), (7) and (8), H₂/2.5, H₂O/12, CO/1.9, and CO₂/3.8; for reaction (20), N₂/1.33, H₂/2.5, H₂O/12, CO/1.9 and CO₂/3.8; for reaction (33), N₂/1.5 and CO/2.5; for reaction (36), H₂O/5.0; and for reaction (50), H₂O/7.5, NO/2, CO/2, and CO₂/3.

^c Multiple rates specified. For reaction specified with more than one set of parameters (i.e., 13/14, 18/19, and 52/53) the overall reaction rate is the sum of the rates as calculated from each set of parameters.

Finally, the equations were discretized and solved in the HPT. The Acceleration Factor of calculation convergence was chosen 0.2 (can be set from 0 (slow but stable) to 1 (fast but least stable)), and the tolerance for the stopping criterion based on the continuity equation residual was chosen 10^{-6} .

CHAPTER 3

AERO-THERMODYNAMIC AND CHEMICAL PROCESS INTERACTIONS IN AN AXIAL HIGH PRESSURE TURBINE

Trung Hieu Nguyen^a, Tri Phuong Nguyen^b, Xavier Vancassel^c, Francois Garnier^a

^a TFT Laboratory, Ecole de Technologie Superieure (ETS), 1100 Notre-Dame St W,
Montreal, Quebec, Canada H3C 1K3

^b Department of Chemistry, University of Montreal (UdeM), 2900, Édouard-
Montpetit Boul., Montreal, Quebec, Canada H3C 3J7

^c The French Aeropace Lab ONERA, 91120 Palaiseau, France

This chapter has been submitted for the publication in the “*International Journal of Engine Research*” – SAGE Publications, October 2017

3.1 Introduction

Aircraft emissions directly contribute to environmental pollutants and local air quality around airports [2], as well as climate change [71, 72] and human health [3] through its engine-emitted species, such as greenhouse gases (CO₂, water vapor), sulfur and nitrogen oxides (SO_x, NO_x), unburnt hydrocarbons (UHC), and particulate matter (PM) [73, 74]. Unfortunately, only a very limited knowledge of PM formation can be found in the literature [75-77]. Thus, fundamental understanding of the formation mechanism of aerosols and effect of engine operating parameters towards aerosols are crucial. In this context, a few studies have been conducted to characterize the aero-thermodynamic process and particulate emission. Recently, various experiment series on APEX1, JETS/APEX2 and on APEX3 [10, 78]) with different types of engine at ground level have been reported. These reports show that the aerosol formations are sensitive to engine design, types of selected fuel, engine operating parameters, and atmospheric conditions. However, the processes of intra-engine (combustor, turbine and exhaust nozzle) have not been discussed in the literature.

Zero-dimensional (0D), one-dimensional (1D), and two-dimensional (2D) numerical simulations have often been used to investigate the aero-thermodynamic and chemical

processes in aircraft engines. The complexities of 3D modeling and of chemical kinetics in high temperature and high pressure typically were difficult problems in the HPT.

Starik and al. [4] computed the turbine flow with a quasi-one-dimensional (Q1D) model. The kinetic models for S-containing gases and chemiions were used. The authors reported that the formation of gaseous sulfate aerosol pollutants and ions and the sulfur conversion fraction significantly depend on the temperature profile along the flow in the engine. Nevertheless, most of the rate constants for ion chemistry were determined at low temperature ranges (300 K - 500 K) only, which are significantly different from the real operating temperatures of high pressure turbine (HPT) (above 1000 K) and therefore the certitude of the results was always in question.

In another study, one-dimensional (1D) and two-dimensional (2D) simulations have been proposed by Lukachko and co-workers [6]. The authors showed 6.3% increase in sulfur oxide content through turbine and the results were very sensitive to the species concentration at the combustor exit and combustor exit temperature. The comparison of an averaged 2D modeling with that of a 1D simulation suggests that the oxidation sulfur magnitude may be under predicted, < 47 %, over a single blade row. Although these calculations were carried out at high temperature (above 1000 K) and high pressure (above 1.6 atm), which are very close to the operation of HPT, however, effects of rotor speed on the flow parameters and sulfur formation have not been discussed. Furthermore, the study of 3D blade geometry has not been performed. It would also be interesting, for comprehensive understanding, to study the 3D fluid-chemical interactions.

More recently, Moniruzzaman [12] and Bisson [13] used 0D and 0D/1D simulations to study the chemical processes in an HPT. The authors predicted the evolution of gaseous aerosol pollutants and particles in combustors and post-combustors (turbine and nozzle). The data at nozzle exit was compared to that obtained with APEX experiments developed by Wey [10, 78] for validation. The design of combustor was divided in three areas: primary zone, primary hole zone, and dilution zone. However, the conception of turbine was simplified and replaced by a reactor, and the influence of rotating blades was converted to the change of

ratio of flow debit. Since the authors used 0D and 1D simulations, the effect of blade geometry was not taken into account.

Several researchers have attempted to describe the model turbulent chemistry in a turbine by using three-dimensional (3D) numerical codes. Such computer numeration often requires long calculation time, and in some cases, necessitates the use of a supercomputer [14]. Demeulenaere and al. [33] started to design 3D modeling for turbomachinery blade, and Yershov and al. [34, 35, 79] studied numerical simulation of 3D flow in axial turbomachinery. Nevertheless, these models were limited to the fundamental flow parameters, such as temperature and pressure. Lampart et al. introduced a concept optimization to improve the efficiency of flow by 3D RANS computations [8]. The flow parameters and turbulence have been studied by Tucker et al. [26], who reconfirmed the signification of RANS approach, and included the factor ‘best practices’ in the 3D turbomachinery calculations. However, 3D turbomachinery chemistry was still not considered in their investigation.

On account of these facts, we propose herein a new approach to investigate 3D model turbulent chemistry at high temperature and high pressure as well as interactions between aero-thermodynamic and chemical processes. We also investigate the evaluation of the effect of 3D geometry and rotor speed on chemical and thermo-dynamical processes in an aircraft engine turbine by using the turbulence modeling strategy RANS. In order to achieve these goals, we set up the following steps: (i) the HPT conception of gas turbine is performed by the module BLADE GEN, (ii) the STARCCM+ (CD-ADAPCO) software is used to simulate the aero-thermodynamic and chemical processes, and (iii) the results are executed and analyzed with an in-house Matlab routine, and compared with that reported in the literature.

3.2 Aero-Thermodynamic and chemical process interactions in an axial high pressure turbine

This section presents the results of simulations of the HPT, discusses the effects of turbine chemical and aero-thermodynamic processes on the formation of sulfate and nitrate aerosol

pollutants, interactions between the processes in the HPT, and effect of spatial geometry and operating condition (rotor speed) on the HPT performance. Section 3.2.1 presents the aero-thermodynamic evolution (without chemical reactions) to better understand variations of aerodynamic parameters and function of the HPT; the initial aero-thermodynamic condition (see Table 2.1) and air at the stator inlet were used. Section 3.2.2 concentrates the formation of NO_x and SO_x aerosols by effects of the aero-thermodynamic and chemical kinetics (with chemical reactions); the initial aero-thermodynamic conditions (in Table 2.1) and neutral gas species initial conditions (see Table 2.2) are set at the same time. The results in section 3.2.3 serve to analyse influences of chemical process on flow parameters, which typically include temperature, pressure, and velocity of flow. This feedback from chemical process demonstrated briefly the interaction between aero-thermodynamic and chemical processes in the HPT.

The results presented in section 3.2.4 discuss calculations for 3D turbine stage and illustrate that the potential impacts of flow non-uniformities cannot be represented directly by 1D model because there are important effects not captured by these models, although it presents explicitly the trends of flow evolution. The trends of 2D simulation results are expected and the evolution of flow and aerosol pollutants is found. However, the effects of spatial geometry among the radial direction were negligible. 3D simulation provides full information and highlights the effect of 3D blade profile, radial spacing, and rotor speed combinations on the HPT performance. The difference of value of chemical and flow parameters between 2D and 3D calculations in the HPT are investigated in this section.

3.2.1 Baseline 1D, 2D full HPT flow path calculation

2D results at the cylindrical surface of 50% span produced the evolution of $T(x)$, $P(x)$, $V(x)$ profiles through turbine blades are shown in Fig.3.1. The baseline 1D calculation, which corresponds to $\bar{T}(x)$, $\bar{P}(x)$ and $\bar{V}(x)$ in its traverse of the HPT, are presented in Fig.3.3.

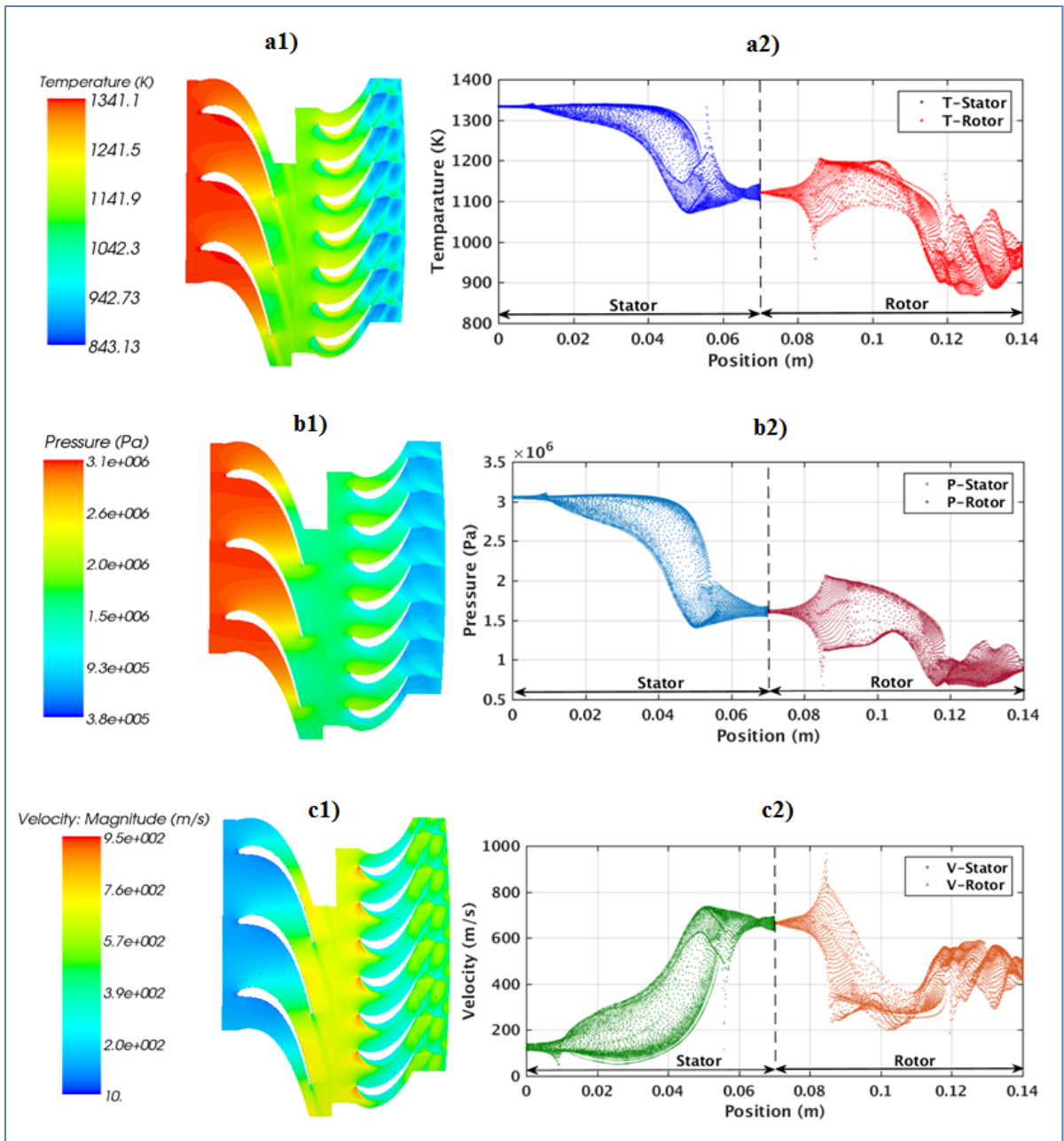


Figure 3.1 Temperature- (a1), pressure- (b1) and velocity- (c1) evolution and temperature- (a2), pressure- (b2) and velocity- (c2) value distribution in stator and rotor blades at the 50 % of the span

Fig.3.1 shows the evolution of three flow parameters: temperature (Fig.3.1a), pressure (Fig.3.1b), and velocity (Fig.3.1c). These figures converged a common point that stator and rotor leading edges form the wake into lumps of fluid, which enter the stator and rotor

passage. In the rotor, values of flow parameters strongly fluctuated after rotor trailing edges contributed by the additional effects of moving rotor. The source term of the moving rotor (S_M) effects finites ($\partial T / \partial x$, $\partial p / \partial x$, and $\partial U / \partial x$ in Eq. 2.1, Eq. 2.2, and Eq. 2.4) cause the total temperature, pressure, and velocity to vary [7, 80, 81]. The variation results of the flow parameters were in good agreement with the experimental results of Strickland et al. [82], Goldstein and Spores [83], Sieverding et al. [84], and Rose et al. [7, 80].

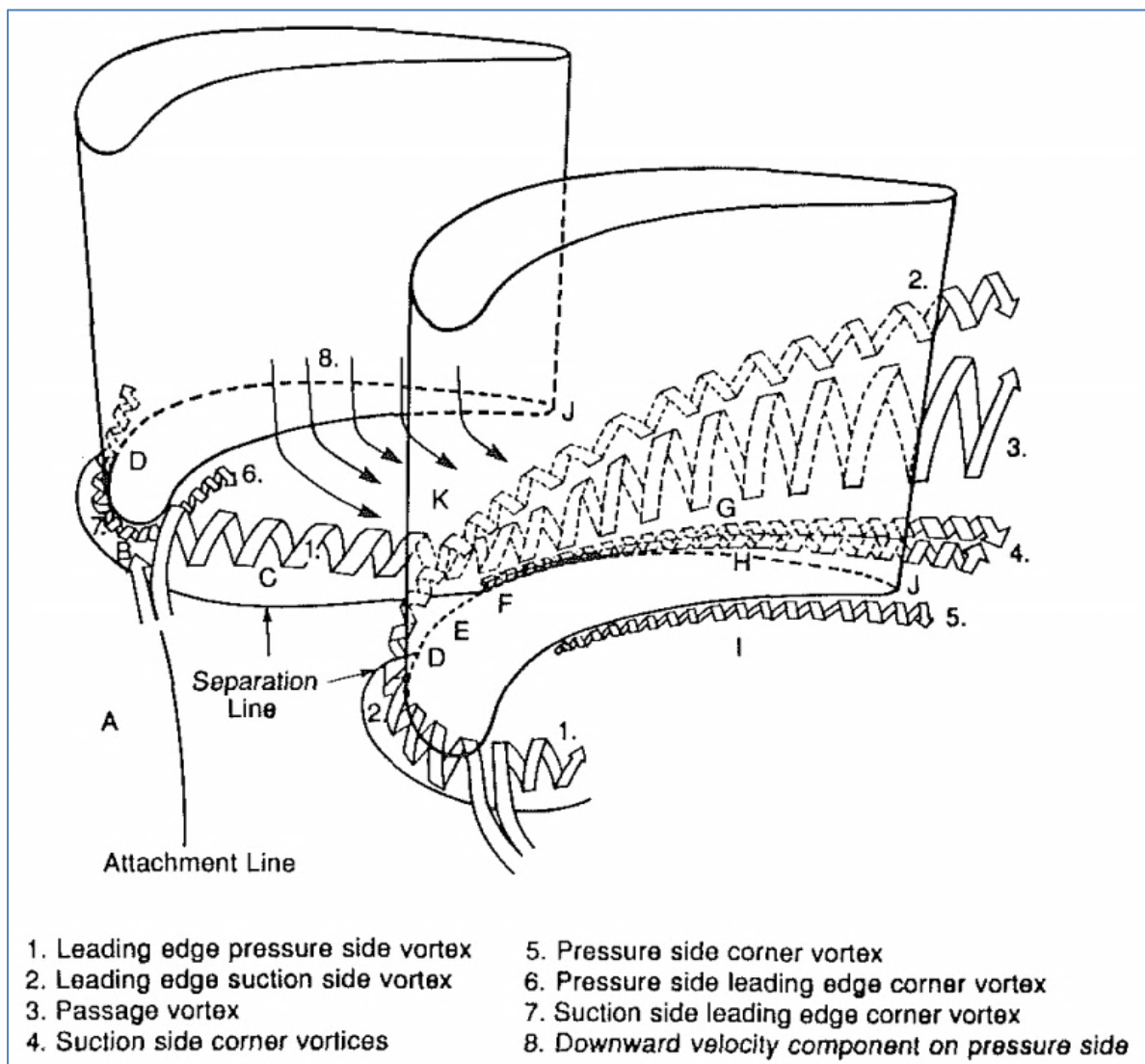


Figure 3.2 The three-dimensional flow field in the end wall region
 Taken from Goldstein et al. (1988, p. 864)

To better understand the mechanism forming the vortex from blade leading edges to blade trailing edges, Goldstein [83] combined various visualizations and measurements described in the literature, such as Marchal and Sieverding [85], Langston [86], Sieverding [87], and Sonoda [88]. This mechanism is illustrated in Fig.3.2. This figure shows the major vortices, labeled 1 through 7, and primary regions of interest, labeled A through K, in the turbine passage. The initial horseshoe vortex 1, 2 and passage vortex 3 are three big vortices. Sieverding [87] indicated that both vortex 1 (pressure side of the leading edge vortex) and vortex 2 (suction side of the leading edge vortex) lift off the end wall surface due to the higher average velocities and lower pressure, found away from the end wall along the suction surface. The two small vortices 4 and 5 originate just downstream of where the passage vortices lift off from region F of the end wall. Sonoda [88] observed that the pressure side corner vortex (vortex 5) became approximately 1/3 of the way back from the blade's leading to its trailing edge. The four vortices, 1, 2, 3, and 4, exist around the both stator and rotor blades but in vicinity of the rotor blades, additionally, they have two leading edge corner vortices (referring to vortices 6 and 7), which originate in the same region as the horseshoe vortex but have a rotation in the opposite direction.

It was observed, from Fig.3.1, that the temperature and pressure decrease throughout the turbine and the velocity of flow increases from stator inlet to stator outlet, and then decreases from mixing plane to rotor outlet. The decrease of temperature and pressure can be linked to losses (heat loss and pressure loss) in the HPT. The principal sources of these losses in the axial turbine, that were already reported by Wei [89] and discussed by many authors (Kacker and Okapuu [90], Moustapha [91], Denton [92, 93], Schobieri and Abouelkheir [94], Okan & Gregory-Smith [95], Yaras & Sjolander [96], Cecco [97], Wehner [98] and Chaluvadi [99]), are profile losses (due to blade boundary layers (including separated flow) on blade surfaces and wake through viscous and turbulent dissipation), shock losses (due to viscous dissipation across the shock), tip leakage losses (due to the clearance between the blade tip and the casing), and end wall losses (due to the secondary flow and formation of vortex result in mixing and dissipation of energy similar to those). Concerning the velocity variation in the HPT, the velocity gradient in stator is positive because the static enthalpy of temperature was then converted to kinetic energy. So, in the stator, the fluid was accelerated while the

temperature decreased in the rotation direction. In the rotor, the moving blades influence the absolute flow velocity and change their value; also the kinetic energy of the fluid is converted to kinetic energy of blade associated with the decrease in flow velocity in rotor [100].

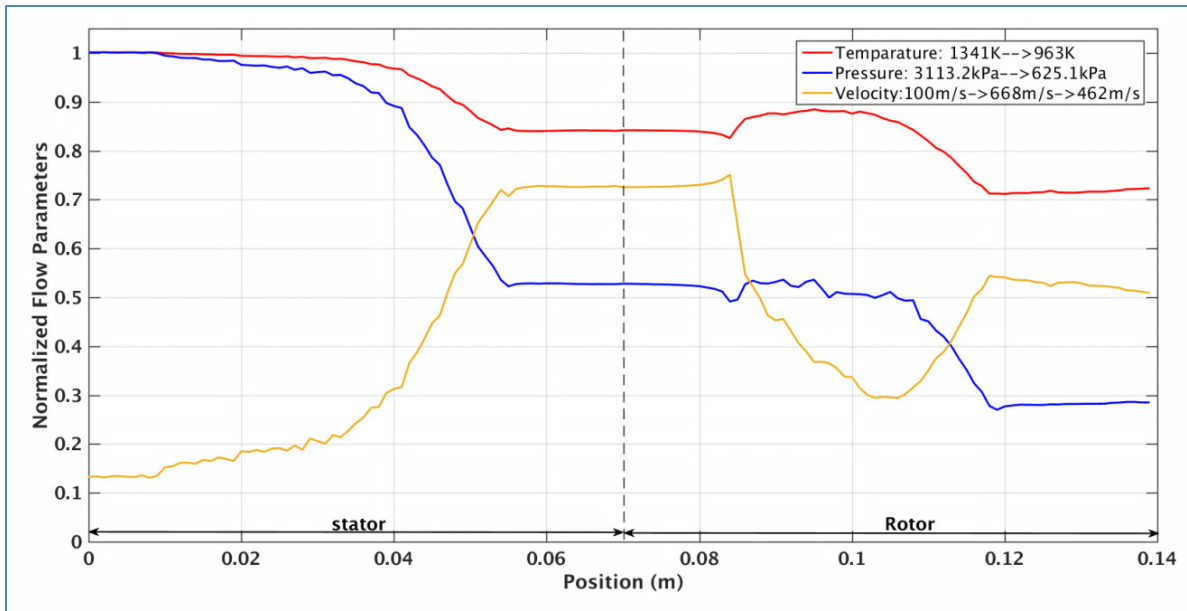


Figure 3.3 Temperature, pressure and velocity evolution in the flow from the combustor exit to the HPT exit

To simplify the flow evolution and to better understand the general tendency of the flow, the trend of flow parameters was presented in Fig.3.3 by 1D calculation, averaged from 2D calculation. In this figure, the temperature drops from 1341 K at the HPT inlet to 963 K at the HPT outlet. Similarly, the pressure passing on stator-rotor falls from 3113.2 kPa to 625.1 kPa. The velocity increases from 100 m/s to 668 m/s and then decreases to 462 m/s at the HPT outlet. In comparison to experiments reported by NASA Lewis Research Center [101] and previous studies for aerodynamic process in turbomachinery [4-6], the tendency of flow parameters has a good agreement with the previous results. In detail of this simulation, value of T_{outlet} / T_{inlet} is 0.72 (compared with 0.65 in the references); P_{outlet} / P_{inlet} is 0.28 (compared

with 0.2 in the references) and V_{outlet}/V_{inlet} is 3.57 (compared with 3.33 in the references). A little difference of values T_{outlet}/T_{inlet} and P_{outlet}/P_{inlet} may be due to difference of blade profiles used for the simulations and the real geometry in experiments.

3.2.2 Formation and distribution of NO_x and SO_x throughout of stator and rotor blade

This section discusses the formation of NO_x and SO_x , in particular formation of SO_3 and NO_2 (sources contribute to production of sulfuric acid and nitric acid via $\text{SO}_3 + \text{H}_2\text{O} \leftrightarrow \text{H}_2\text{SO}_4$ and $\text{NO}_2 + \text{OH} \leftrightarrow \text{HNO}_3$). During the formation of these acids, the conversion from SO_2 to SO_3 and NO to NO_2 , considered to be the key reactions, is also analyzed in this section. Fig.3.4 and Fig.3.6 present evolutions of NO_x and SO_x formations. It is found that the flow has significant impacts on chemical process and the formation of NO_x and SO_x principally occurs before stator blade's leading at high temperature and pressure.

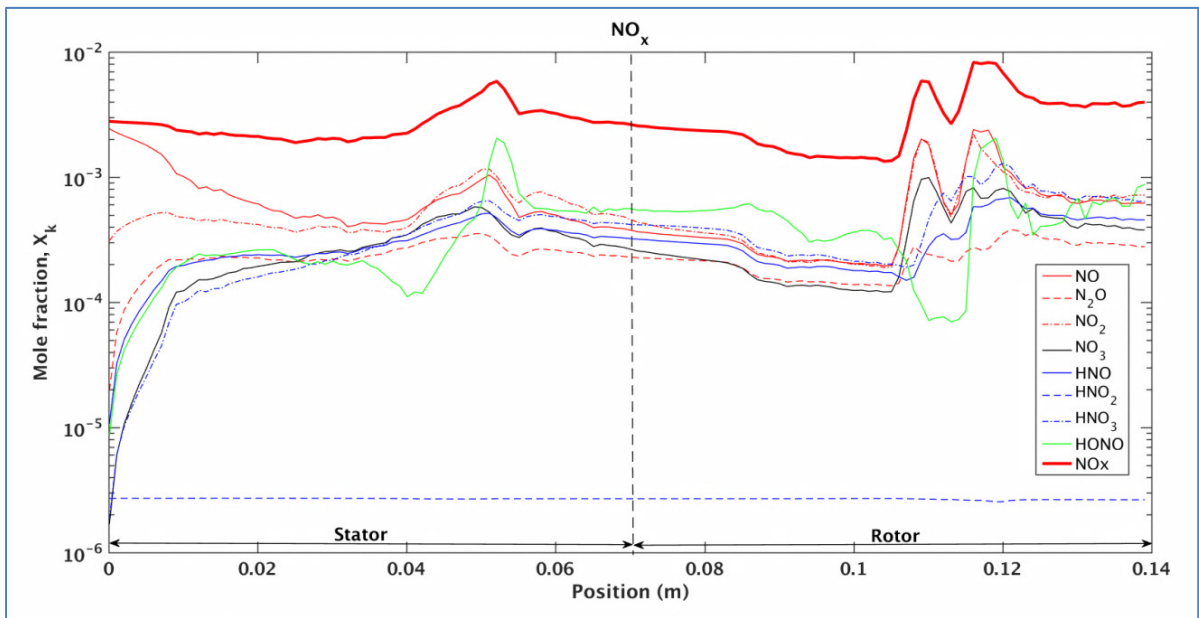


Figure 3.4 Baseline calculation results of $\overline{X}_{\text{NO}_x}$

Accordingly, the wake zones of aero-thermodynamic process that are discussed in the section 3.2.1, the formation of species strongly fluctuated in two zones: stator and rotor blade's trailing, in particular rotor blade's trailing where effects of moving rotor are identified. The fluctuation of aerosol formations was briefly demonstrated in Fig.3.5 in which the evolution of NO in the HPT is presented. This highlights the presence of significant influences due to blade profiles, flow parameter effects, and turbine function (rotation of rotor) which are very close, as suggested by Lyon and Bahr [102], Howard [103], Lukachko [5, 6], and Wey [10, 78], but the nature of their effects was not the same. This process possesses a direct kinetic effect through initial temperature and temperature field in the HPT [6, 102, 103] and has an indirect kinetic effect through velocity perturbation, dilution and thus changes in concentrations [5, 104].

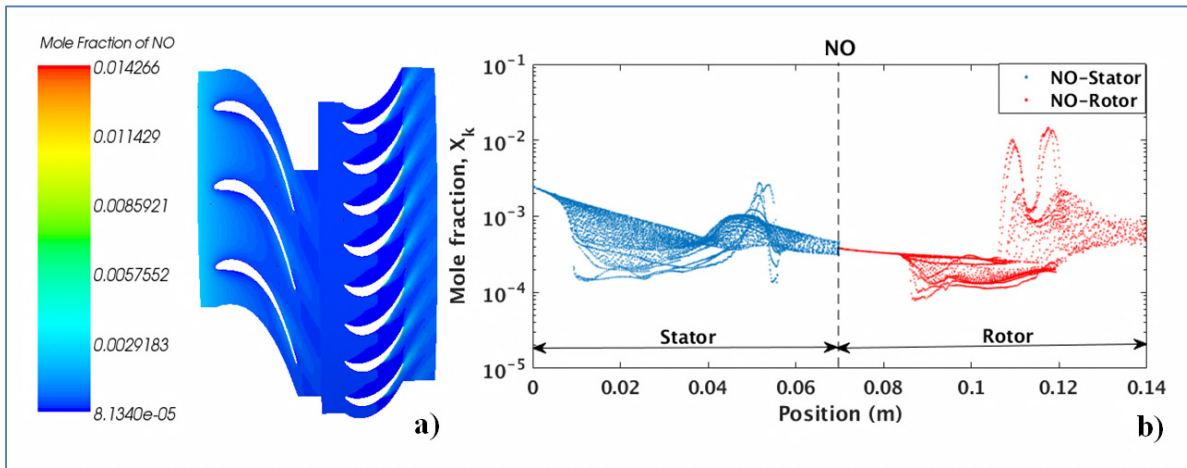


Figure 3.5 NO evolution (a) and NO value distribution (b) at the 50 % of the span

As illustrated in Fig.3.4, the emission gases are composed mostly of nitrogen pollutants. NO decreases in the HPT due to its conversion to NO_2 by oxidation [12] and leads to increase of NO_2 . In the other words, mole fraction of NO (X_{NO}) decreases from $2.52 \cdot 10^{-3}$ at the HPT inlet to $6.25 \cdot 10^{-4}$ at the HPT outlet and at the same time mole fraction of NO_2 increases from $2.80 \cdot 10^{-4}$ to $7.10 \cdot 10^{-4}$ or $X_{\text{NO}_2} / X_{\text{NO}_x}$ increases from 9.6 % to 17.8 %. Concerning the NO_2 formation, there are four principal pathways leading to NO_2 (two pathways via O, one via

OH and one via HO₂): NO + O ↔ NO₂; NO₂ + O ↔ NO + O₂; HONO + OH ↔ NO₂ + H₂O and NO + HO₂ ↔ NO₂ + OH; destruction by H has a minor role which contributes to NO₂ kinetics [5]. For the NO₂ production via O, the resultant impact on NO₂ can be either positive or negative; for the production via OH, increase of HONO in the turbine (Fig.3.4) favors the presence of NO₂. Although, there are four pathways to produce NO₂, Lukachko [5] showed that NO₂ was typically dominated via HO₂ by NO + HO₂ ↔ NO₂ + OH. In comparison with previous studies, the evolution of N-containing species (decrease of NO; increase of NO₂, N₂O and HONO) in the HPT completely agrees with the measurements and experiments of Glarborg [68], Mueller [62], Lukachko [5, 6], Wey [10, 11], Moriruzzaman, and Yu [12], Starik [14] and Bisson [13]; the stability of NO_x total mole fraction (Fig.3.4) can be found in [13]. The obtained values of the X_{NO_2} / X_{NO_x} ratio (9.6 % to 17.8 %) in the HPT (Table 3.1) are in a good agreement with measurements [14, 105], in which this ratio was detected in the range of 6 % - 23 % for different aircraft engines.

Table 3.1 Inlet to exit comparisons of \overline{X}_{NO_x,SO_x}

Species	Inlet (Mole fraction)	Outlet (Mole fraction)	Species	Inlet (Mole fraction)	Outlet (Mole fraction)
NO	2.52E-3	6.25E-4	HNO ₃	9.11E-9	6.37E-4
NO ₂	2.81E-4	7.10E-4	SO	2.63E-10	6.55E-5
NO ₃	8.36E-10	3.89E-4	SO ₂	2.05E-4	9.19E-5
N ₂ O	0.00	2.90E-4	SO ₃	6.42E-6	8.30E-5
HNO	2.32E-7	4.72E-4	HONO	0.00	8.99E-4
HNO ₂	2.71E-6	2.80E-6			

Concerning SO_x, Fig.3.6 shows the evolution of sulphate precursors. It is observed that the conversion from SO₂ to SO₃ strongly occurs in the zone near combustor exit (the turbine inlet) and the mole fraction of SO_x species strongly fluctuated again at the rotor's trailing by effects of blade profile and rotation of rotor. Recent modeling results demonstrated that at high pressures, where the conversion from NO to NO₂ strongly occurs, SO₃ is produced via

$\text{SO}_2 + \text{NO}_2 \leftrightarrow \text{SO}_3 + \text{NO}$ and at lower pressures, SO_3 appears through $\text{SO}_2 + \text{O}(+ \text{M}) \leftrightarrow \text{SO}_3(+ \text{M})$ [62]. Thus, at high pressure, the conversion of NO to NO_2 directly linked to conversion of SO_2 to SO_3 and kinetic coupling of NO_x and SO_x chemistry significantly reduces SO_2 . In detail, from the turbine inlet to the turbine outlet, mole fraction of SO_2 decreases from $2.05 \cdot 10^{-4}$ to $9.19 \cdot 10^{-5}$ and mole fraction of SO_3 increases from $6.42 \cdot 10^{-6}$ to $8.30 \cdot 10^{-5}$. The evolutions of SO_x in the HPT were in good agreement with the previous measurements [4-7, 14] and experiments [62, 68]. Fig.3.6 and Table 3.1 also show that the $X_{\text{SO}_3} / X_{\text{SO}_x}$ ratio changes from 3.03 % at the turbine inlet to 33.2 % at the turbine outlet while this ratio changes in the range of 3.0 %- ~53.3 % in the 1D calculations of Lukachko [6]. This difference can be due to effects of 3D geometry profile and rotation of rotor that will be represented in section 3.3.2.

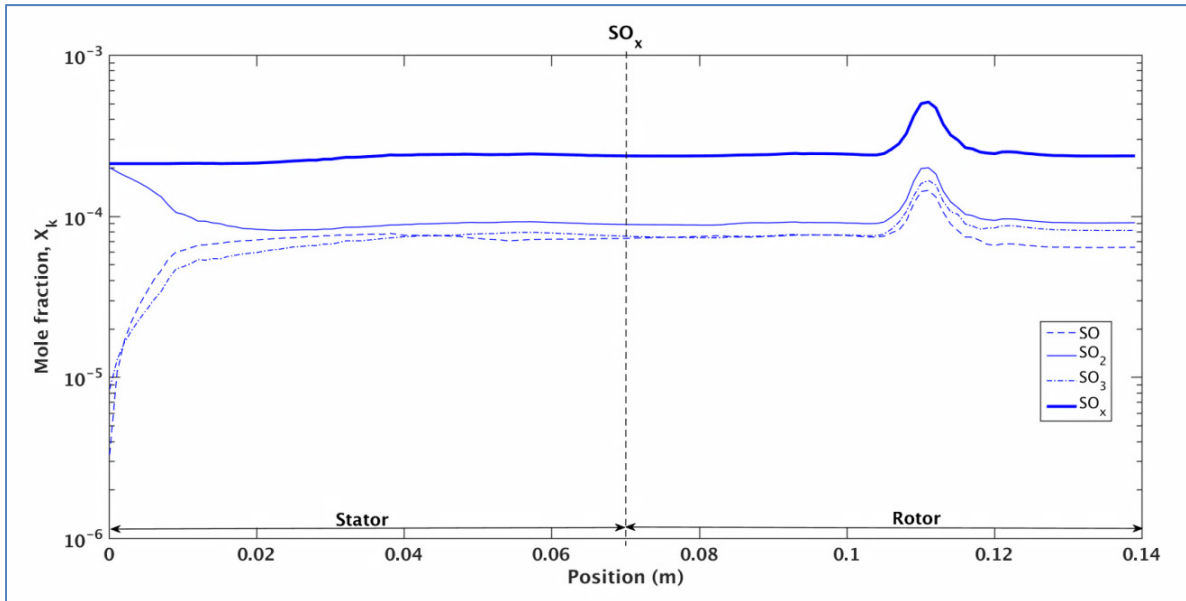


Figure 3.6 Baseline calculation results of $\overline{X}_{\text{SO}_x}$

Although the aero-thermodynamic parameters influence on the formation of species via the chemistry kinetics, chemical process exhibits a little effect on the aero-thermodynamic process as described in section 3.3.1.

3.2.3 Chemical effects on flow variation

To analyze chemical effects on flow parameters, Fig.3.7, Fig.3.8, and Fig.3.9 show the comparison of temperature, pressure, and velocity in two cases: with and without chemical reactions. Generally, flow parameter evolutions in two cases are very close, their baselines well follow up together and well agree with flow parameter evolutions as indicated in the previous studies and experiments of Marchal and Sieverding [85], Strickland et al. [82], Langston [86], Sonoda [88], Goldstein and Spores [83], Sieverding et al. [84, 87], and Rose et al. [7, 80]. The vortex of the flow in two cases briefly begins at stator blade's leading and develops among blade profile, the vortex strongly occurs in rotor where there are impacts of rotation, which were explained in detail in section 3.2.1. The chemical process had an effect on every flow parameter with different intensities. Fig.3.8 presents the temperature evolution in two cases: with and without chemical reactions. It indicated that the decrease of temperature with chemical reactions occurs more slowly than that without reactions.

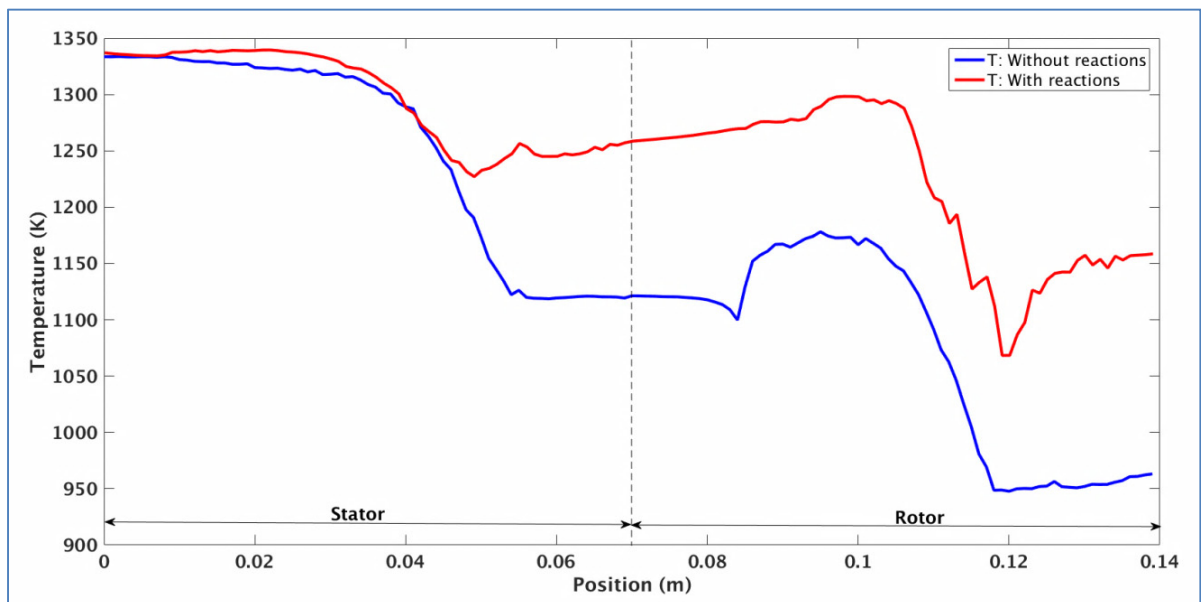


Figure 3.7 Variation of the temperature as a function of the axial distance with and without chemical reactions

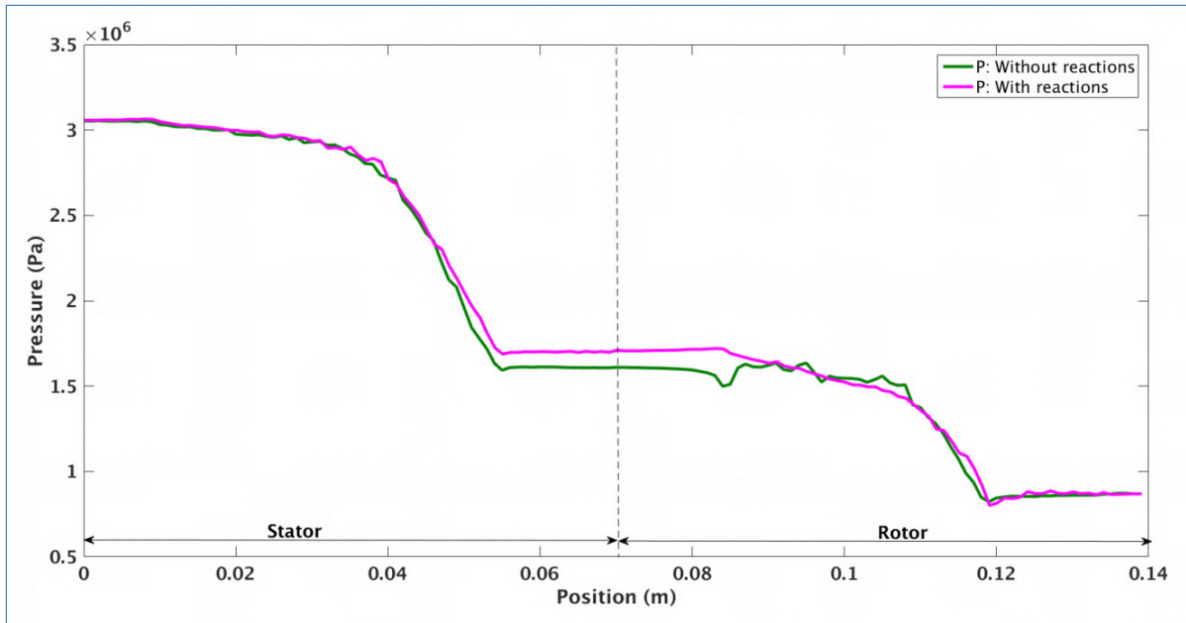


Figure 3.8 Variation of the pressure as a function of the axial distance with and without chemical reactions

The maintenance of temperature with reactions may be explained by influence of exothermic reactions in the HPT that have positive impact on contribution to the increase of temperature. The difference of temperatures between two cases mainly occurs from stator blade's trailing to the turbine outlet (including rotor) where concentration of the turbulence in the turbine exists. The maximum temperature difference between two cases was 16.9 % at the turbine outlet.

Similar to temperature and velocity evolutions in two cases, they are slightly different from stator blade's trailing, in particular, around mixing plane and after rotor blade's trailing. The maximum velocity difference is 38.8 %, near the mixing plane. Generally, it was found that the velocity value with reactions is lower than that without reactions. Reaction kinetics have negative impact on increase of flow velocity but the velocity value with reactions is higher at mid rotor blade, which may be due to the turbulence around this position. If the chemical process has strong impact on the temperature and velocity of the flow, the impact of this process on the pressure in the HPT is less pronounced than on the temperature and velocity (see Fig.3.8). The maximum difference in value of pressure in two cases is 5.8 % near mixing plane. This may be due to two reasons: firstly, there is no significant change of total mole

fraction of species in the HPT (Fig.3.4 and Fig.3.6) and secondly, the impact of chemical reactions on pressure is negligible in comparison with the other parameters, such as turbine geometry and losses of charge.

Quantitatively, values of proportion X_{outlet} / X_{inlet} in two cases, with and without reactions (X herein can be T , P and V), are, respectively, 0.86, 0.72 for T_{outlet} / T_{inlet} (compared with 0.65 in the measurements and experiments of references [5, 6, 14, 101]); 0.29, 0.28 for P_{outlet} / P_{inlet} (compared with 0.2 in the references) and 2.75, 3.57 for V_{outlet} / V_{inlet} (compared with 3.33 in the references). Thus, results in both cases are in a good agreement with the results in the references. Noted differences in the measurements are explained in discussion in section 3.2.1 and may be due to difference of blade profiles used for the simulations and the real geometry in experiments.

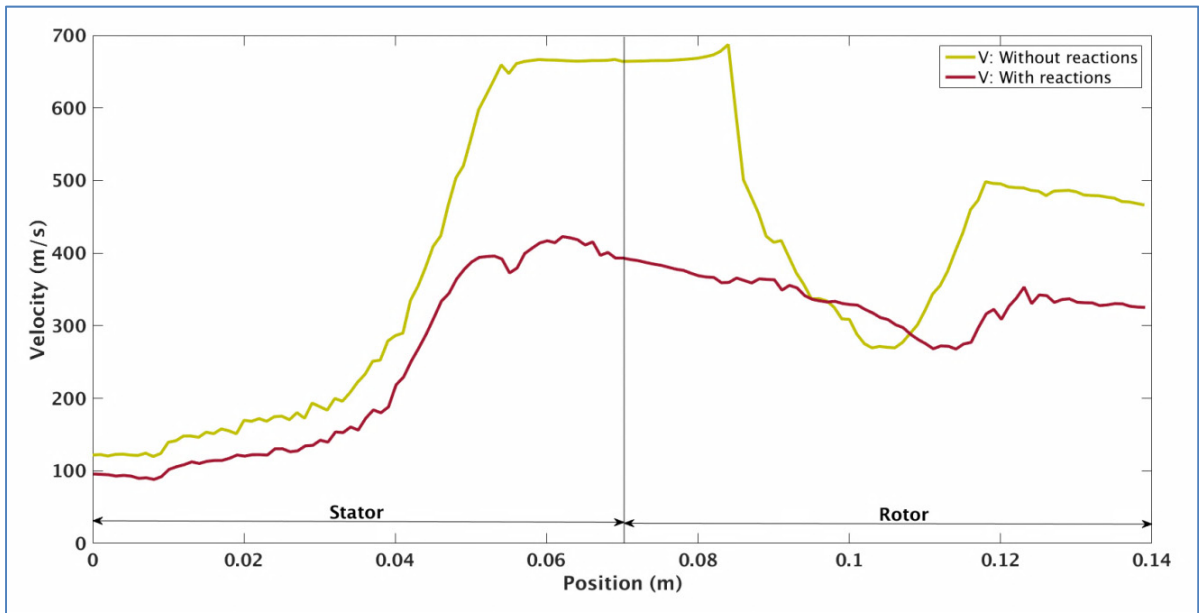


Figure 3.9 Variation of the flow velocity as a function of the axial distance with and without chemical reactions

3.2.4 Effect of 3D blade profile, radial spacing, and rotor speed combinations on the HPT performance

This section analyses effects of spatial geometry combined with turbine function (typically rotor speed) on some evolutions of flow parameters and species in the HPT. Fig.3.10, Fig.3.11, and Fig.3.12 show evolutions of temperature, turbulent kinetic energy (TKE), and NO aerosol distributed in three cylindrical surfaces at three different radial distances corresponding to 5 %, 50 %, and 95 % of the span. These figures demonstrate that the difference of evolutions principally occurs in the rotor where we have the fort change of blade profile among radial direction (Fig.2.3) and the impact of rotation at the different radius. The impact of rotor speed on the flow is represented via two aspects: first, aspect of flow parameter such as relative velocity (relative velocity in rotor is different at the different radial spacing because this velocity is proportional to radius r and angular speed ω via $V_{relative} = r * \omega$) and second, chemical formation of species via the dilution zones caused by rotor speed combined with spatial geometry. The change of blade's geometry formed the dilution zones and by effect of rotor blade rotation, the dilution zones also were created in the opposite rotation direction.

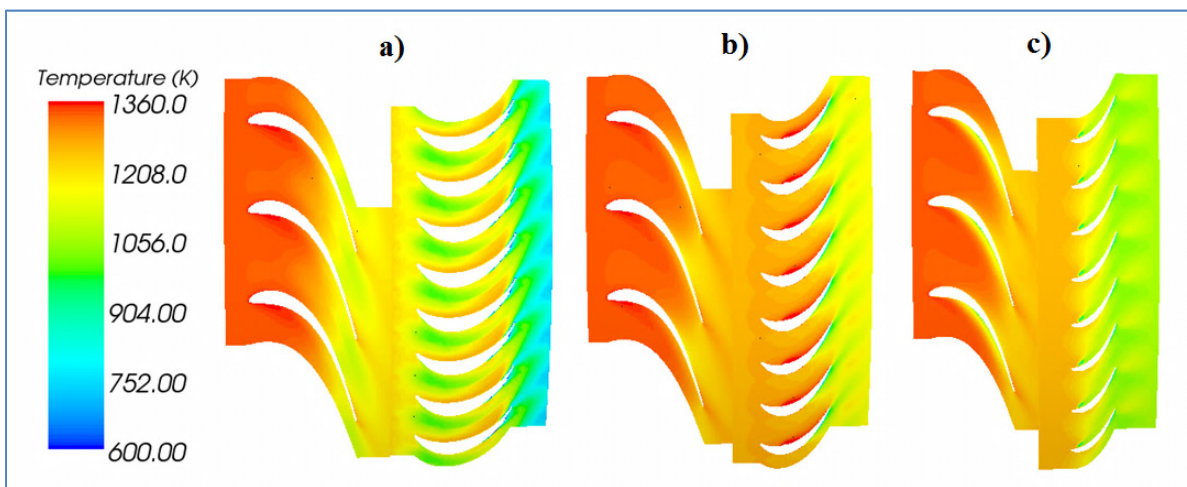


Figure 3.10 Temperature evolution at the 5 % (a), 50 % (b), and 95 % (c) of the span

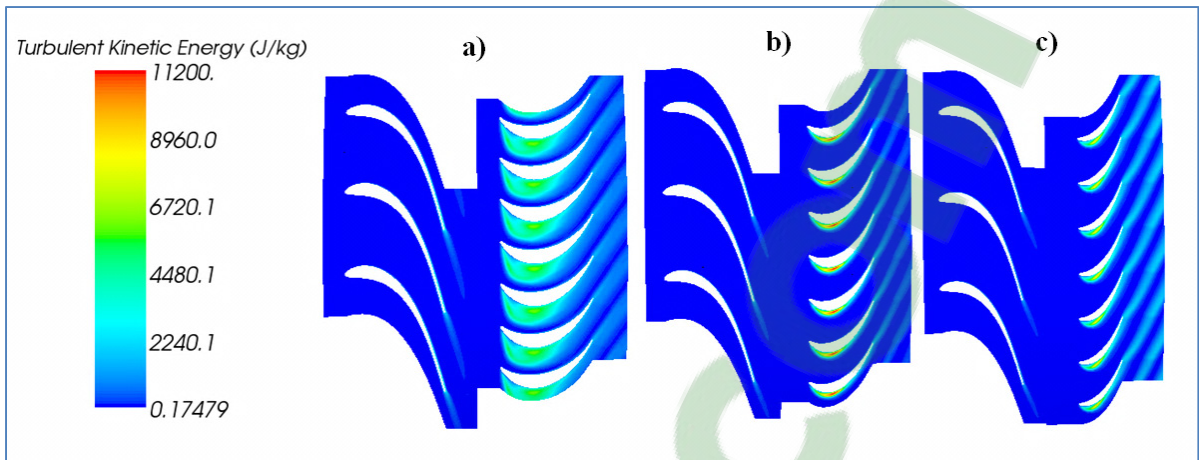


Figure 3.11 Turbulent kinetic energy (TKE) evolution at the 5 % (a), 50 % (b), 95 % (c) of the span

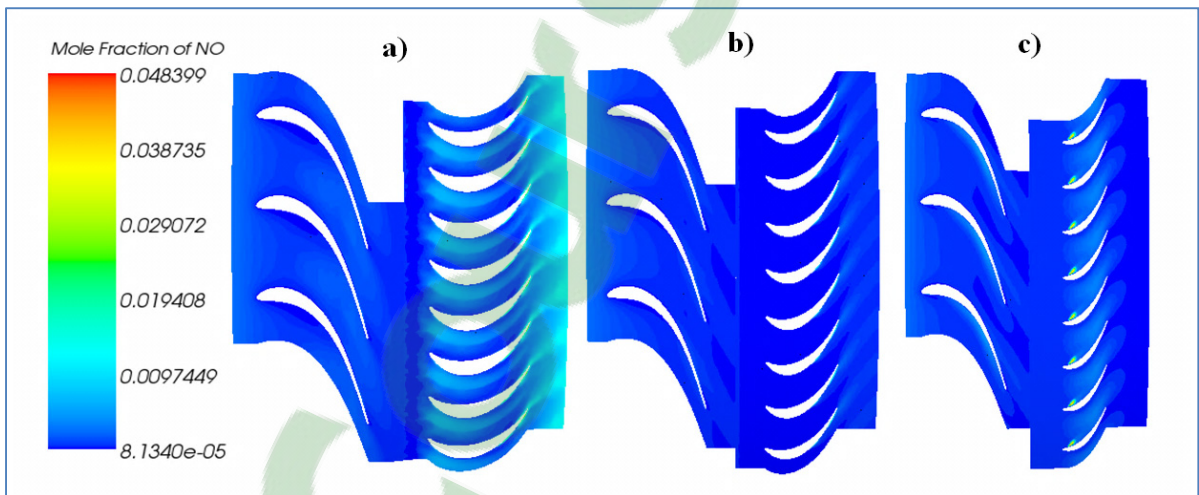


Figure 3.12 X_{NO} distributions at 5 % (a), 50 % (b), and 95 % (c) of the span

Fig.3.11 shows the distribution of turbulent kinetic energy (TKE) at 5 %, 50 %, and 95 % of the span. It is evident that TKE at 5 % of the span, exhibits the larger zone but lower value than that at 50 % and 95 % of the span. Nevertheless, with the same rotor speed, the change of radial spacing has an impact on the flow. The flow near hub of blade has lower relative velocity and has the fluid less compressible that implicates formation of dilution zones, increase the volume of turbulent zone, but decrease of TKE value near this region. By the

formation of dilution zone near rotor blade hub, the NO has elevated concentration at 5 % of the span (see Fig.3.12). Thus, 3D calculation provides full information on the study of aerothermodynamic and chemical transformations in every region in the turbine.

Furthermore, the effect of 3D spatial geometry, effect of difference radial distances, or impact of combination of radial distance and rotor speed can be analysed only by 3D simulations and not by 1D nor by 2D simulations. As illustrated in Fig.3.13 and Fig.3.14, observation of 1D baselines of temperature and NO distribution confirms that 1D calculation well produces only the trends of evolutions because the trends of temperature and NO distribution baselines at three percentages of the span are identical. But if we only use a 1D calculation or 2D calculation for every surface of 5 % or 50 % or 95 % of the span, it is found that there are differences of values between these surfaces. In comparison with the averaged value, the value difference may be up to 17 % for temperature at the HPT outlet (Fig.3.13) and up to 48 % for NO mole fraction at turbine outlet (Fig.3.14).

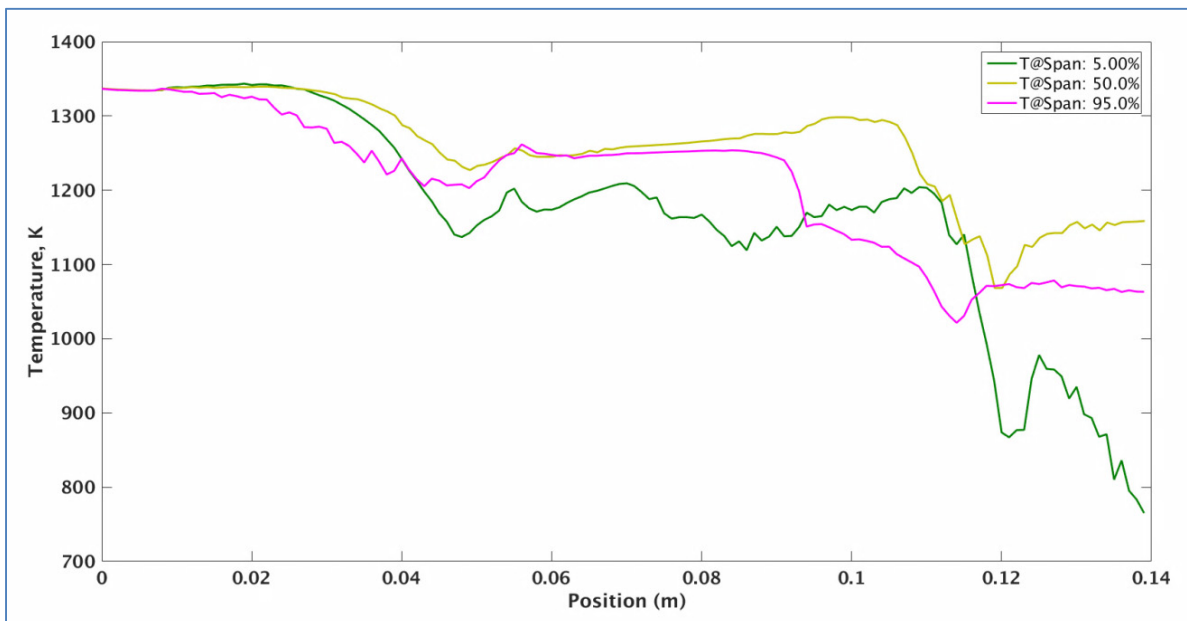


Figure 3.13 Temperature evolution at 5 %, 50 %, and 95 % of the span

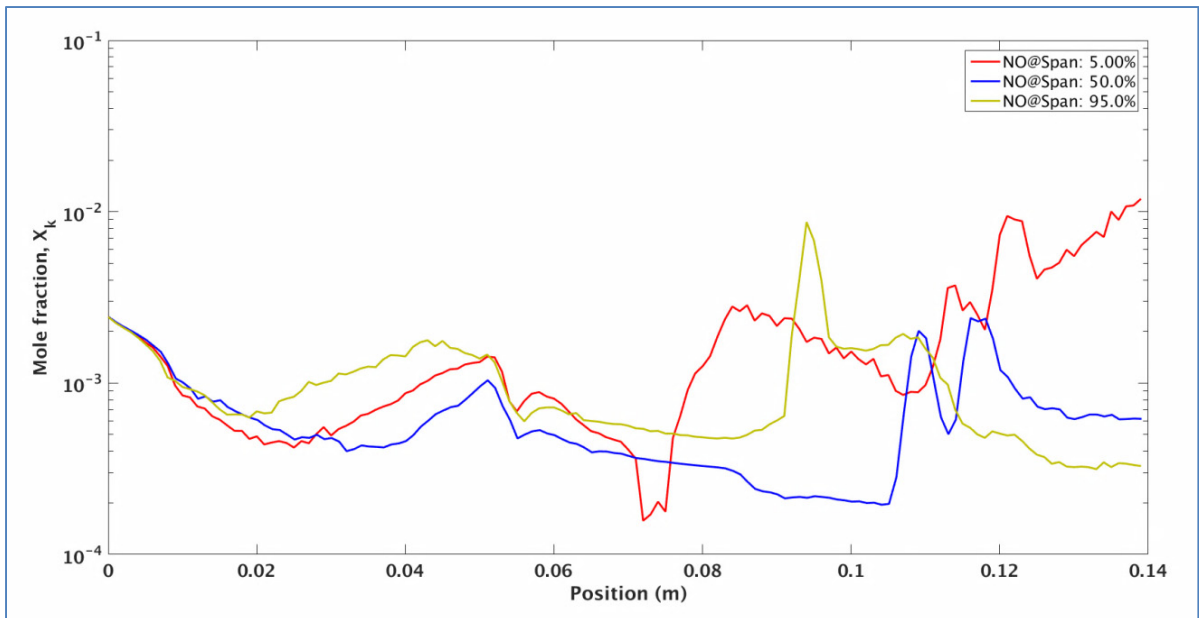


Figure 3.14 NO evolution at 5 %, 50 %, and 95 % of the span

3.3 Conclusion

Results of 3D modeling and calculations that simulate some complexity of actual intra-engine flows showed significant interactions between the geometrical parameters, operating condition of turbine (rotor speed), and physical and chemical processes including aerosol pollutant formation (NO_x and SO_x). The aero-thermodynamic process always influences the formation of chemical species and the chemical process also has relative impact on the flow parameters (value difference of aero-thermodynamic parameters with and without chemical reactions may be up to 17 % for temperature and 39 % for velocity).

Our analysis also indicated strong dissimilarities in aero-thermodynamic and chemical evolutions in the comparison of 1D/2D calculations with 3D calculations. The difference of parameters between these simulations can be up to 17 % for temperature and 48 % for NO mole fraction. Furthermore, the flexibility for the 3D HPT design in this research allows to widely apply this simulation for many different types of engine today.

Finally, this work brings new insights and provides useful information that may help to develop technologies of different types of engine and to reduce the pollution gases for environment in the future. In addition to improvements in these areas, future work will focus on the effects of initial conditions, the impact of different operating conditions, the impact of the reaction set, the stator-rotor interaction around mixing plane, the optimization of the HPT design, and details of 2D and 3D fluid-chemistry interactions, including the analysis of turbine cooling flows.

CHAPTER 4

EVALUATION OF THE RELATIONSHIP BETWEEN AERO-THERMODYNAMIC PROCESS AND OPERATIONAL PARAMETERS IN THE AXIAL HIGH PRESSURE TURBINE

Trung Hieu Nguyen^a, Tri Phuong Nguyen^b, Francois Garnier^a

^a TFT Laboratory, Ecole de Technologie Superieure (ETS), 1100 Notre-Dame St W,
Montreal, Quebec, Canada H3C 1K3

^b Department of Chemistry, University of Montreal (UdeM), 2900, Édouard-
Montpetit Boul., Montreal, Quebec, Canada H3C 3J7

This chapter has been submitted for the publication in the “*Aerospace Science and
Technology*” – Elsevier Publications, August 2017

4.1 Introduction

The gas turbine engines have been widely used in the air transport. The knowledge of aero-thermodynamic process in intra-engine (combustor, turbine and nozzle) is an important issue. That helps aircraft airline and manufacture to determine the performance of gas turbine engines, to ensure flight safety, to reduce maintenance cost and increase aircraft lifetime. Additionally, study the aero-thermodynamic parameters in the intra-engine can also decrease the losses, increase the efficiency and reduce the fuel consumption. In this context, many researchers attempted to investigate the aero-thermodynamic process in the combustor and the nozzle [5, 13, 14, 106-108]. However, the studies on the turbine components are very scarce, mainly because to access to a complete vision about the aero-thermodynamic process, it is indispensable to study this process in the different operational conditions of engine to approach the real function conditions of engine.

In fact, the research to study AT evolution in the turbine in a general level and especially in the high pressure turbine (HPT) is very rare in the literature. The complexities of AT process in the HPT are related to 3D design of complex blade profile, the simulation of the movement of one row (rotor) to the other (stator) (multi- rows), the influences of different operating conditions and effect of cooling system at rotor blade on the flow. Other

challenging relates to the computational cost of 3D calculations which requires a strong super-computer to calculate and simulate the complex flow in the HPT.

The 3D design of rotor and stator blades for high pressure turbine (HPT) remains a challenge in the field due to the complexity of HPT blade profile [32]. The 3D design of turbomachinery was realized by Demeulenaere [33] in which the fundamental geometry parameters of turbine such as hub and shroud radius, length of chord, ratio of chord, pitch of blades, flow inlet and outlet angles were started to use by 3D conception. The final blade was designed for an optimized pressure distribution. However the numerical simulation was not taken into account.

Concerning the numerical modeling of turbines, Rose et al. [7] used 2D URANS method to study the aero-thermodynamics in an axial turbine. The authors showed the transformation of wakes and their interactions with the rotor blades in the rotor. Besides the simulation results were compared with experiments. Nevertheless the multi-rows (stator-rotor) and their interactions, the effect of 3D geometry on the flow and the influence of operating conditions on the flow have not been discussed in this simulation.

Lampart et al. [8] used the RANS approach to realize the numerical simulation of 3D flow in an axial turbomachinery. The authors explained herein the transformation and distribution of flow parameters in the turbine. Additionally, the modification of blade profile was realized to increase the flow efficiency. However, the models were limited to simulate multi-rows (stator-rotor) with only three pairs of stator and rotor blades (quite small in comparison with the blade number of turbine engine in the reality) and the influence of cooling system as well as the effect of operating conditions on flow was still not considered in their investigation.

Yilmaz et al. [9] evaluated the relationship between exhaust gas temperature and operation parameters in the CFM-56 engines at two different power settings, including cruise and take-off via the data base from experiments. The author varied operation parameters including rotational speed, boundary temperature and fuel flow and studied its effect on the exhaust gas temperature. Wei et al. (APEX) [10, 11] also realized experiments to measure the emissions from gas engine and temperature of exhaust gas as a function of operating conditions.

However, the aero-thermodynamic process of intra-engine has not been discussed in these researches.

In this work, we bring new insights about the 3D design of the HPT (High Pressure Turbine) and 3D numerical evolution of aero-thermodynamic parameters for multi-rows turbine (stator-rotor), as functions of operational parameters in take-off and cruise of the CFM-56 engine which are widely used in airliners: Boeing 737, Airbus A320 family and A340. The distribution of these parameters, the effects of boundary temperatures, rotation speeds as well as cooling systems on behavior of flow and the non-uniformities of thermal field were calculated and simulated by using the turbulence modeling strategy RANS. The RANS approach in this research is an optimized option to study multi-row turbomachinery and both stationary and rotating blade row. In order to achieve these goals, our design processes as follows: (i) the HPT conception of gas turbine is performed by the module BLADE GEN, (ii) the STAR-CCM+ (CD-ADAPCO) software is used to simulate the aero-thermodynamic process and estimate the influences of different operating conditions on the aero-thermodynamic parameters, and (iii) the results are executed and analyzed with an in-house Matlab routine, and compared with that reported in the literature.

4.2 Aero-Thermodynamic losses in HPT

Fig.4.1 shows the temperature and pressure evolutions in the HPT. It is observed that both of temperature and pressure decreased from the turbine inlet to turbine outlet that can be directly linked to temperature and pressure losses in the turbine. There are some typical sources of losses in the turbine: profile losses, shock losses, tip leakage losses, endwall losses and cooling loss. The profile losses occurred principally at stator and rotor TE. In the rotor, the trailing vortex mixing with rotational speed produces the complex flow and contributes to the rotor losses [109]. Concerning the shock loss, the shock loss is pronounced at the leading edge blade of the stator and the rotor, this is special true with the pressure evolution (Fig.4.1b). The tip leakage losses defined as the clearance between the blade tip and the casing, with the unshrouded blade in this work, can be negligible. With the same behavior of

the profile losses, in the HPT the endwall losses concentrated especially at rotor TE. Concerning the cooling loss, in this research, a simplified modeling of cooling was used and the effect of this process will be discussed in detail in section 4.3.3. The cooling losses herein are mainly due to the modification of transition near boundary layer.

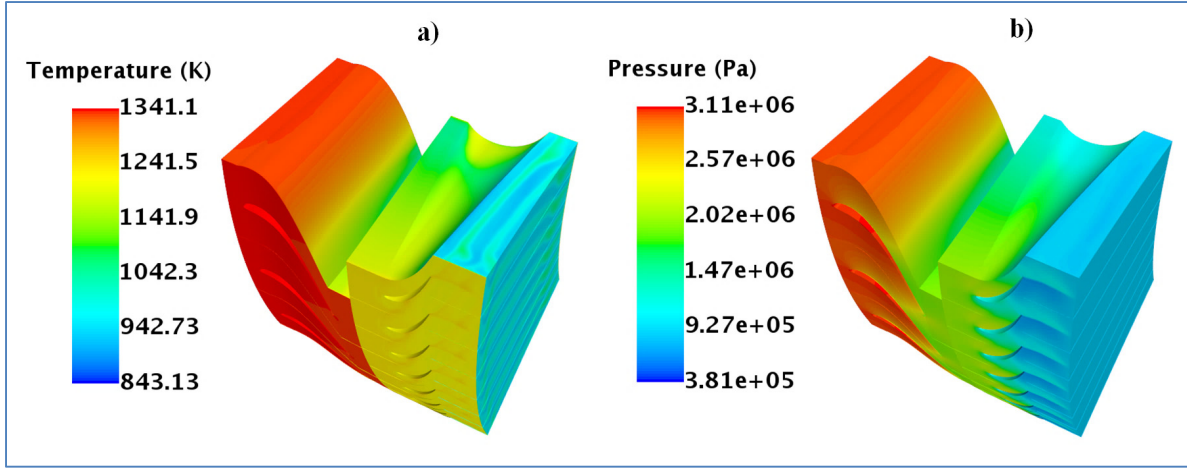


Figure 4.1 Temperature and pressure evolutions in the HPT

Nevertheless, the decrease of temperature and pressure are directly linked to five principal types of losses. But in many instances, it is difficult to distinguish between them because of their interaction and mixing. There are many papers published on the loss source [91, 94-98, 110], in which the losses in the turbine are used to be expressed in terms of loss coefficients. The authors studied the loss coefficients with various loss prediction methods but the total losses are always calculated as following:

$$\zeta = \sum \zeta_i \quad (4.1)$$

In the stator:

$$\zeta_N = \zeta_{pr,N} + \zeta_{sh,N} + \zeta_{tl,N} + \zeta_{ew,N} + \zeta_{co,N} \quad (4.2)$$

In the rotor:

$$\zeta_R = \zeta_{pr,R} + \zeta_{sh,R} + \zeta_{tl,R} + \zeta_{ew,R} + \zeta_{co,R} \quad (4.3)$$

where, ζ enthalpy loss coefficient; ζ_i component loss coefficient; $\zeta_N, \zeta_{pr,N}, \zeta_{sh,N}, \zeta_{tl,N}, \zeta_{ew,N}, \zeta_{co,N}$ stator loss coefficient, stator profile loss coefficient, stator shock loss coefficient, stator tip leakage loss coefficient, stator endwall loss coefficient and stator cooling loss coefficient respectively; $\zeta_R, \zeta_{pr,R}, \zeta_{sh,R}, \zeta_{tl,R}, \zeta_{ew,R}, \zeta_{co,R}$ rotor loss coefficient, rotor profile loss coefficient, rotor shock loss coefficient, rotor tip leakage loss coefficient, rotor endwall loss coefficient and rotor cooling loss coefficient respectively.

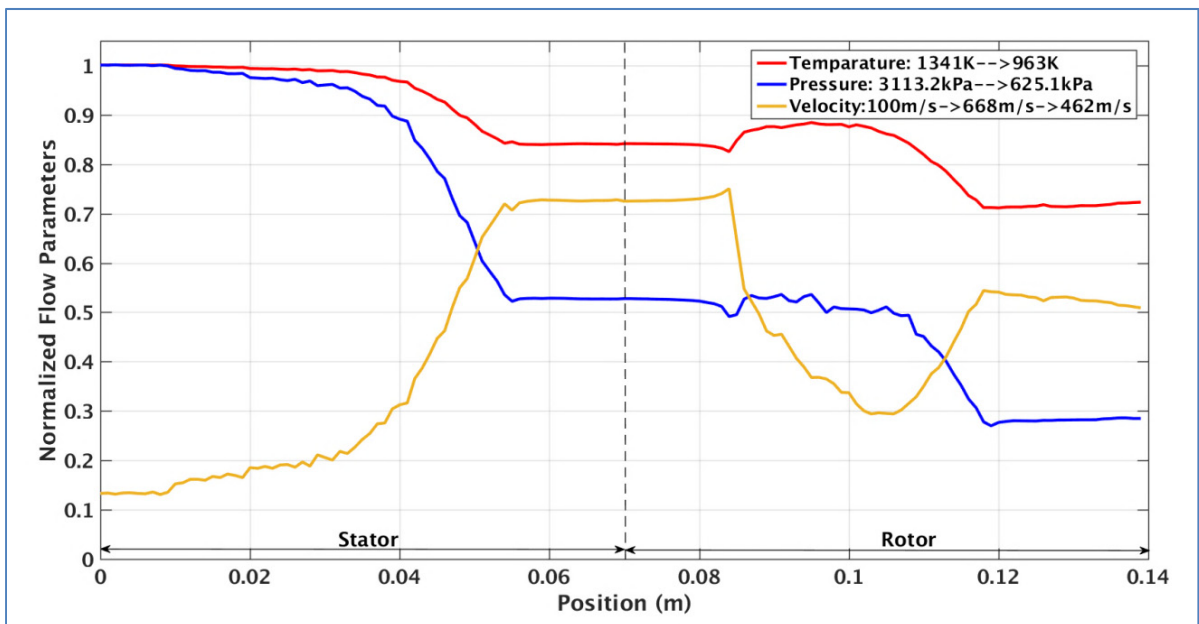


Figure 4.2 Temperature, pressure and velocity evolution from the combustor exit to the HPT exit

To study the general gradient evolution of flow, baselines of flow parameters are realized under the 1-D calculation result that are averaged from 2D cylindrical surface of the HPT at the 50% span as shown in Fig.4.2. It was found that the velocity gradient was positive in the stator and negative in the rotor while the temperature and pressure gradients were negative throughout the HPT. The increase of velocity in the stator could be explained by the transfer of static enthalpy of temperature into kinetic energy. So, in the stator, the fluid was accelerated while the temperature decreased in the rotation direction. In the rotor, relative to the moving blades that directly influence relative flow velocity and then absolute velocity

and change their value; also the kinetic energy of the fluid is converted to kinetic energy of the blade associated with the decrease of the flow velocity in rotor [100].

Fig.4.2 displays the temperature, pressure and velocity evolutions from the combustor exit to the HPT exit. It can be seen that the temperature drops from 1341 K at the HPT inlet to 963 K at the HPT outlet; similarly, the pressure passing on stator- rotor falls from 3113.2 kPa to 625.1 kPa. The velocity increases from 100 m/s to 668 m/s at “mixing plane” and then decreases to 462 m/s at the HPT outlet. In comparison with the previous experiments reported by Nasa Lewis Research Center [111-113] and others works on the aerodynamic evolution in turbomachinery [4-6], the tendency of flow parameters observed in this work has a good agreement with the previous results in the literature. In detail, value of T_{outlet} / T_{inlet} in this simulation is 0.72 (compared to 0.65 in the references); P_{outlet} / P_{inlet} is 0.28 (compared to 0.2 in the references) and V_{outlet} / V_{inlet} is 3.57 (compared to 3.33 in the references). A little difference of these values may be due to difference of the blade profile used between this simulation and the real geometry in the experiments. This influences directly the value of losses (especially profile losses) and aero-thermodynamic transformation implicating change of flow parameter values including T_{outlet} / T_{inlet} , P_{outlet} / P_{inlet} and V_{outlet} / V_{inlet} .

4.3 Evaluation of the relationship between aero-thermodynamic process and operational parameters

In this research, we realize all the simulations with different operating conditions. The boundary conditions (Table 2.1) are used. In the section 4.3.1, we studied the influences of thermal field changes in two cases of operating condition on the HPT flow: take-off and cruise that had a large different value of temperature at boundary condition (1554 K at the HPT inlet for take-off and 1341 K for cruise) [9, 114, 115]. In the section 4.3.2 the effect of rotor speed during the operating cruise has been investigated. Two different rotor speeds are computed in which one value at 8500 rpm corresponding to a normal rate of the operating cruise while other at 15183 rpm is the maximum operational speed of the turbine [4, 5]. In

the section 4.3.3, the cooling temperature in rotor blade depends on engine types and rotor blade materials [112, 116]. We report here the obtained results for the simulated internal cooling in three cases, 1) an adiabatic blade boundary condition, 2) the wall temperature set at 870 K corresponding to blade material by Titanium- based alloys, 3) the wall set at 990 K corresponding to the blade material by Nickel- based alloys. The section 3.5 discusses about the complexities of non-uniformities of thermal field distribution under effects of 3D spatial turbine blade profiles, operating conditions, radial and axial spacing in the turbine.

For each simulation, more than one million iterations, according to the positions of HPT, were used to solve equations, resulting in high resolution in both space and time. The Acceleration Factor of calculation convergence was chosen 0.2 (can be set from 0 (slow but stable) to 1 (fast but least stable)) and, finally, the stopping criteria of satisfaction was chosen 10^{-6} .

4.3.1 Influence of the initial temperature field in cruise and take-off

Fig.4.3 presents the temperature evolutions in two cases of initial temperatures: cruise (1341K) (a) and take-off (1554.5 K) (b) at the 50% span. In this figure, the temperature gradient evolutions are much closed, and just different about their values. It is found that the vortex concentrated principally in two zones of the turbine around leading edges and trailing edges of blades. The ‘horseshoe vortex’ and small leading edge corner vortices appeared at leading edges and formed the wake into lumps of flow, which enter the stator and rotor passage; the passage vortex strongly occurred after stator and rotor trailing edges, especially after rotor trailing edges contributed by the additional effects of moving rotor. The vortex production in this calculation was in line with that reported in the literature [83, 85-88]. About the temperature value, with the increase of the initial temperature, the temperature was falling from 1554 K to a minimum of 969 K in take-off while it was rapidly dropped from 1341 K to 843 K in the cruise.

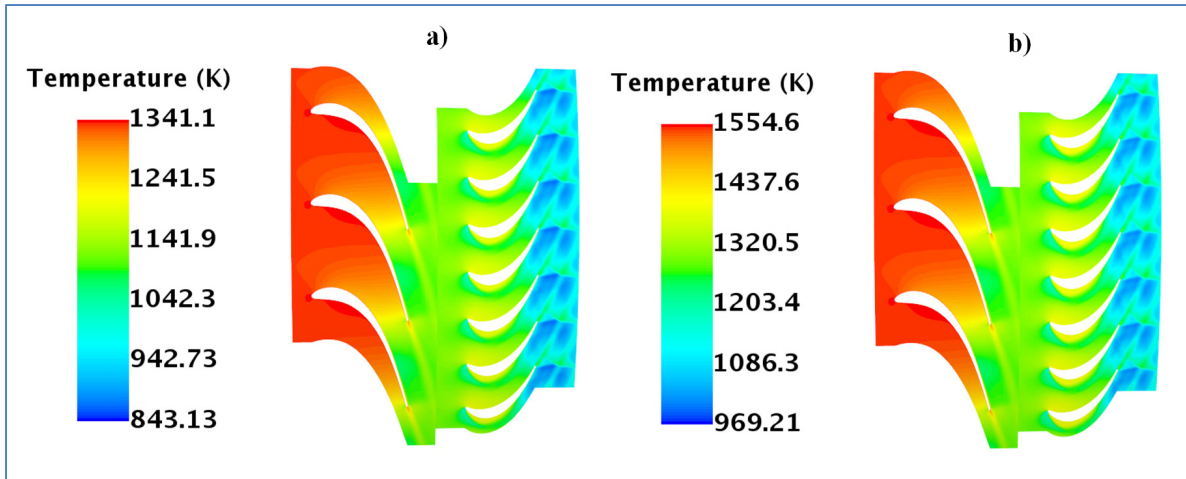


Figure 4.3 Temperature evolutions in two cases of initial temperatures: cruise (1341K) (a) and take-off (1554.5 K) (b) at the 50% of the span

The temperature value distributions and temperature evolution gradient were presented in Fig.4.4. This indicates that the temperature values of take-off were always higher than that in the cruise, which can be explained by the increase of initial temperature causing directly the increase of enthalpy. The later leads to an increase of the temperature field throughout the HPT as shown in Fig.4.4c.

If the temperature at the HPT inlet has a significant effect on the thermal field, this parameter seems to have no significant impact on pressure field (Fig.4.5). This figure clarifies that the difference of pressure between two cases, which occurred around rotor blades, is negligible because the highest value is found to be nearly of 3.2 %. On the contrary, the temperature change has a strong effect on the velocity field (Fig.4.6). The difference of velocities in two cases is found to be concentrated at ‘mixing plane’ and the turbine outlet where vortices are generated. The highest difference of velocities was about 11.5 % at the turbine outlet. Fig.4.6 shows also that the velocity of take-off was always more important than that in cruise because of the increase of temperature causing the increase of static enthalpy that thus accelerated the transfer of the static enthalpy into kinetic energy. The consequence of this process made the velocity field value to be higher. With the same reason, the increase of

kinetic energy caused the increase of turbulent kinetic energy (TKE) of take-off as shown in Fig.4.7, the gradients of TKE in two cases were quite similar and only their values were different.

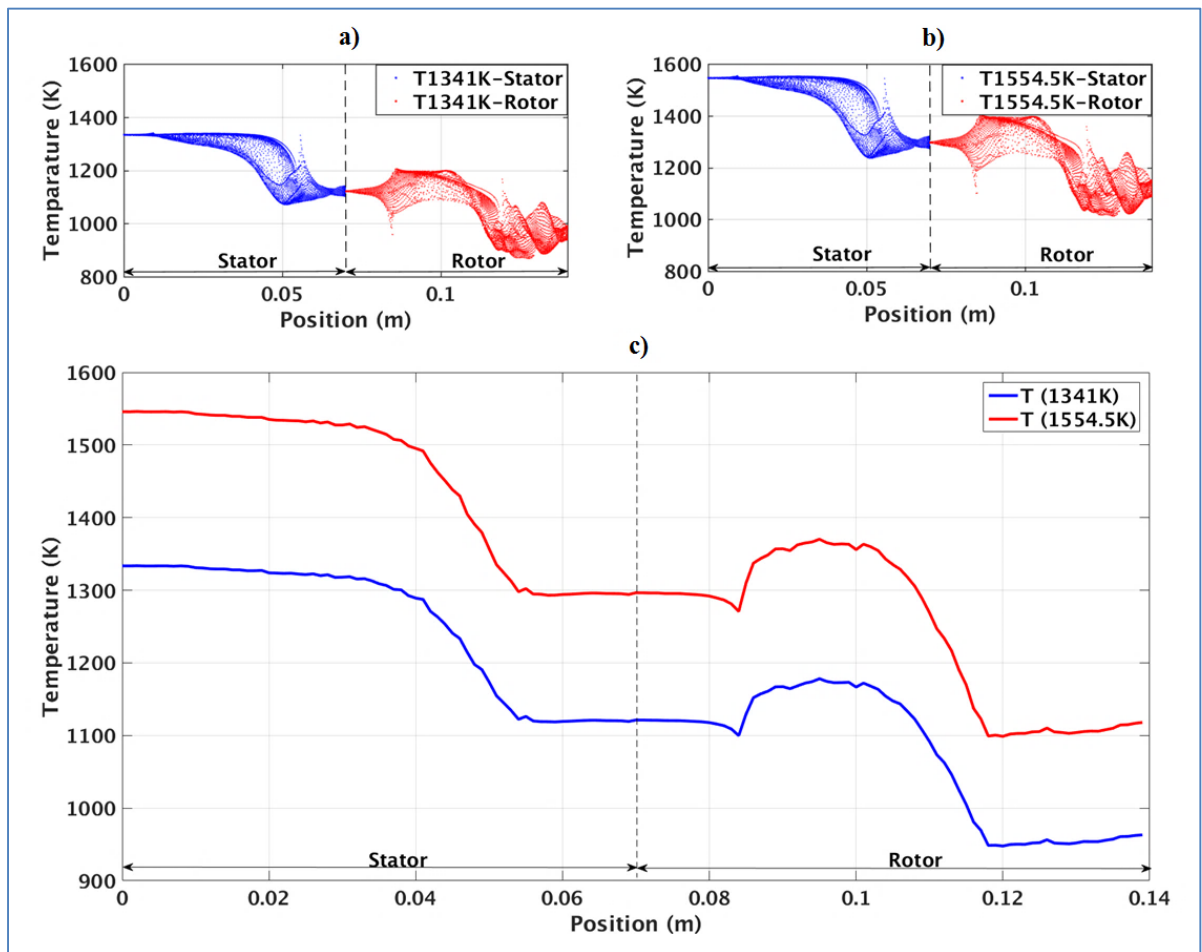


Figure 4.4 Temperature distributions (a, b) and temperature variations (c) in two cases of initial temperatures: cruise (1341K) and take-off (1554.5 K)

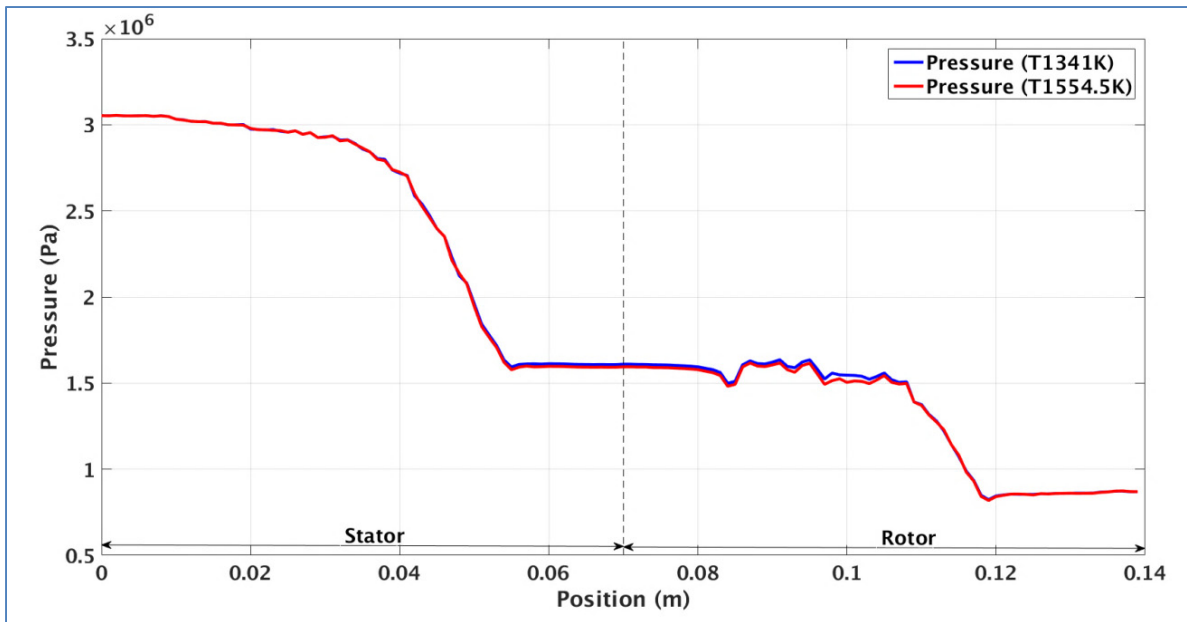


Figure 4.5 Variations of the pressure as a function of the axial distance in two cases of initial temperatures: cruise (1341K) and take-off (1554.5 K)

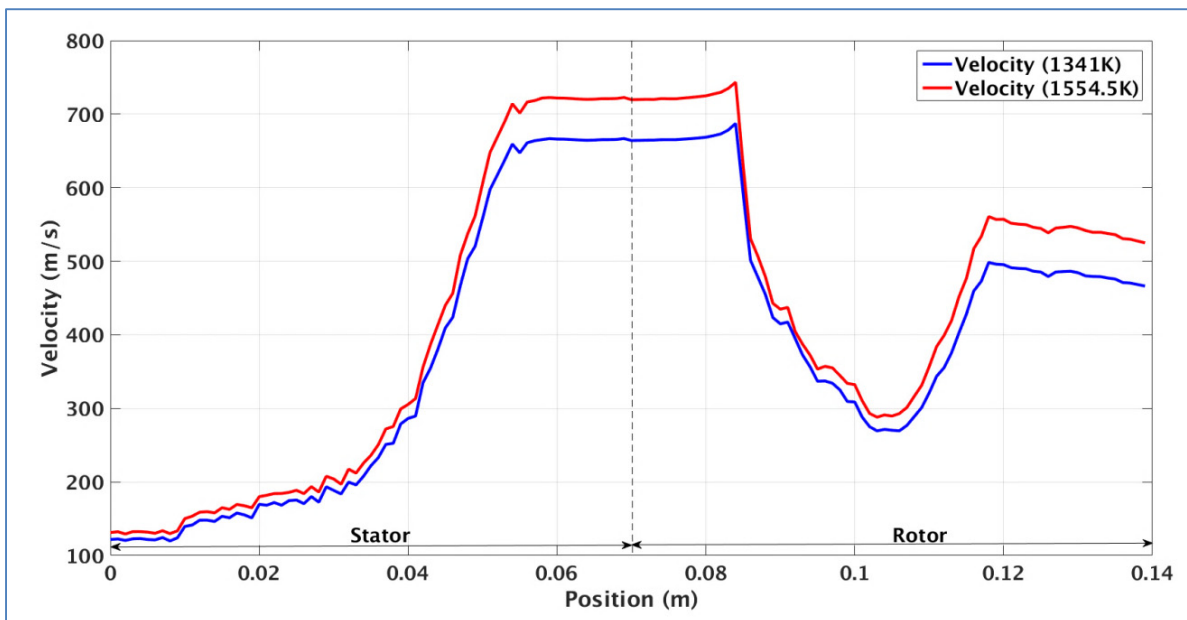


Figure 4.6 Variations of the velocity as a function of the axial distance in two cases of initial temperatures: cruise (1341K) and take-off (1554.5 K)

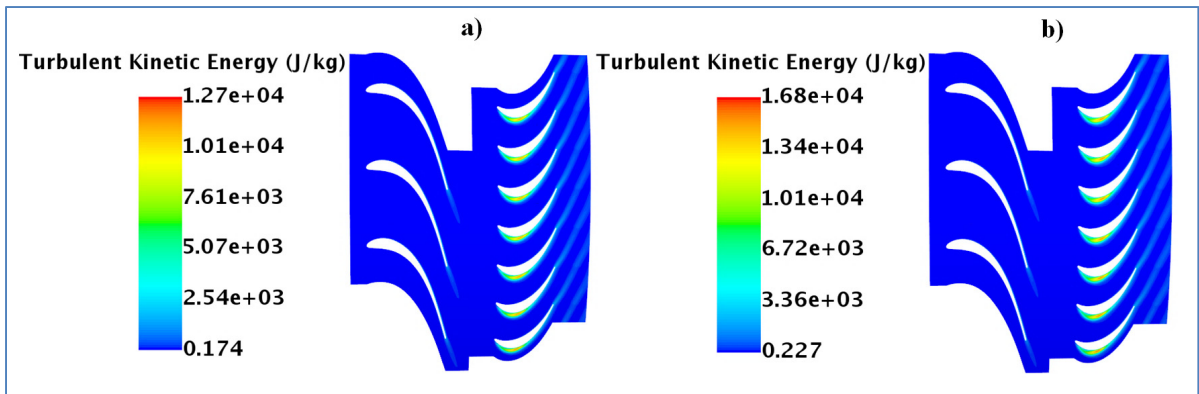


Figure 4.7 Turbulent kinetic energy (TKE) evolution in two cases of initial temperatures: cruise (1341K) and take - off (1554 K)

4.3.2 Influence of rotor speed in two cases: operating cruise and maximum rotor speed

Figs. 4.8-4.10 show the temperature, pressure and velocity distribution in the stator and the rotor for two different rotor speeds: 8500 rpm corresponding to a normal rate of the operating cruise and 15183 rpm corresponding to a maximum operational speed of the turbine. The distribution of flow parameter values exhibits a homogeneous distribution from stator inlet to trailing edge (TE) of stator blades in two cases. However, the difference of flow parameters appears behind stator blade TE to the turbine outlet. In this area the flow in the rotor seems to have a tendency to be compressed and thus the fluctuation of temperature, pressure and velocity values in the rotor is observed to be lower than that in the operating cruise. The flow parameter values were not different in front of stator blade TE in two cases because the change of rotor speed occurred only in the rotor and the effect of this change in front of the stator blade TE was negligible.

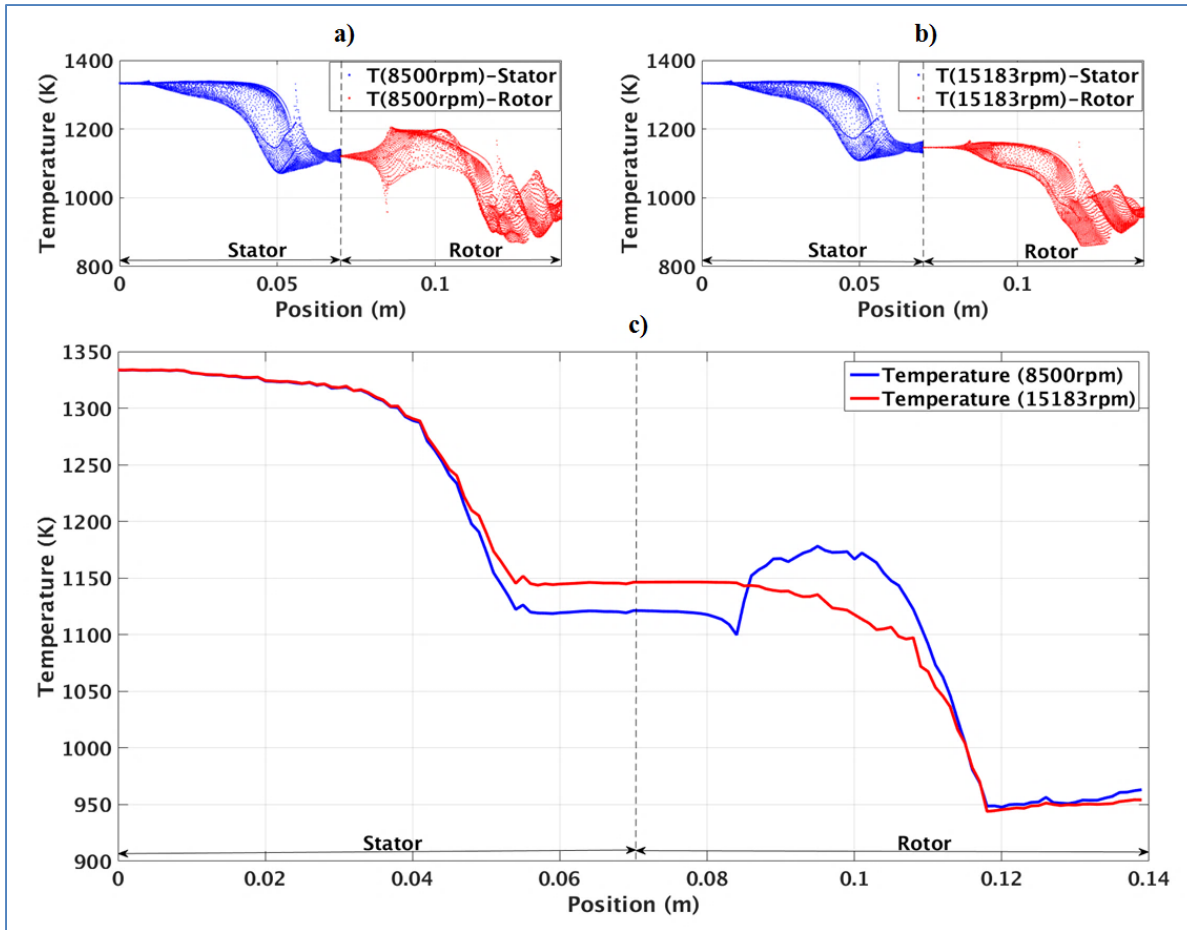


Figure 4.8 Temperature distributions (a, b) and temperature variations (c) in two cases of rotor speed: 8500 rpm and maximum 15183 rpm

Although, the effect of the rotor speed on each flow parameter (temperature, pressure and velocity) was different. It was remarkable that the influence of the rotor speeds on pressure and temperature were not important (Figs.4.8c and 4.9c); the difference of temperature and pressure occurred principally around ‘mixing plane’ and rotor blade corresponding to the interactions of stator and rotor regions, vortex around rotor blade and pressure difference between pressure side and suction side. The maximum difference of temperatures was 4.3 % at rotor blade and the maximum difference of pressure in two cases was equal to 22.6 % at the ‘mixing plane’; the difference at the turbine outlet for temperature and pressure were equal to 1 % and 0.4 % respectively. Oppositely, the influence of rotor speed on velocity field was more remarkable with the temperature and the pressure field

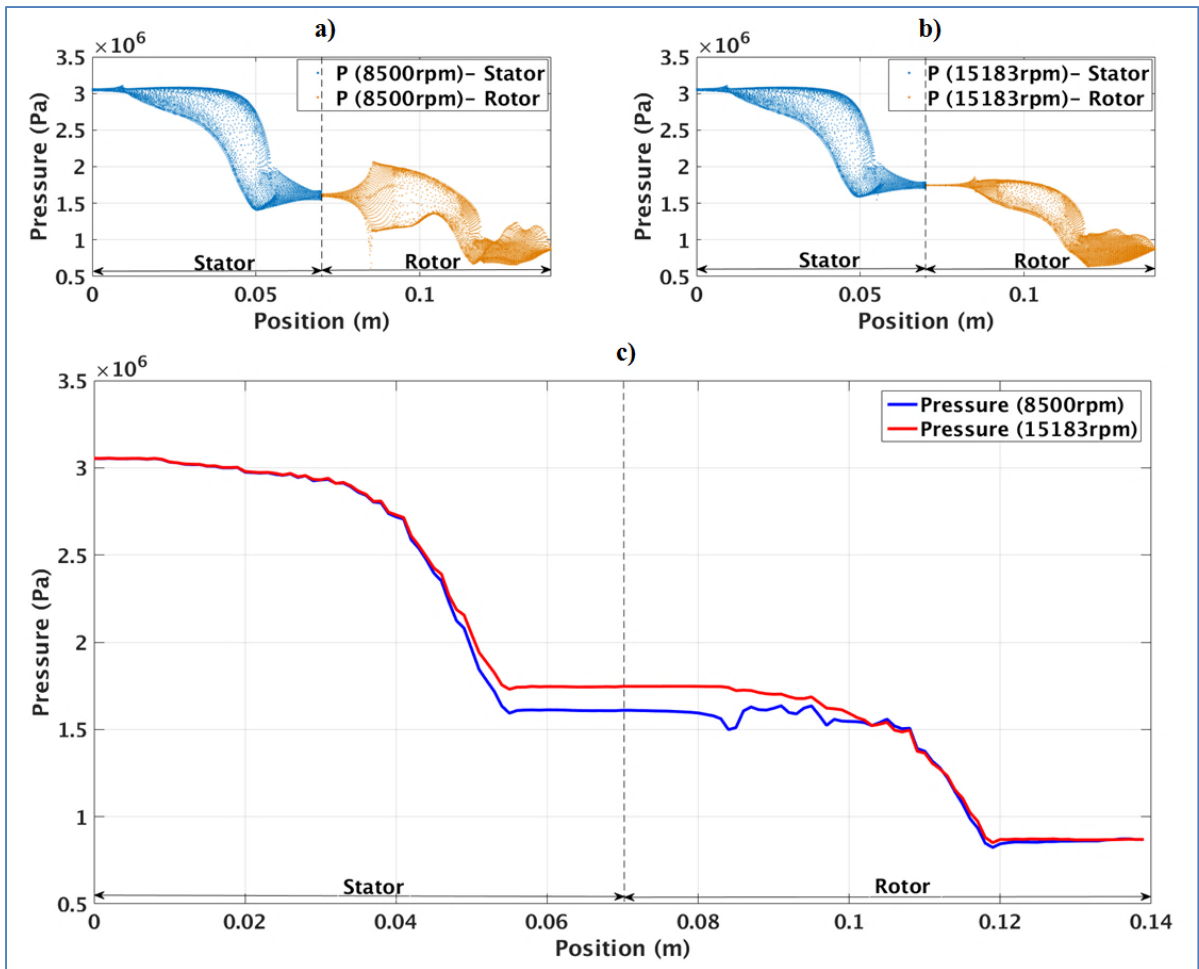


Figure 4.9 Pressure distributions (a, b) and pressure variations (c) in two cases of rotor speed: 8500 rpm and maximum 15183 rpm

(Fig.4.10c). This figure shows that the difference of velocities begins to be appeared behind stator blade TE and at the turbine outlet with a maximum value about 31.2 %. The mechanism of action of rotor speed on the velocity is complex and it can be explained in two pathways: firstly, the increase of rotor speed raised the relative velocity and then increased the absolute velocity while the axial velocity was almost constant in the rotor; secondly, this increase of rotor speed raised vortex in the rotor causing increase of losses around rotor blade and then led to the decrease of absolute velocity in the rotor. Therefore, the velocity value in the case of maximum rotor speed was not always higher than that in operating cruise as shown in Fig.4.10c.

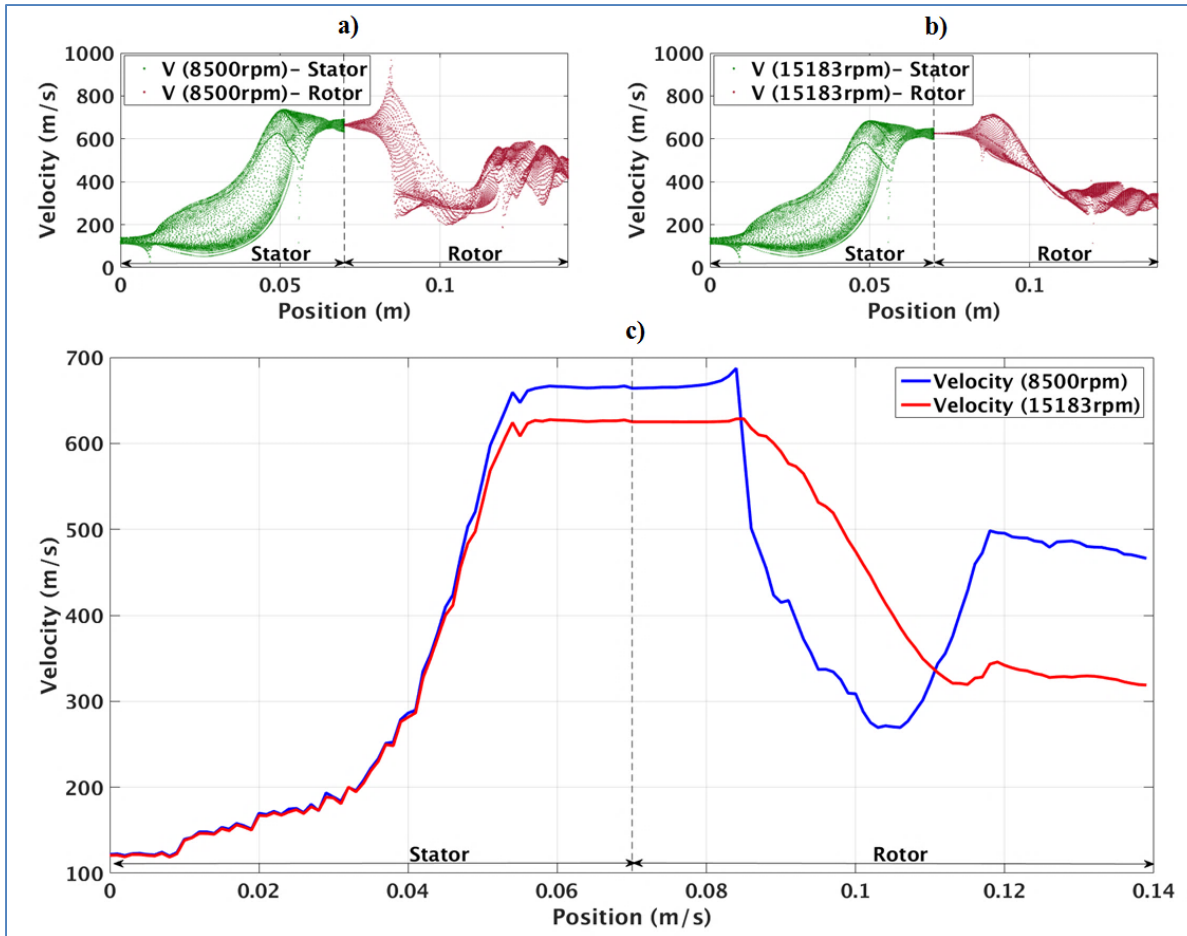


Figure 4.10 Velocity distributions (a, b) and velocity variations (c) in two cases of rotor speed: 8500 rpm and maximum 15183 rpm

Consequently, the rotor speed have direct link to kinetic energy of rotor blade and influenced strongly on the kinetic energy of flow and on the velocity field. However, the kinetic energy of rotor blade has a weak influence on the static enthalpy and pressure. That can be explained by the fact that the transfer of static enthalpy into kinetic energy of flow occurred almost in one direction (these in section 4.2). In the reverse direction, the transfer of kinetic energy to static enthalpy was quite small and in consequence, the effect of the rotor speed on temperature and pressure is trivial.

4.3.3 Effect of cooling at rotor blade

The cooling at rotor blade is necessary to have high performance in internal engine and to protect the rotor blade material. The cooling temperature in rotor blade depends on engine types and rotor blade materials [112, 116]. We report here, the obtained results of the simulated internal cooling in three cases, 1) an adiabatic blade boundary condition, 2) the wall temperature set at 870 K corresponding to blade material by Titanium- based alloys, 3) the wall set at 990 K corresponding to the blade material by Nickel- based alloys.

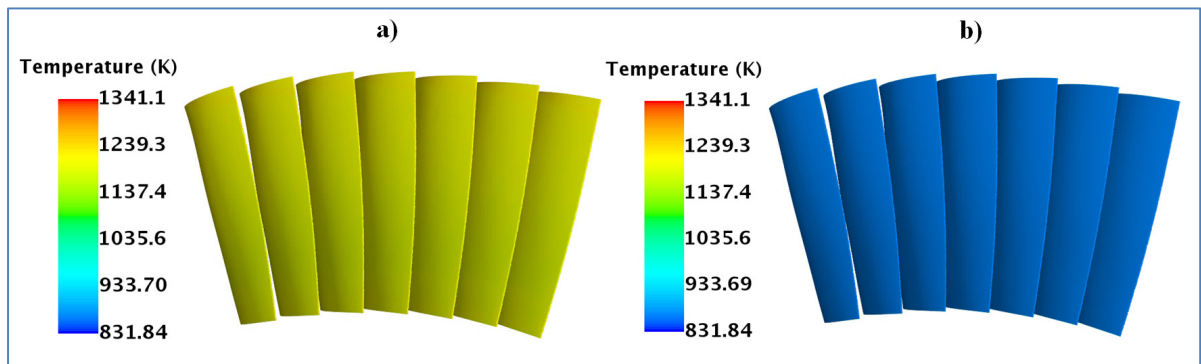


Figure 4.11 Temperature of rotor blade surfaces in two cases: no cooling (a) and cooling (b) at 870 K

Fig.4.11 shows the temperature of rotor blade surfaces in two cases without and with cooling at 870 K. Such described above, the blade surface temperature without cooling was too high and can reached around 1200 K. In this work, to protect the blade material, the cooling at 870 K was used and the blade surface temperature fell to 870 K.

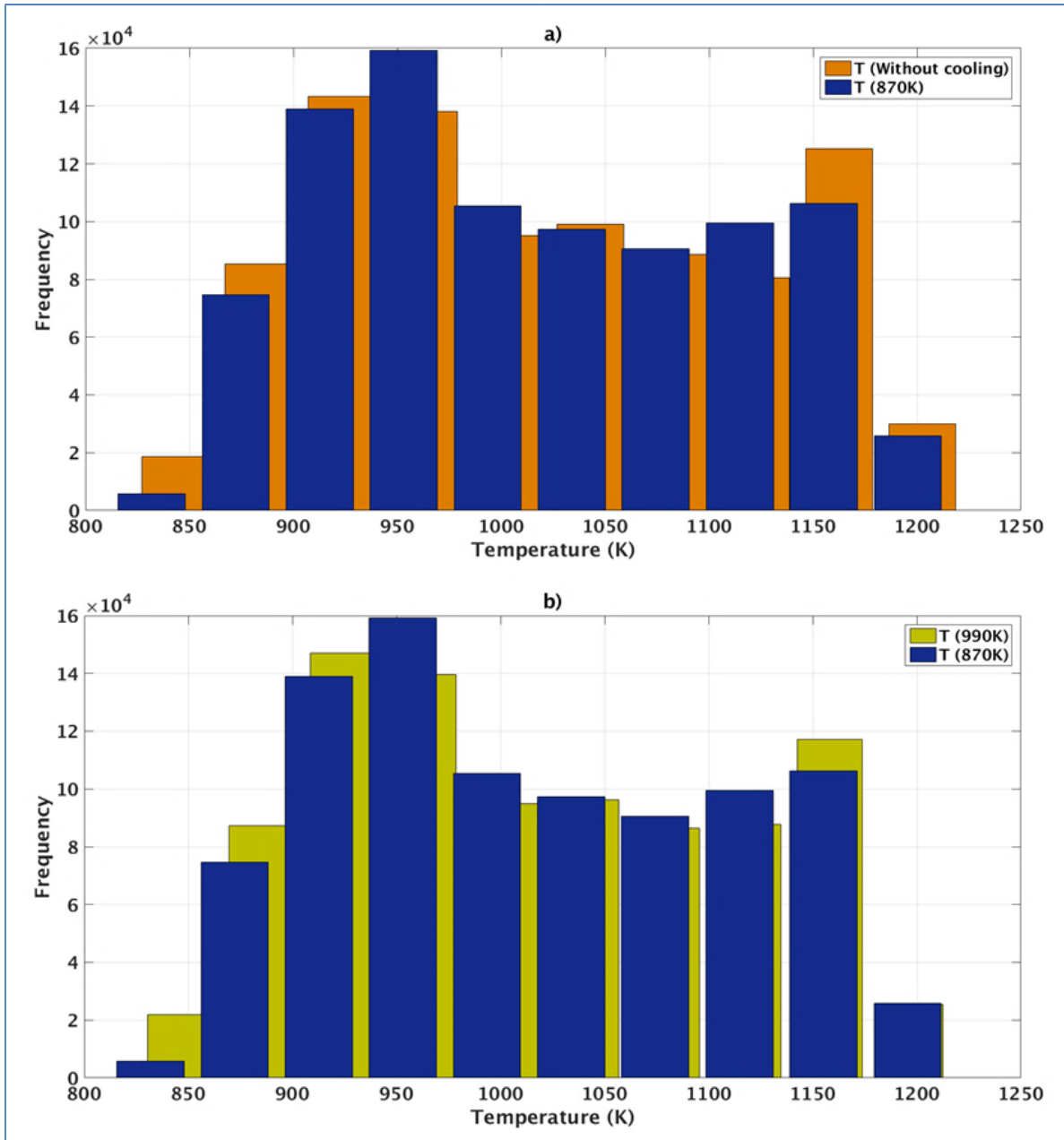


Figure 4.12 Cooling effect on temperature field

Fig.4.12 presents the frequency of temperature values in the HPT in these cases. Fig.4.12.a shows that with cooling, the zone of high temperature above 1150 K was reduced and the zone of lower temperature value around 900 K was increased. Fig.4.12b shows the same tendency meaning that a decrease of the temperature in high temperature area is observed this

occurred at the same time with the increase of lower temperature zone in the both of cases (870 K and 900 K). Thus, the cooling system leads to decrease of the static enthalpy around rotor blade and then causes a decrease of the total static enthalpy in the HPT. The low temperature area around rotor blade was maintained and created (called “film cooling”) to protect rotor blade material. In more detail about the effect of cooling on the flow can be seen in Fig.4.13 and Fig.4.14 showing the variation of temperature and pressure without and with cooling at 870 K. It is found that the difference of temperature value in two cases principally appeared at rotor blade leading edge and then extended to the turbine outlet because the cooling system operating is only for rotor blade. The maximum difference of temperature between two cases was about 1.7 % at the middle of rotor blade and this value was about 0.7 % at the HPT outlet. Fig.4.14 shows that the distributions of pressure in two cases were very similar and have a good agreement with that reported in a recent publication [6]. It has to be noted that the difference of velocity value in these two cases was negligible. In other words, the cooling seems have most effect on temperature field than on pressure and velocity.

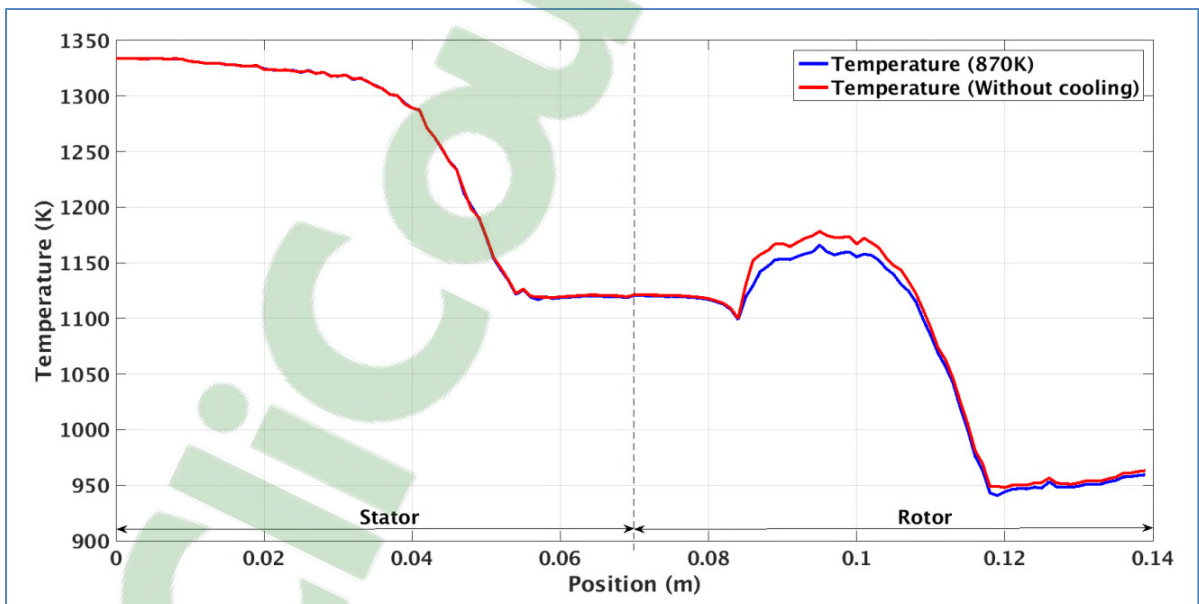


Figure 4.13 Temperature variations as a function of the axial distance in two cases: cooling with rotor blade temperature at 870 K and without cooling

Let us go back to detail about the effects of cooling system on the temperature field. This phenomenon depends on difference between the rotor surface temperature and the temperature of the hot gas stream of flow. The previous studies [117-119] and experiments reported by Leach et al. [112], demonstrated that the cooling effectiveness was defined by:

$$\eta = \frac{T_g - T_m}{T_g - T_c} \quad (4.4)$$

where, T_g the temperature of the hot gas stream, T_m the temperature of rotor blade surface (temperature of the metal) and T_c the temperature of the cooling air. Thus, see Eq. 4.4, while the temperature of the hot gas stream (T_g) only depends on the type of engine and the operating conditions, the cooling system can be influenced by the temperature and material of rotor blade (relation of T_m and T_c).

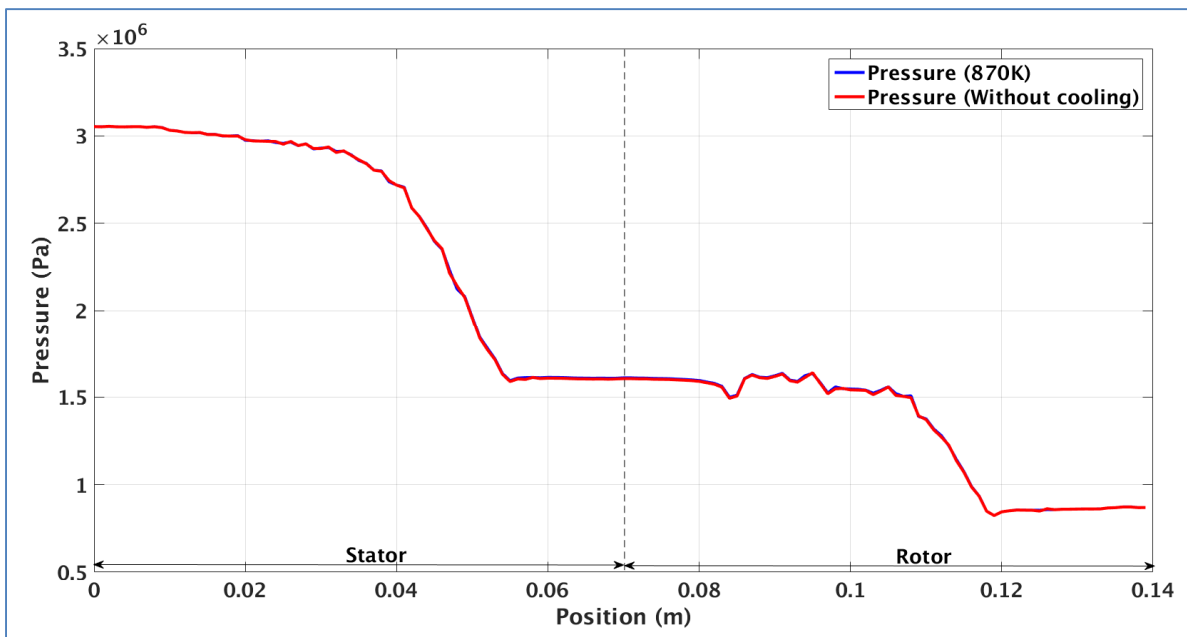


Figure 4.14 Pressure variations as a function of the axial distance in two cases: cooling with rotor blade temperature at 870 K and without cooling

In comparison with the change of initial temperature in section 4.3.1, in both cases: the changes of initial temperature and cooling have the same behavior with global temperature evolution. However, the impact of the initial temperature factor seems bigger than cooling process. Nevertheless, the cooling system has a strict relation with initial temperature in the turbine: basing on the cooling system, the initial temperature can be increased for increase of engine performance and for different operating conditions.

Table 4.1 resumes the maximum different values of the flow parameters and the difference of these parameters at the turbine outlet which are calculated in the previous sections: 4.3.1, 4.3.2 and 4.3.3.

Table 4.1 Effects of initial temperature change, of rotor speed change and cooling system

Parameters	Di_{Tmax}	$Di_{T-outlet}$	Di_{pmax}	$Di_{p-outlet}$	Di_{vmax}	$Di_{v-outlet}$
Initial temperature (1341 K – 1554.5 K)	14.2 %	13.4 %	3.2 %	0.3 %	11.5 %	11.5 %
Rotor speed change (8500 rpm – 15183 rpm)	4.3 %	1 %	22.6 %	0.4 %	31.2 %	31.2 %
Cooling system (870 K – no cooling)	1.7 %	0.7 %	0.4	0.3 %	1.1 %	1.1%

In the HPT, study the temperature field is an important work to better understand the turbine operating conditions and chemical reactions in the internal engine because the temperature is a major factor that can effect the chemical transformation processes. However, the distribution of thermal field is complex and non-uniform under effect of 3D geometry profile. The non- uniformities of thermal field in the turbine will be presented in the next paragraph.

4.3.4 Non-uniformities of thermal field distribution in the spatial HPT

Fig.4.15 presents the distribution of thermal field based on isothermal values for four typical zones: 1341.1 K- 1200 K (a), 1200 K- 1100 K (b), 1100 K- 1000 K (c) and 843.13 K- 1000 K (d). To clearly show the temperature value, each zone herein is presented with 8 different isothermal values. It is considered that the temperature was decreased throughout the turbine (Fig.4.15a-d) that was explained by the losses such as in the section 4.2; the temperature around rotor blade was high from 1050 K to 1250 K as mentioned above (section 4.3.3). Besides, the distribution of thermal field in the turbine was not uniform. The non-uniformities of temperature are observed in the stator and especially in the rotor in both axial and radial directions. The non-uniformities of temperature in the axial direction lead to a decrease of temperature (section 4.2) and the non-uniformities in the radial direction were directly linked to the wakes from stator, moving rotor blade and non-uniform inlet temperature or inlet temperature distortion at rotor inlet. In this research, we calculate and simulate the thermal field in both parts of the turbine (stator and rotor). These calculations were much more complex than that realized only for one row of stator or rotor. The temperature at rotor inlet was directly linked to stator outlet temperature results via “mixing plane” and was a non-uniform inlet temperature.

Fig.4.15a-b show that the maximum surface temperature on the pressure side was higher than the average gas temperature at the suction side. This phenomenon has been already explained by Butler et al. [120] and Kerrebrock et al [121] upon the tendency for separation of hot and cold gases in the turbine rotor. Thus, to protect the rotor blade, we concentrated especially on the material of pressure side of rotor blade. Fig.4.15 allows to be perceived that the distribution of isothermal values were complex. Nevertheless, basing on the previous studies [120-122], we can predict lines of isothermal values along the rotor pressure surface following:

$$\frac{d^2 \delta}{d^2 z} = \frac{1}{R} \left(\frac{T_{iso}}{T_0} - 1 \right) \frac{(\Omega R)^2}{W_z^2(z)} = \frac{1}{R} \left(\frac{T_{iso}}{T_0} - 1 \right) \frac{1}{\phi^2} \quad (4.5)$$

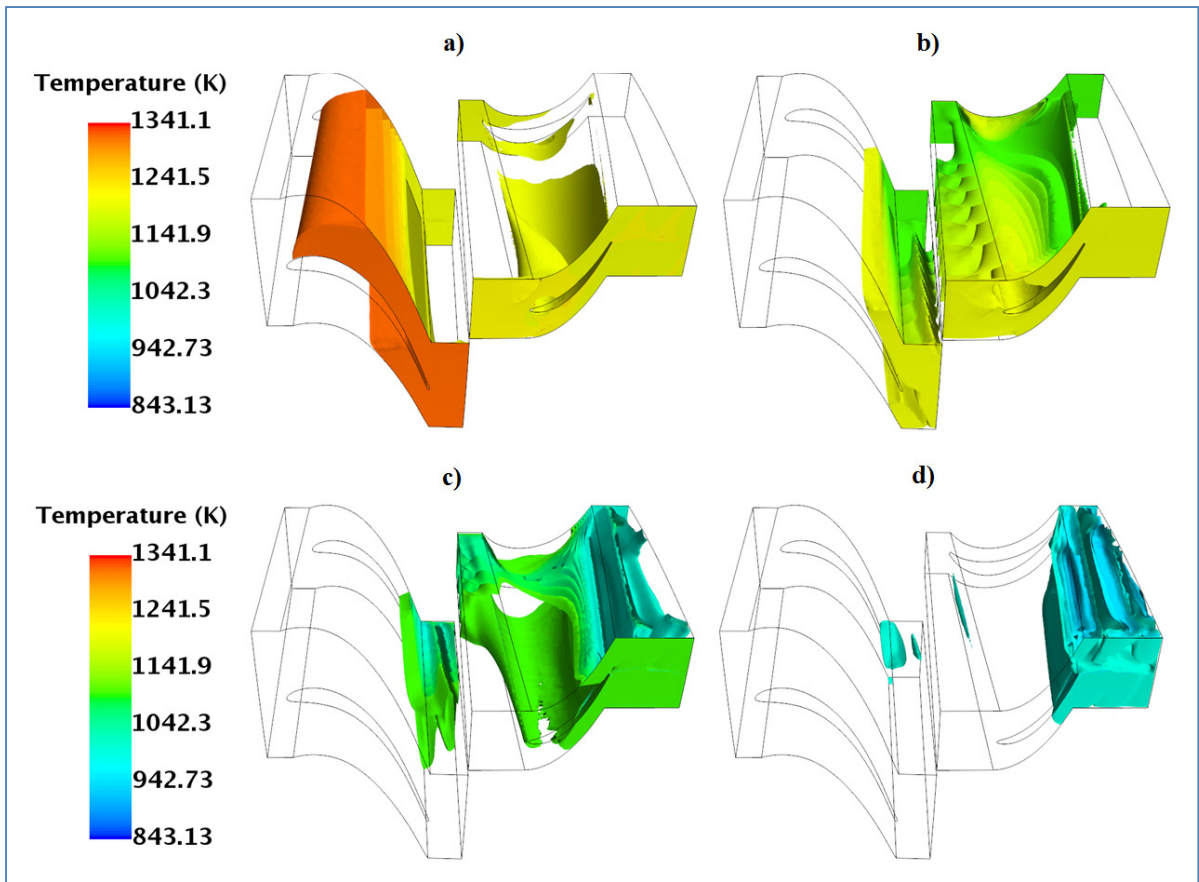


Figure 4.15 Isovalues of thermic field in the turbine following four zones: 1341.1 K- 1200 K (a), 1200 K- 1100 K (b), 1100 K- 1000 K (c) and 843.13 K- 1000 K (d)

where, δ the radial displacement of isothermal values in comparison with mean surface streamline [122] (as shown in Fig.4.16), z the axial axe or the rotational axe, R the radius, T_{iso} the isothermal value, T_0 the fluid static temperature, Ω the rotational speed, W_z the axial velocity on the blade pressure surface and $\phi = \frac{W_z}{\Omega R}$ the familiar nondimensional flow coefficient. As shown in Eq. 4.5, it is considered that the displacement scaled linearly with streak temperature and at the low flow coefficient, there was more influence on the radial displacement versus the high flow coefficient. Therefore, the distribution of isothermal values in rotor was as a function of many variables: radius, streak temperature, rotor speed and the axial velocity.

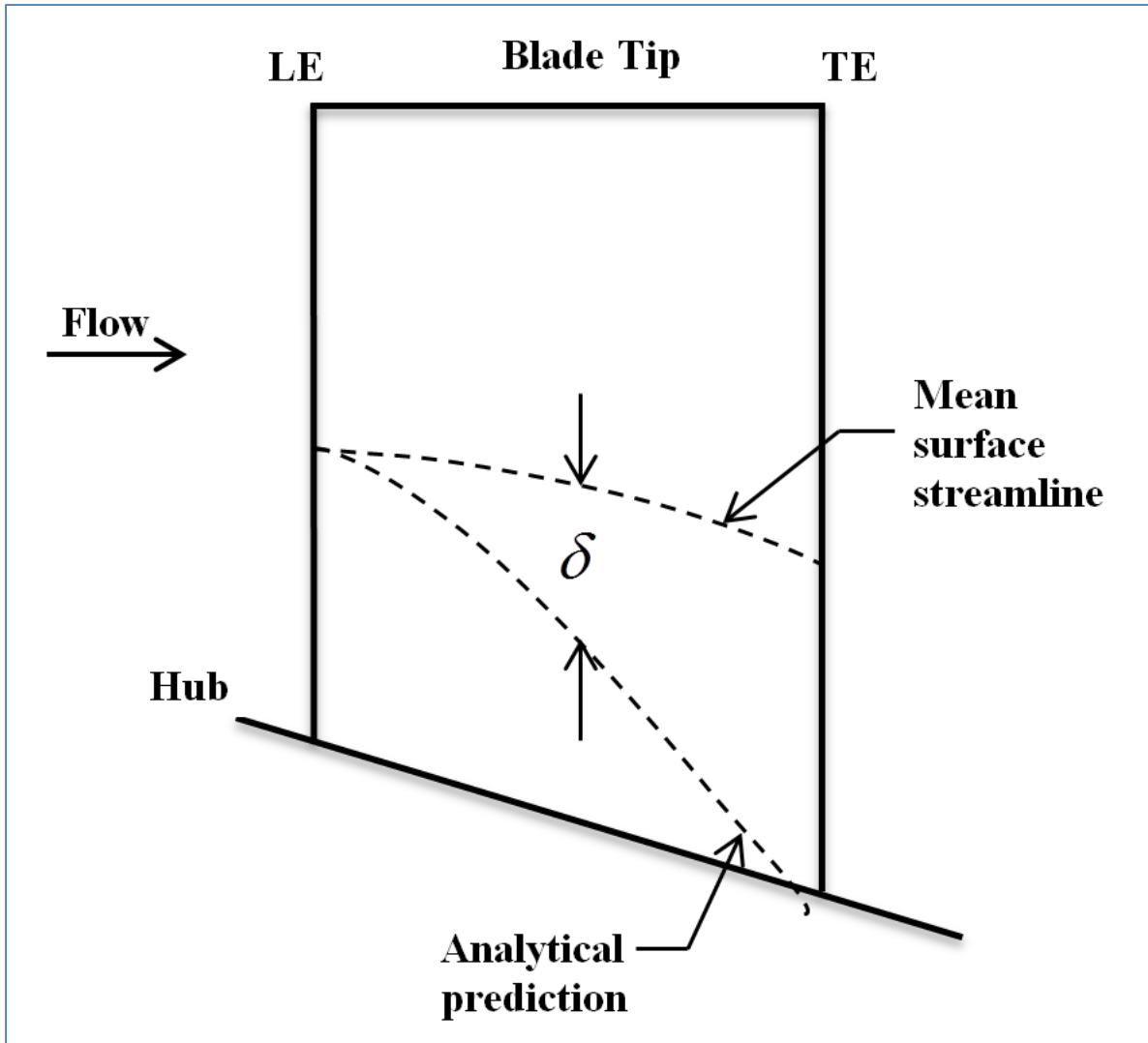


Figure 4.16 Simple model predicted (Eq. 4.5) of temperature isovalue line along the rotor pressure surface

More detail about the non-uniformities of thermal field can be seen in Fig.4.15 in which the temperature decreases about 28.2 % from 1341 K at the HPT inlet to 963 K at the HPT outlet ($T_{outlet} / T_{inlet} = 0.72$) in the axial direction; in the radial direction, the temperature increases from 1050 K at the hub surface to 1200 K at the tip surface, the maximum difference in these two surfaces was calculated at about 12.5 % and $T_{tip} / T_{hub} = 1.14$.

4.4 Conclusion

3D design of the HPT, tridimensional computed calculations and modeling on the aerothermodynamic evolution, the influence of operational parameters on the aerothermodynamic process and the non-uniformities of thermic field in the HPT have been investigated.

The thermal boundary condition strongly affected the flow temperature with the maximum difference of temperature between take-off and cruise processes about 14.2 % while the rotor speed has a significant effect on the flow velocity. Additionally, the effect of cooling system was quite small. This factor has a slight impact on the temperature around rotor blade surface with a value of about 1.7 %. The work highlights also the non-uniformities of temperature in the turbine in axial and radial directions. The obtained results show a difference of temperature about 28.2 % between the HPT outlet and inlet in the axial direction and in the radial direction this value in the hub surface and tip surface can be lower (12.5 %).

This paper is a continuation and extension of earlier works that the author and the co-workers realized to study the interactions of aero-thermodynamic and chemical processes in the HPT. This paper brings the useful information and new insights to better understand the aerothermodynamic process and the operating conditions of high pressure turbine. The results issued from this work can be used for various aircraft engines and helps to optimize the design of compressor and turbine for the next generation of aircraft engines.

Clicours.COM

CHAPTER 5

3-D MODELING OF TRANSFORMATION OF AEROSOL POLLUTANTS IN THE HIGH PRESSURE TURBINE

Trung Hieu Nguyen^a, Tri Phuong Nguyen^b, Francois Garnier^a

^a TFT Laboratory, Ecole de Technologie Superieure (ETS), 1100 Notre-Dame St W,
Montreal, Quebec, Canada H3C 1K3

^b Department of Chemistry, University of Montreal (UdeM), 2900, Édouard-
Montpetit Boul., Montreal, Quebec, Canada H3C 3J7

This chapter has been submitted for the publication in the “*Chinese Journal of Aeronautics*”
– Elsevier Publications, September 2017

5.1 Introduction

Aviation is a direct source of gas phase pollutants through its emissions such as greenhouse gases (CO₂, water vapor), sulfur and nitrogen oxides (SO_x, NO_x). That contributes to environmental pollutants and local air quality around airports [2]. To evaluate the impact of aviation on global climate in the atmosphere and air quality near airports, one needs to understand the formation mechanisms of these key chemical compounds inside aircraft engine (combustor, turbine and exhaust nozzle). In the past, the chemical process in the combustor was studied by many researchers such as Dhatchanamoorthy et al. [106], Mark et al. [107], Leżański et al.[108] and recent researches [5, 13, 14] also showed that the change of chemical species in the nozzle is very small. However, the studies on the turbine are very scarce because of the complexity of the flow and processes in this part. Nevertheless, the evolution of the processes in the turbine is needed to study. There are two principal processes in the turbine: aero-thermodynamic and chemical process. This paper is to study the chemical process with the formation and transformation of aerosol pollutants in the turbine. This research is a continuation and extension of earlier works that the author and the co-workers realized to study the aero-thermodynamic processes in the high pressure turbine.

The investigation of precursor pollutants in the HPT is challenging because of the complexity of kinetic chemistry in the 3-D complex flow relating moving blade at high temperature and

pressure. In the past, Moniruzzaman et al. [12] and Bisson et al. [13] used 0-D and 0-D/1-D simulations to study the chemical process in the HPT. The authors simulated the transformation of species in both the combustor and post-combustor (turbine and nozzle) by using the CHEMKIN package. However, the HPT was simplified and replaced by a reactor. Since the authors used 0-D and 1-D simulations, the effects of turbine geometry, blade profiles and rotation speed was not taken into account.

Starik et al. [4] realized modeling of sulfur and chemiions in aircraft engines with a quasi-one-dimensional (Q1-D) model. This is the first published model study of ion formation in the intra-engine of an aircraft engine. Nevertheless, most of the rate constants for ion chemistry were determined at low temperature ranges (300 K - 500 K), which are significantly different from the real operating temperatures of high pressure turbine (HPT) (above 1000 K); and because of using Q1-D modeling there had the limits such as the above discussions.

One-dimensional (1-D) and two-dimensional (2-D) numerical simulations have been proposed by Lukachko and co-workers [6], in which the chemical reactions were carried out at the high temperature (above 1000 K) and high pressure that are very close to the operating condition of HPT. In this research, the authors used a developed computational tool of chemistry (CNEWT) to simulate production of sulfate aerosol pollutants in the post-combustor intra-engine (turbine and exhaust nozzle) of an aircraft engine. However, the calculations for the turbine were only performed over a single blade row, the multi-rows of turbine relating the moving blade and 3-D effects on the chemical formation of species has not been performed.

The research introduced in this paper focuses on the roles of fluid dynamic and chemical kinetic processes in setting of the transformation of aerosol precursor emissions of precursor pollutants (NO_x , SO_x) and other gas species (hydrogen, oxygen species and carbon oxides) in the turbine before that are emitted into the nozzle and the atmosphere. The new insights of dissimilarities of chemical transformations in the 3-D multi-rows HPT and the effects of moving rotor blade on this process are also taken into account. In comparison of three calculations (1-D, 2-D and 3-D), the limits and the underpredictions 1-D and 2-D simulations

are shown. In this research, the turbulence modeling strategy RANS in a complex packaging of STAR-CCM+ is used that is capable of 3-D modeling and simulation. The results are executed and analyzed with an in-house Matlab routine, and compared with that reported in the literature.

5.2 Evolution of N-, S-, O-, H- and C-containing gas species in the HPT

This section discusses the transformation of aerosol pollutants and inadequacies of 1-D and 2-D simulations. In more detail, this section concentrates the evolution of N-, S-, O-, H- and C-containing gas species under the effects of flow nonuniformities in the turbine. This section shows not only the tendency of gas transformation in 1-D but also the distribution of mole fractions around turbine blades in 2-D at the 50 % span.

5.2.1 Evolution of nitrogen species

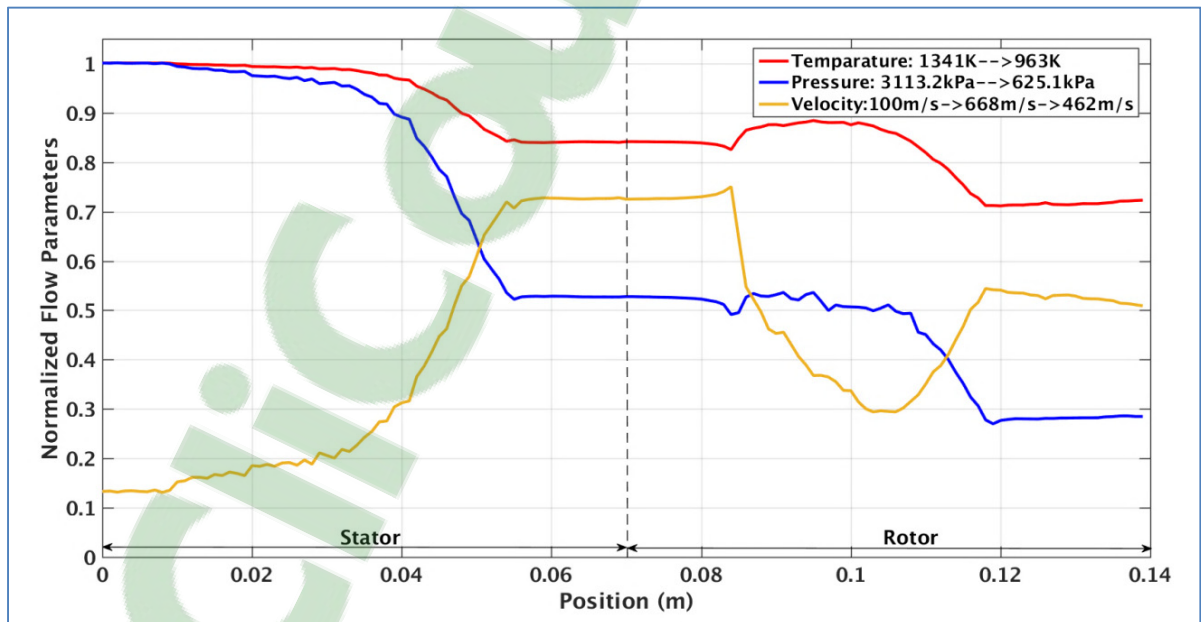


Figure 5.1 Temperature, pressure and velocity evolution from the combustor exit to the HPT exit

A base line of temperature, pressure and velocity was conducted and established using the method described in the section 3.2.1 as shown in Fig.5.1 to better understand the influences of flow parameters on the chemical transformations. However, the aero-thermodynamic process was presented in the other research. This research concentrates the transformation of chemical species.

Fig.5.2 shows the evolution of major nitrogen pollutants (N- containing) at the 50 % span. It is observed that the nonuniformities of nitrogen distribution occur throughout the whole turbine by the effects of turbine blade profiles. Additionally, with the influences of moving rotor blade, the nonuniformities occur strongly in the rotor, especially over rotor blade. In detail, the NO mole fraction decreases from $2.52 \cdot 10^{-3}$ at the turbine inlet to $6.25 \cdot 10^{-4}$ at the turbine outlet (Fig.5.2a) caused by the conversion of NO to NO₂ (also see NO₂ increases from $2.80 \cdot 10^{-4}$ to $7.10 \cdot 10^{-4}$ at the same time in Fig.5.2c). The conversion of NO to NO₂ is the very important process to detect NO_x in the turbine. The conversion of NO to NO₂ is realized via three main pathways: $\text{NO} + \text{O} \leftrightarrow \text{NO}_2$; $\text{NO}_2 + \text{O} \leftrightarrow \text{NO} + \text{O}_2$ and $\text{NO} + \text{HO}_2 \leftrightarrow \text{NO}_2 + \text{OH}$ (other principal pathways via HONO by the reaction $\text{HONO} + \text{OH} \leftrightarrow \text{NO}_2 + \text{H}_2\text{O}$). Although there are four principal pathways leading to NO₂, it is generally believed that the formation of NO₂ was typically dominated via NO and HO₂ by $\text{NO} + \text{HO}_2 \leftrightarrow \text{NO}_2 + \text{OH}$ [5]. To estimate the conversion of NO to NO₂, the ratio $X_{\text{NO}_2} / X_{\text{NO}_x}$ is usually used. Numerical simulation demonstrated that the ratio $X_{\text{NO}_2} / X_{\text{NO}_x}$ increases from 9.6 % at the turbine inlet to 17.8 % at the turbine outlet (as shown in Fig.5.3). The increase of $X_{\text{NO}_2} / X_{\text{NO}_x}$ and the obtained value of this ratio are in good agreement with calculations [12, 14] and measurements [10, 78, 105], in which this ratio was detected in the range of 6 % to 23 % for different aircraft engines.

Fig.5.2b, Fig.5.2g and Fig.5.2h show the increase of N₂O, HNO₃ and HONO in the HPT, respectively. These results are in line with results reported by Morriruzzaman [12] and Wey [10, 78] for CFM- 56 engines. The above discussion, HONO contributes to the NO₂ production via $\text{HONO} + \text{OH} \leftrightarrow \text{NO}_2 + \text{H}_2\text{O}$, but HONO is one of few combustion products in the aircraft engine emission in the turbine and nozzle [12]; in this research,

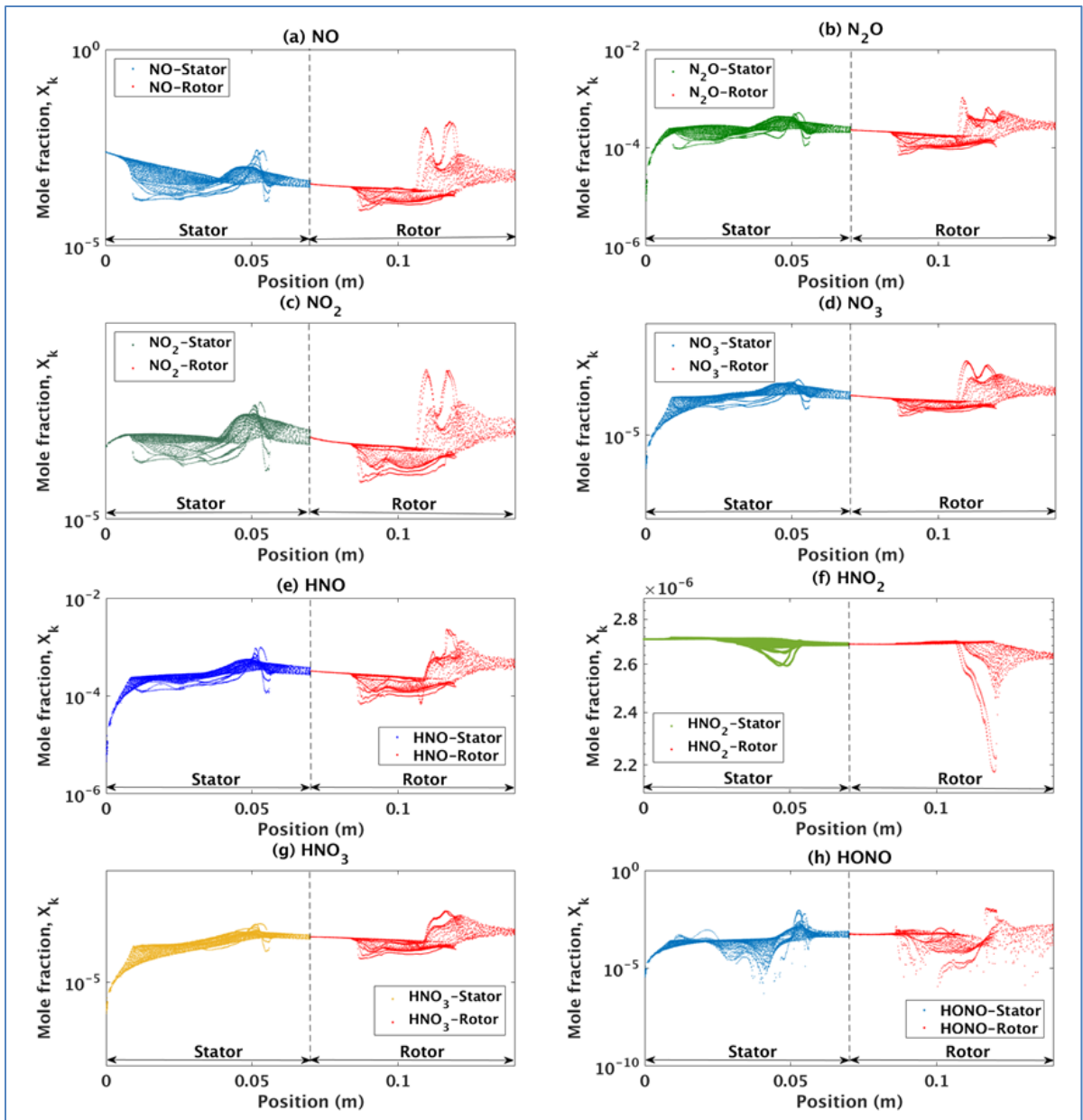


Figure 5.2 N-containing gas species mole fractions (nitric oxides and nitric acids) at the 50% span

HONO is about 2.3 % of NO_x at the turbine outlet (in comparison with 2 % as reported by Lukachko [5]). In summary, the NO_x transformations and tendency of NO_x gradients in the HPT, Fig.5.3 presents the average mole fraction of NO_x species. Thus, the proposed model

can adequately predict both NO_x transformation and the $X_{\text{NO}_2} / X_{\text{NO}_x}$ ratio in the turbine, which is very important for analysis of aviation impact on the atmospheric processes.

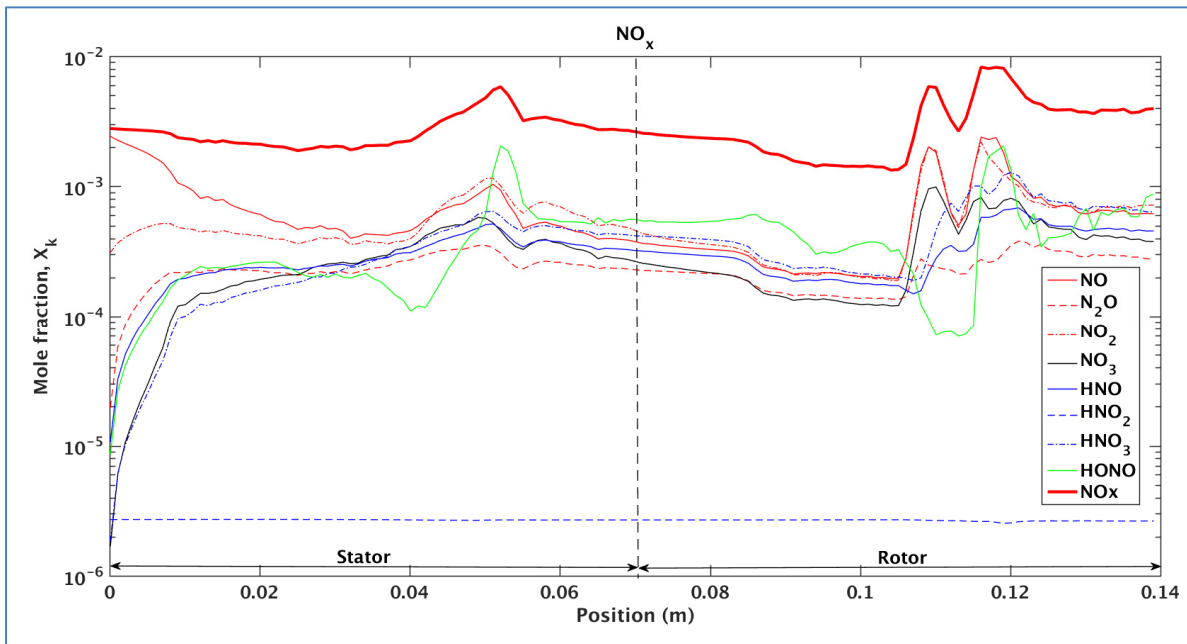


Figure 5.3 Baseline calculation results of $\overline{X}_{\text{NO}_x}$

5.2.2 Evolution of sulfur species

Fig.5.4 and Fig.5.5 exhibit the evolution of principal sulfur species in the HPT. It was observed that the decrease of SO_2 simultaneously occurs with the increase of SO_3 caused by conversion from SO_2 to SO_3 . Similar to NO_x case, this conversion strongly occurs in zones near the combustor exit or the turbine inlet where the temperature and the pressure are very high and possessed more concentrated oxygen [6, 69, 70]. In detail, the mole fraction of SO_2 decreases from $2.05 \cdot 10^{-4}$ at the turbine inlet to $9.19 \cdot 10^{-5}$ at the turbine outlet and the mole fraction of SO_3 increases from $6.42 \cdot 10^{-6}$ to $8.30 \cdot 10^{-5}$. The conversion from SO_2 to SO_3 is realized via two principal pathways: at the high pressure before stator blade's leadings where the fractional conversion of NO to NO_2 increases, SO_3 formation via $\text{SO}_2 + \text{NO}_2 \leftrightarrow \text{SO}_3 + \text{NO}$

becomes important and at the lower pressure, SO_3 formation occurs through $\text{SO}_2 + \text{O}(+ \text{M}) \leftrightarrow \text{SO}_3(+ \text{M})$ [62]. In the both pathways, for SO_3 production, resultant impact of SO_2 is positive. At high pressure near the combustor outlet (or the turbine inlet), addition of NO_2 from NO_x chemistry falls significantly on the effects of SO_2 , reduces SO_2 and favors the SO_3 formation [68].

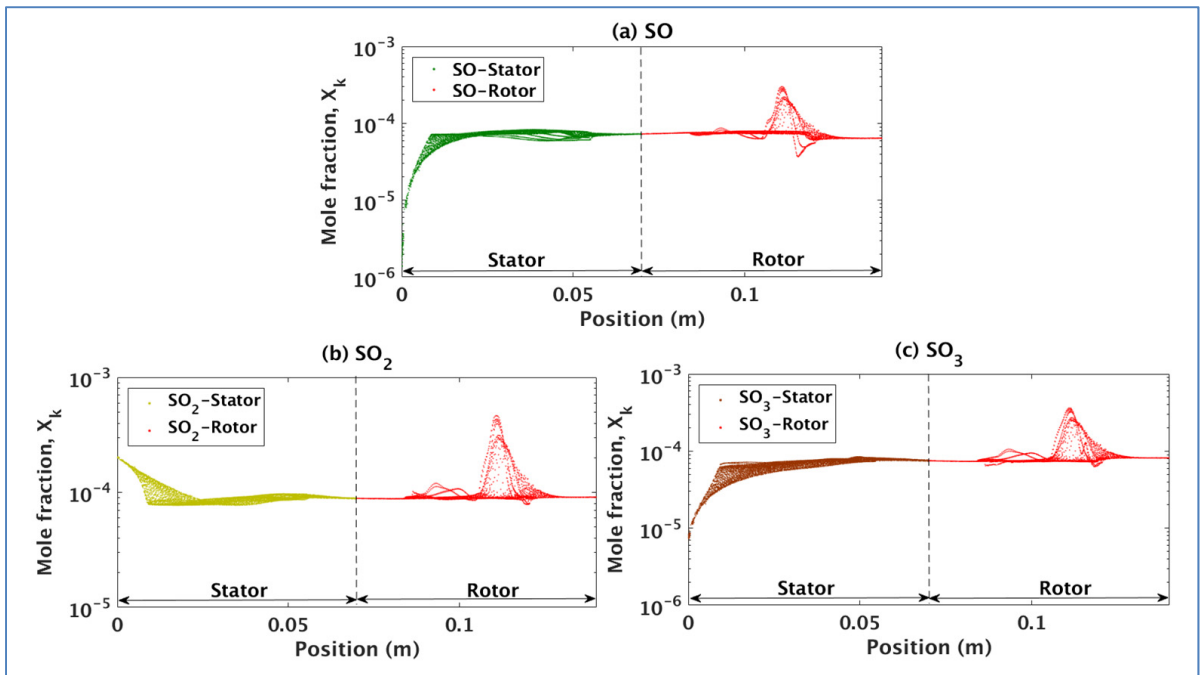


Figure 5.4 S-containing oxide gas species mole fractions ((a), (b) and (c)) at the 50% span

The changes of S-containing in the HPT are in line with the numerical results [4-6, 12-14] and the experimental results of Mueller [62] and Glarborg [68]. The important parameter, which characterizes the efficiency of conversion of SO_2 to SO_3 ($X_{\text{SO}_3} / X_{\text{SO}_2}$) [5] changed from 3.03 % at the combustor exit to 33.2 % at the turbine outlet (Fig.5.8 and Table 3.1). In comparison with 1D results of Lukachko [6], this ratio change is in the range of 3.0 %- ~53.3 %. This difference can be explained by 3D geometry effects combined with rotor rotation effects in this study that will be represented in detail in section 5.3.

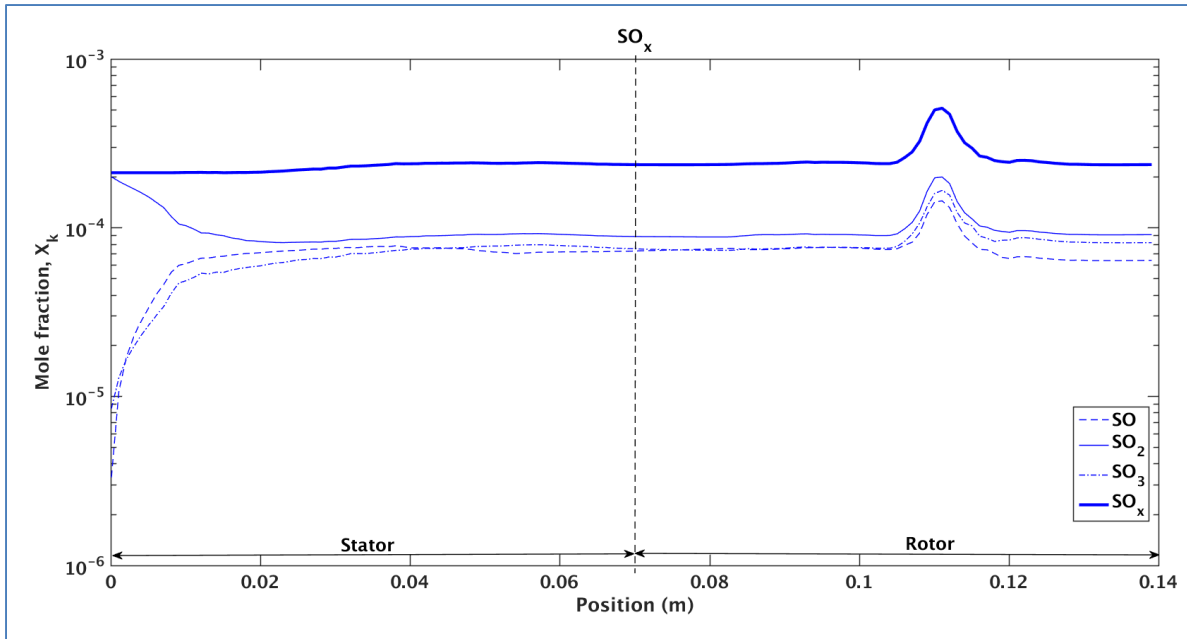
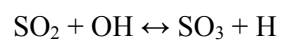


Figure 5.5 Baseline calculation results of \overline{X}_{SO_x}

5.2.3 Evolution of hydrogen, oxygen species and carbon oxides

Fig.5.6 shows the evolution of hydrogen, oxygen and carbon oxides at the 50 % span in the HPT. It is found that the change of mole fractions of species occur strongly at the zone near the combustor outlet or the HPT inlet at the high temperature and the high pressure that correspond with the formation of NO_x and SO_x at this zone. Then the change of mole fractions of these species occurs more slowly in the next regions behind the stator LE.

The recent researches [5, 14] showed that the OH radical is the main oxidizer both in the combustor and the postcombustor flow such as the HPT. The Fig.5.6e exhibits that the OH concentration decreases in the HPT that is due to the occurrence of the principal following processes:



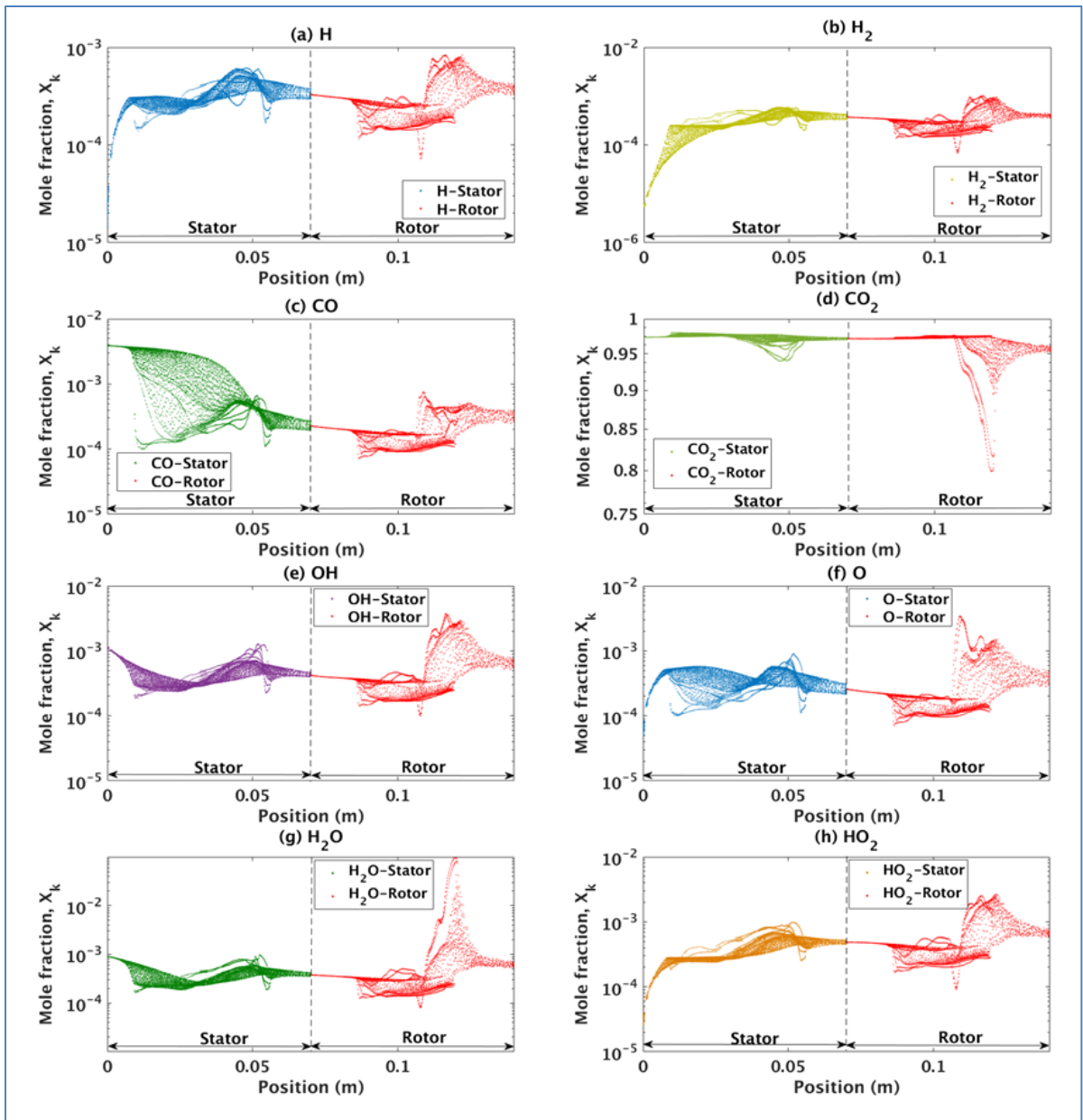


Figure 5.6 O-, H- and C-containing gas species mole fractions at the 50% span

Such as the above discussion about the formation of SO_x and the conversion of SO_2 to SO_3 , at the lower pressure behind the stator LE, SO_3 formation occurs through $\text{SO}_2 + \text{O} (+ \text{M}) \leftrightarrow \text{SO}_3 (+ \text{M})$. That may cause the decrease of O behind the stator LE (Fig.5.6f). Fig.5.6f shows also the increase of O near the combustor outlet or the HPT inlet. That is unpredicted,

Lukacho et al [6] also exhibited the unpredicted increase of O near the combustor outlet, that may be caused by the conception of the HPT in the engine.

Fig.5.6d shows the evolution of an important greenhouse gas (CO_2), the CO_2 is quite stable in the HPT and its mole fraction has a little bit of change behind the rotor TE causing by the trailing edge vortex. Fig.5.6d reconfirm that CO_2 possesses the high percentage of gases in the HPT.

Fig.5.7 presents the gradient of CO, OH, H_2O , H_2 , N_2 evolution. Therefore, besides CO_2 , the N_2 has also the high percentage in comparison with the mole fraction of no pollutants (hydrogen, oxygen and carbon oxides).

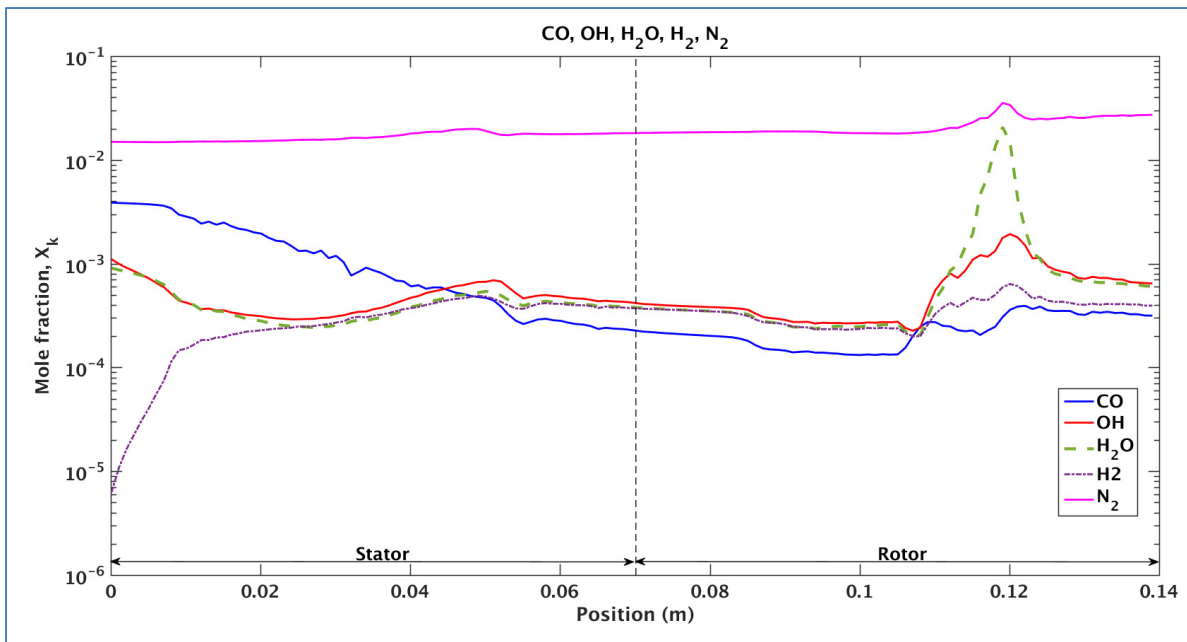


Figure 5.7 Baseline calculation results of $\overline{X_{\text{CO}}}$, $\overline{X_{\text{OH}}}$, $\overline{X_{\text{H}_2\text{O}}}$, $\overline{X_{\text{H}_2}}$ and $\overline{X_{\text{N}_2}}$

In summary, the Fig.5.8 exhibits the generalized trends of gas species in the HPT. It is considered the stability of the primary exhaust products (CO_2 , H_2O and N_2), the light decrease of the secondary exhaust species (NO , SO_2) caused by the conversion of NO and SO_2 to NO_2 and SO_3 , the increase of oxidation species such as HNO_3 and SO_3 and the

decrease of OH oxidant participating in the chemical reactions to the formation of NO_x and SO_x . Additionally, Table 3.1 presents the averaged mole fractions of species at the HPT inlet and HPT outlet.

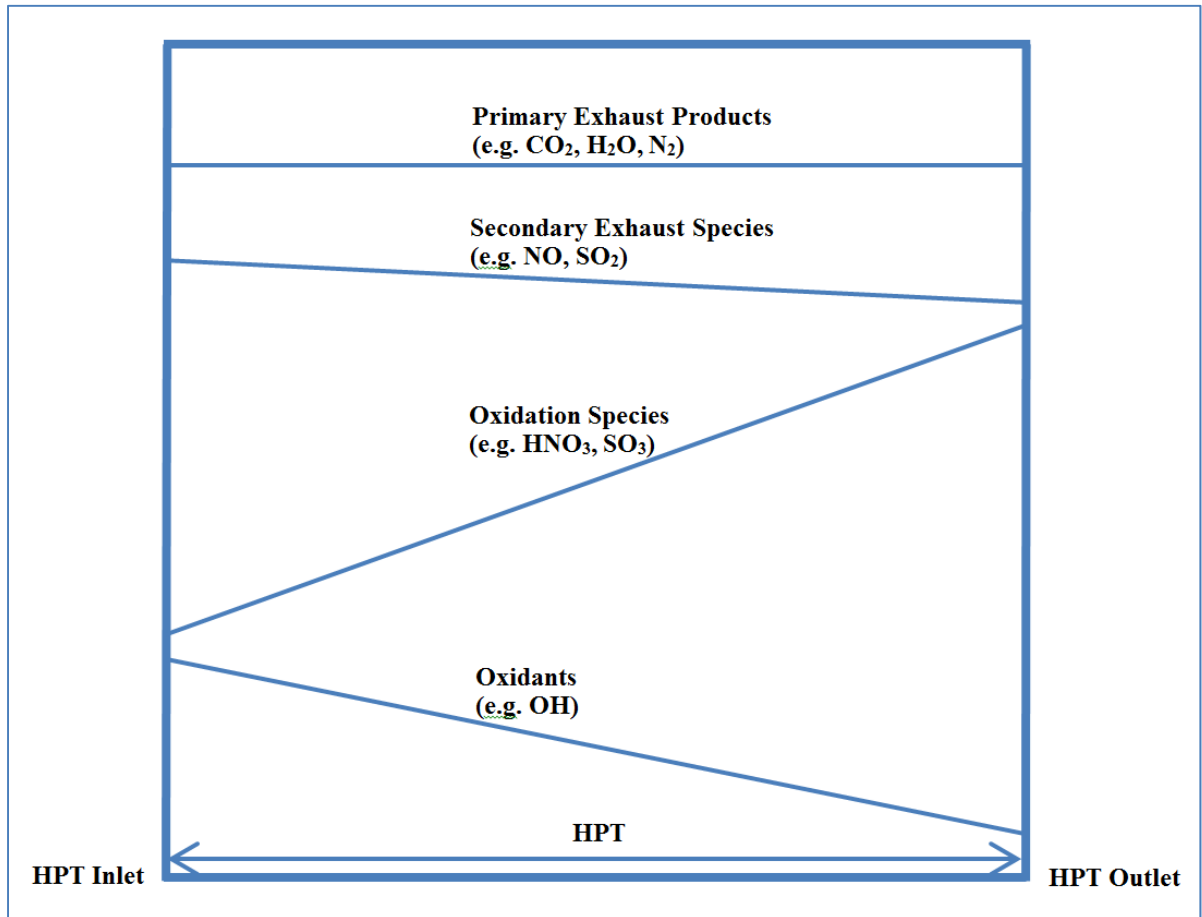


Figure 5.8 Generalized trends of gas species in the HPT

5.3 Inadequacies of 1-D, 2-D and 3-D analyses on chemical change

The results presented in this section discuss nonuniformities of gas distribution in 3-D turbine, especially in three typical surfaces at the 5 %, 50 % and 95 % spans. In the comparison of 1-D, 2-D and 3-D simulations, this section shows the inadequacies of 1-D and 2-D estimations and the useful information from 3-D solutions. The differences of aerosol

precursor results in the turbine of three types of simulation (1D, 2D, 3D) are investigated in this section.

1-D estimations are based on averaged profiles of 2D profiles of evolutions of species at the 50 % span. Fig.5.9 shows both of 1-D and 2-D solutions for CO₂ mole fraction at the 50 % span. It is considered that the 1-D analysis agrees with the trends of 2-D calculation, but they did not agree with the magnitude of change. With the 2-D calculations, they give more information about the concentration of CO₂ mole fraction at each region along the rotation axe, the influence of 2-D profiles of turbine blades on distribution of CO₂ mole fraction. Fig.5.9 also shows that the big difference between the 1-D and 2-D calculations principally occurs at rotor blade where concentrates the vortex such as the above discussion in the previous sections. Table 5.1 compares the 1-D estimation to the 2-D calculation and shows maximum difference of mole fractions of principal species at the HPT outlet and over rotor blade. It is found that the mole fractions of species at the HPT outlet can be underpredicted by 16.4 %, most of which is due to poor prediction of change in NO. At the HPT outlet, the change of CO₂, H₂O, N₂, SO₂ and SO₃ are captured more accurately than changes in NO, HNO₃ and OH by 1-D calculation. Over the rotor blade where has the big difference between 1-D and 2-D calculations, the difference can be underpredicted by 75.6 % in H₂O. Therefore, the difference of estimated mole fractions of species between 1-D and 2-D solutions is due to the difference of chosen species and of chosen regions that we want to study in the turbine.

In comparison of the 2-D and 3-D calculations, Fig.5.10 shows the distribution of CO₂ mole fraction in three cylindrical surfaces at the 5 %, 50 % and 95 % span. It is revealed that the evolutions of CO₂ in three 2-D surfaces are dissimilar that is due to the different blade profiles, the different influences of source term of rotor speed on the different radical radiuses and the nonuniformities of aerothermodynamic parameters of three surfaces. Quantitatively, Fig.5.11 presents averaged 2-D calculation of CO₂ mole fraction in the three surfaces. It is considered that the trends of CO₂ evolution are the same but the magnitudes of CO₂ mole fraction are different, particularly in the rotor. Fig.5.12- 5.16 show the evolution of mole fractions of other principal species in the HPT (NO, HNO₃, SO₂, SO₃ and OH) at the 5 %, 50 % and 95 % span. The difference of mole fractions in three 2-D surfaces is different

for each gas in the turbine. If three curves at 5%, 50 % and 95 % span is quite converged for SO_2 and SO_3 (Fig.5.14, 5.15), they are diverged for CO_2 , NO , HNO_3 and OH (Fig.5.11, 5.12, 5.13, 5.16), especially behind the rotor trailing edge caused by the rotor trailing edge vortex.

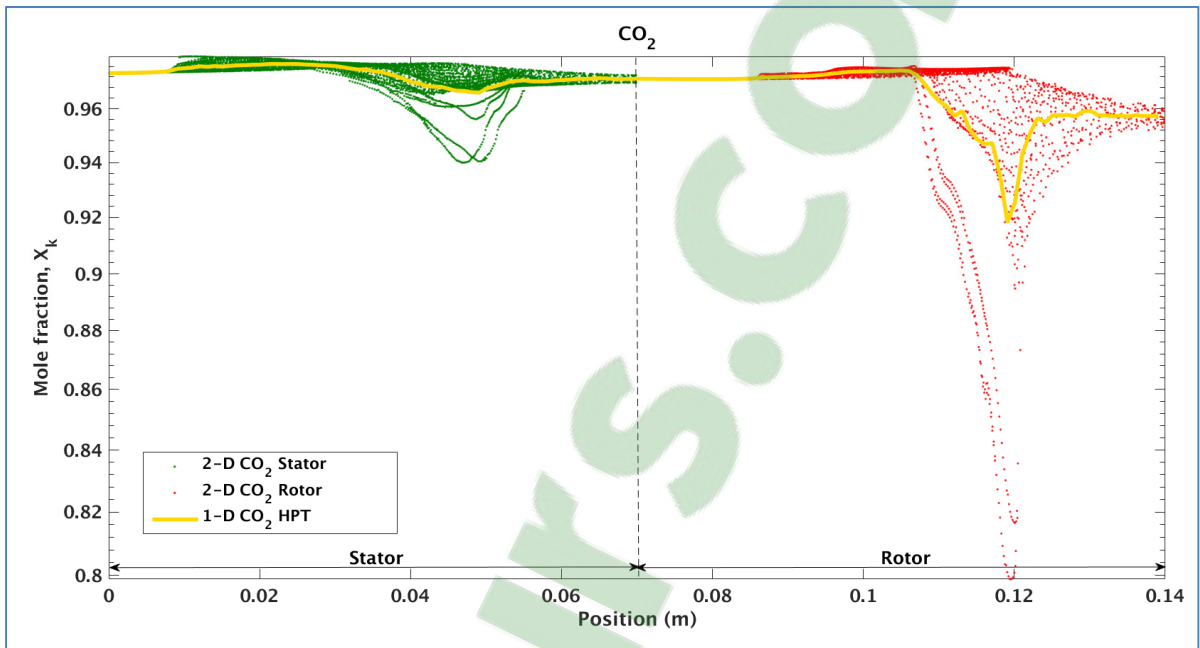


Figure 5.9 X_{CO_2} distributions of 1-D estimation and 2-D solutions at the 50 % span

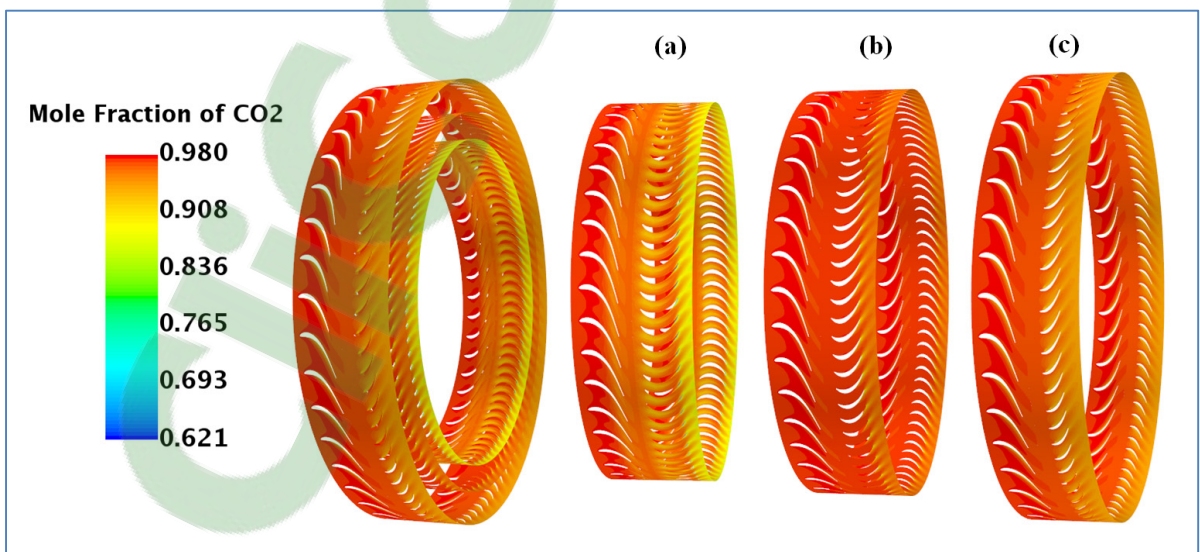


Figure 5.10 X_{CO_2} distributions at the 5 % (a), 50 % (b), and 95 % (c) span

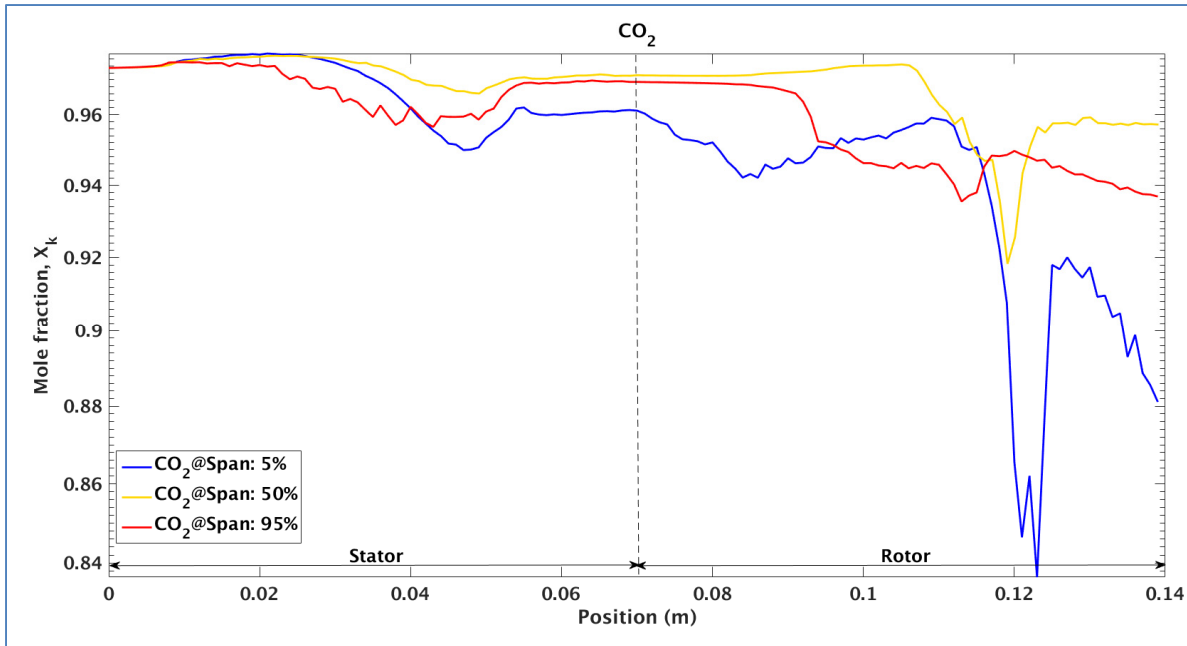


Figure 5.11 CO_2 evolution at the 5 %, 50 %, and 95 % span

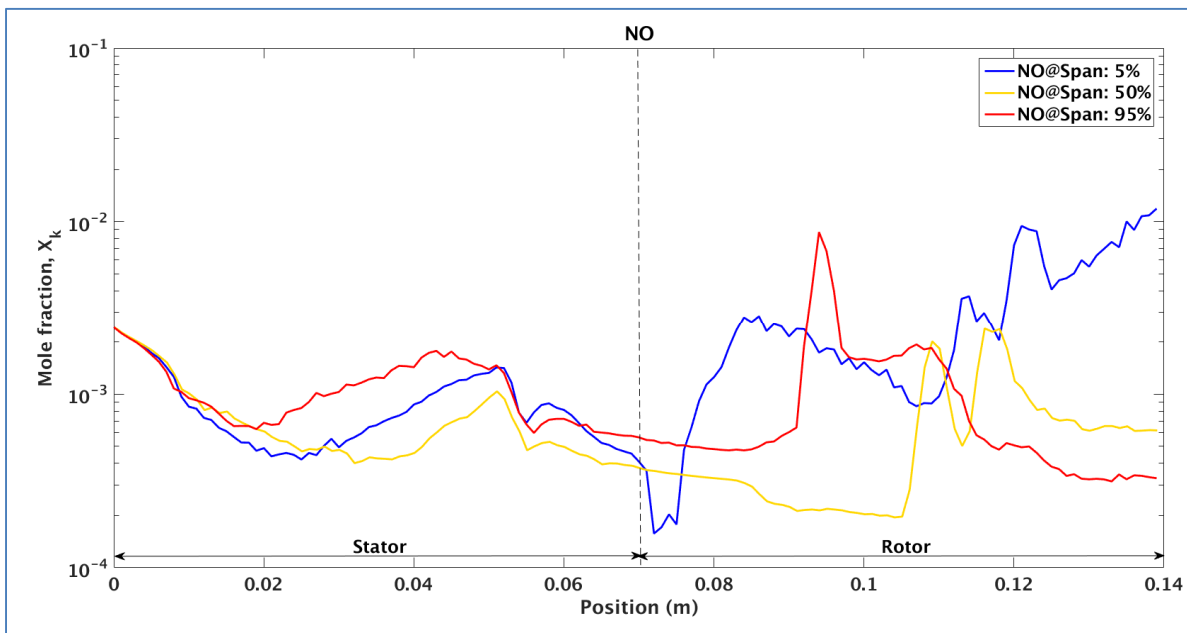


Figure 5.12 NO evolutions at the 5 %, 50 %, and 95 % span

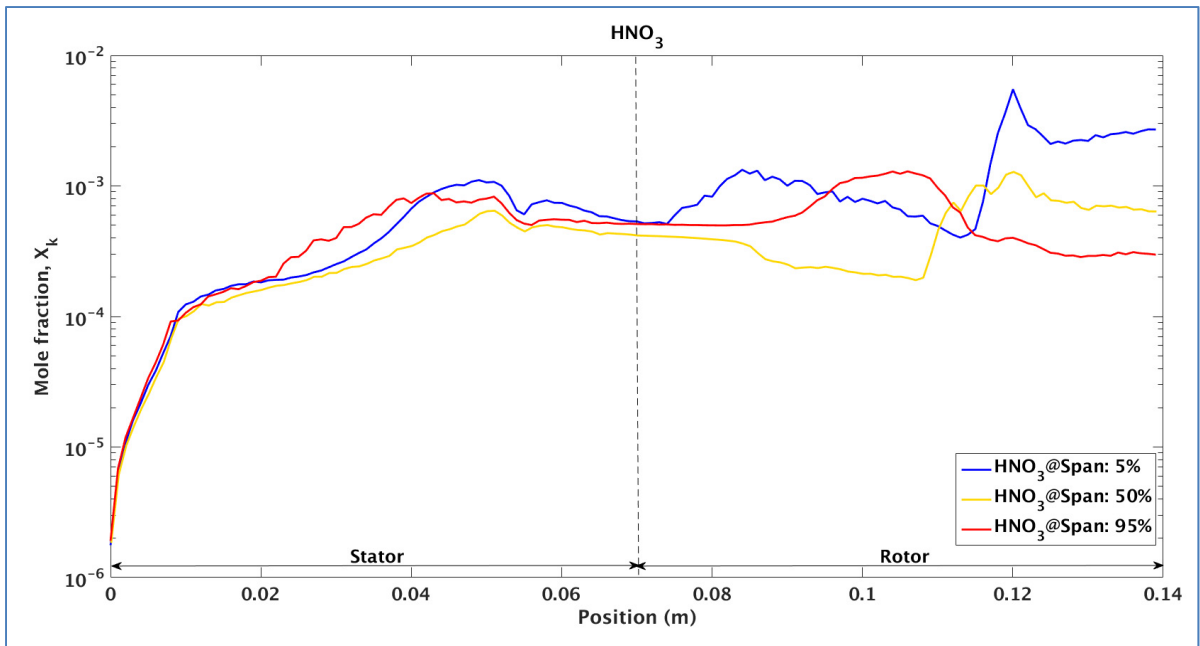


Figure 5.13 HNO_3 evolution at the 5 %, 50 %, and 95 % span

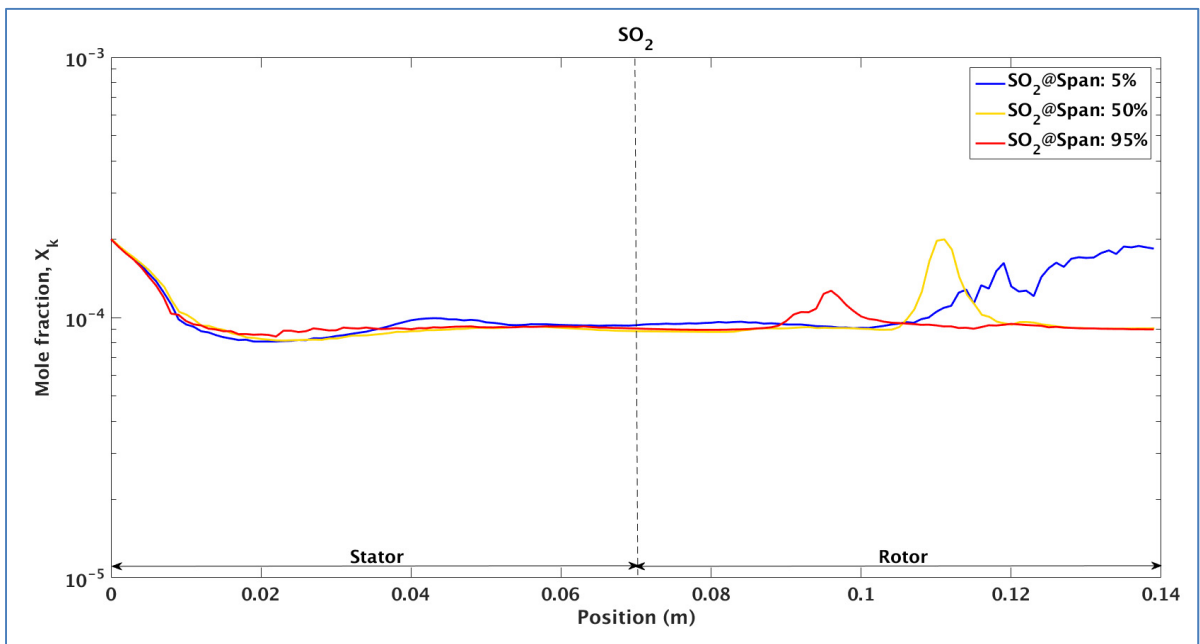


Figure 5.14 SO_2 evolution at the 5 %, 50 %, and 95 % span

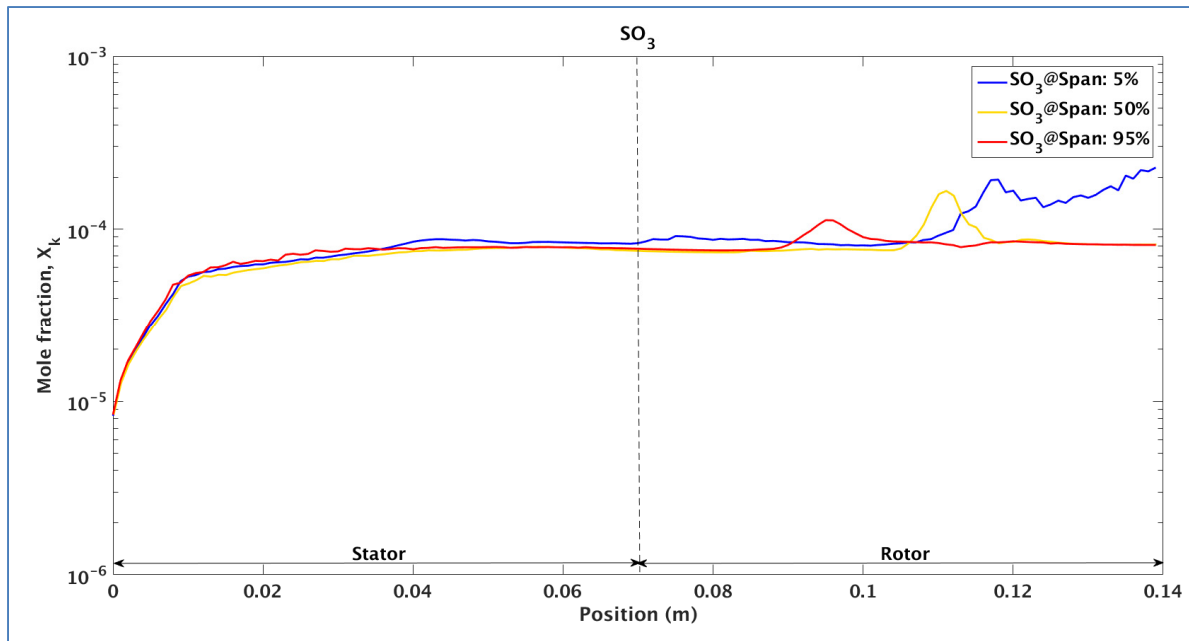
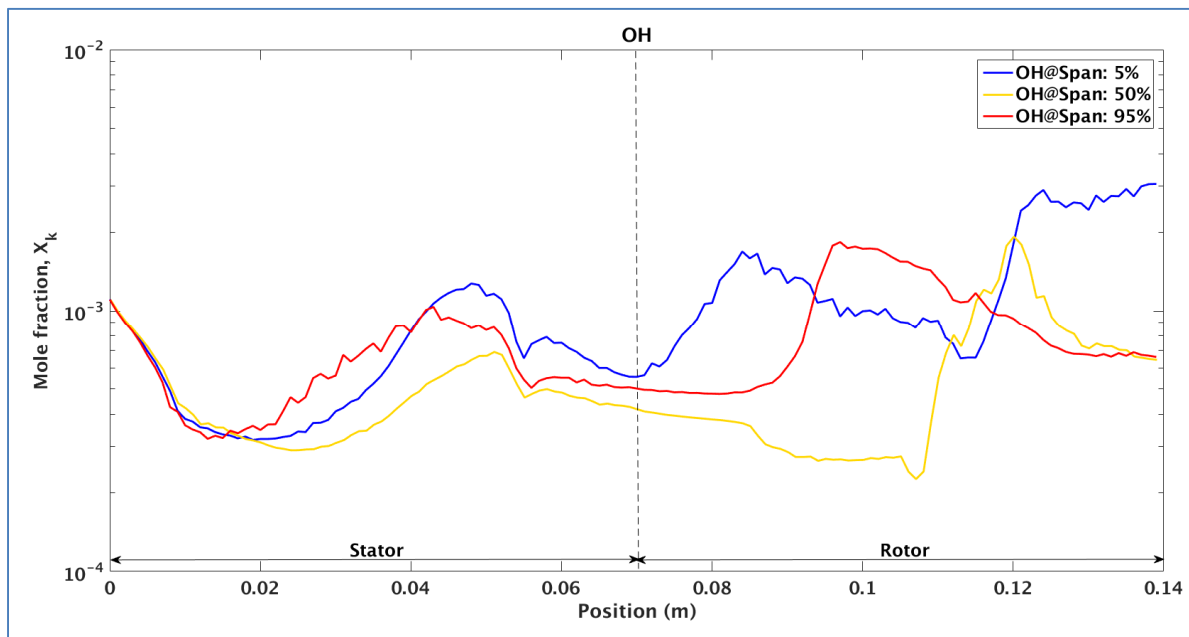
Figure 5.15 SO_3 evolution at the 5 %, 50 %, and 95 % span

Figure 5.16 OH evolution at the 5 %, 50 %, and 95 % span

Basing on creative matrixes of mole fractions of species in the 3-D simulation, we can compare the averaged mole fractions between 2-D and 3-D calculations. Table 5.2 exhibits averaged mole fractions of species at the turbine outlet in two cases: 2-D calculation at the 50 % span and 3-D calculation. Then this Table also shows the difference of mole fraction results of species at the HPT outlet in two calculations. It is observed that if 2-D calculation can perform relatively well the evolution of CO₂, N₂, SO₂ and SO₃, the difference of mole fractions of H₂O, NO, HNO₃ and OH between 2-D and 3-D calculations may be underpredicted by 90.7 % and most of which is due to the poor prediction of H₂O by the 2-D solution.

Table 5.1 Inlet to outlet comparisons of \overline{X}_k for 1-D estimations, X_k for 2-D solutions

Species ^a	1-D estimations and 2-D solutions	
	At turbine outlet, X_k , Maximum % difference	Over rotor blade, X_k , Maximum % difference
CO ₂	2.1	5.3
H ₂ O	5.0	75.6
N ₂	3.6	44.1
NO	16.4	32.9
SO ₂	0.6	52.4
HNO ₃	7.4	31.6
SO ₃	0.1	47.1
OH	7.7	21.7

^aOne dimensional/two dimensional initial/inlet speciations are the same

Thus, these results indicate that 1-D estimation can perform relatively well the trend of mole fraction evolutions of species; 2-D solution can give the useful information of these evolutions in the 2-D surface but some nonuniformity impacts cannot be adequately captured through current 1-D and 2-D solutions. Additionally, 3-D calculation can give full information about these evolutions at every region in the space, full information of 3-D

geometry effects, influence of rotor speed on the different radical positions and influence of nonuniformities of aerothermodynamic parameters (temperature, pressure and velocity of flow) on the chemical transformation of aerosol gases. With the complex flow and the complex chemical transformations in some parts of aircraft engine such as the HPT, 3-D calculation is significant to calculate these processes.

Table 5.2 Inlet to outlet comparisons of \overline{X}_k for 2-D simulation and \overline{X}_k for 3-D turbine calculations

Species ^a	2-D solutions, Outlet plane result, \overline{X}_k	3D solutions, Outlet plane result, \overline{X}_k	Outlet plane result, \overline{X}_k , % difference
CO ₂	9.58E-01	9.36E-01	2.3
H ₂ O	6.12E-04	6.59E-03	90.7
N ₂	2.81E-02	2.96E-02	5.1
NO	6.25E-04	1.86E-03	66.4
SO ₂	9.19E-05	1.12E-04	17.9
HNO ₃	6.37E-04	1.16E-03	45.1
SO ₃	8.30E-05	1.00E-04	17.0
OH	6.55E-04	8.74E-04	25.1

^aTwo dimensional/three dimensional initial/inlet speciations are the same

5.4 Conclusion

The transformation of aerosol precursor emissions of pollutants and other gas species (hydrogen, oxygen species and carbon oxides) in the high pressure turbine of an aircraft engine has been simulated. The model simulates the evolution of principal precursor pollutant gases (NO_x and SO_x) and other species (hydrogen, oxygen species and carbon oxides). The turbine flow is computed with a 3-D flow model. This is the first published model study of 3-D chemical formations inside a high pressure turbine and for the first time

to compare three numerical solutions (1-D, 2-D and 3-D calculations) of transformation of trace species inside an aircraft engine.

The 1-D estimation and 2-D calculations have served as a method of identifying the general trend in chemical evolution and the trend of distribution of species in a 2-D surface through the turbine and have established several conclusions of interest: 1) Temperature and mixed dilution are the primary factors influencing turbine chemistry, especially at the high temperature near the turbine inlet and the mixed dilution at the rotor blade trailing edge; 2) The formation of NO_x , SO_x , CO_x families through oxidation processes (OH and O) is a key factor in determining the chemical process within the HPT; 3) The nonuniformity of flow parameters may constitute a mechanism that has significance on the chemical formation of trace species in the turbine. These 1-D and 2-D calculations also show that the formation of NO_x and SO_x is characterized by the two important conversions of NO and SO_2 to NO_2 and SO_3 . Quantitatively, the ratios of two conversions ($X_{\text{NO}_2} / X_{\text{NO}_x}$ and $X_{\text{SO}_3} / X_{\text{SO}_x}$) were calculated; $X_{\text{NO}_2} / X_{\text{NO}_x}$ increases from 9.6 % at turbine inlet to 17.8 % at the turbine outlet and $X_{\text{SO}_3} / X_{\text{SO}_x}$ changes from 3.03 % to 33.2 % in the HPT.

Our results also indicated strong dissimilarities in chemical transformations of 3-D calculations. In 3-D calculations, the effects of spatial geometry, rotor speed and nonuniformities of flow enhance significantly the productions of aerosol precursors. In comparison between 1-D, 2-D and 3-D simulations, results show that the difference of mole fractions of species can be underpredicted by 75.6 % between 1-D and 2-D calculations and for the comparison of 2-D and 3-D calculation, the underpredicted difference may be 90.7 %.

This paper is a continuation and extension of earlier works that the author and the co-workers realized to study the aero-thermodynamic processes in the HPT. We bring the useful information and new insights to better understand the chemical transformation in the HPT. The results issued from this work can be used for various aircraft engines and help to reduce the avionic emissions for the next generation of aircraft engines.

CONCLUSION AND RECOMMENDATIONS

The research brings herein, for the first time, 3D design of the multi-row HPT, tridimensional calculations and modeling on the aerothermodynamic evolution under various operational conditions (Cruise and Take-Off cycle), new insights into the interactions of aerothermodynamic process and chemical process, 3D chemical formations inside a HPT and first time to compare three numerical solutions based on 1D, 2D and 3D approaches of trace species transformations inside an aircraft engine.

The 3D calculations have established conclusions of interest: i) The aerothermodynamic process always influences the formation of chemical species but the chemical process also has an impact on the flow parameters (value difference of aerothermodynamic parameters with and without chemical reactions may be up to 17 % for temperature and 39 % for velocity of flow). ii) The thermal boundary conditions have strongly affected the temperature (14 %), the rotor speed strongly affected the velocity field (31 %) while the cooling system does not appear to affect the aerothermodynamics fields (about 2 %). iii) Chemically, the 3D simulations show strong nonhomogeneity in chemical transformations throughout the HPT. Comparison of 1D, 2D and 3D approaches, the difference of mole fractions of species could reach 75 % between 1D and 2D calculations and 90 % between 2D and 3D calculations.

This study allowed proper quantification and physico-chemical characterisation of gaseous pollutants in the turbine of an engine aircraft which may affect the atmospheric environment (i.e. climate change and airport air quality). Furthermore, another significant impact of the in-depth knowledge of the aero-thermodynamics fields could be in improving the lifetime of the high-pressure turbine which is known as a critical component of the aircraft engine. Finally, this work provides a better description of the aero-thermodynamical and chemical processes that will assist aircraft engine manufacturers in solving the conflicting goals between the increasing of performance and their environmental impact.

Here are a few recommendations to improve in the future 3D CFD calculations of the turbine:

The geometry of the turbine should be optimized in a future project. In this research, beta, theta or thickness of turbine blades can be modified for finding optimized blade profiles to reduce the pollutants in the HPT .

The turbulent approaches more complex such as LES should be added in the 3D calculations. In that moment, it should find a new method to solve algorithm equations at the zone between stator and rotor ('mixing plane'). Because in the RANS approach, the aerothermodynamic parameters were averaged for the whole plane of 'mixing plane', in the LES, these parameters can be averaged for every element at the 'mixing plane' and it should find a way to reduce the calculation time of super-computer.

The study of chemical process should be extended with a more complex chemical kinetic (more chemical reactions and more species) at high temperature and pressure to increase the precision of investigation.

Finally, a simulation of high pressure turbine and low pressure turbine multi-stages should be performed and studied to have a complete vision of aero-thermodynamic and chemical transformations in the complete turbine. This is an important step contributing to the simulation of complete aircraft engine.

LIST OF BIBLIOGRAPHICAL REFERENCES

1. Hofmann, D.J. (1991), *Aircraft Sulfur Emissions*. Nature, **349**(6311): p. 659-659.
2. Jones, S., et al. (2015), *The application of magnetic measurements for the characterization of atmospheric particulate pollution within the airport environment*. Science of the Total Environment, **502**: p. 385-390.
3. Harrison, R.M., M. Masiol, and S. Vardoulakis (2015), *Civil aviation, air pollution and human health*. Environmental Research Letters, **10**(4): p. 041001.
4. Starik, A.M., et al. (2002), *Modeling of sulfur gases and chemiions in aircraft engines*. Aerospace Science and Technology, **6**(1): p. 63-81.
5. Lukachko, S.P., et al. (2008), *Engine design and operational impacts on particulate matter precursor emissions*. Journal of Engineering for Gas Turbines and Power, **130**(2): p. 021505.
6. Lukachko, S.P., et al. (1998), *Production of sulfate aerosol precursors in the turbine and exhaust nozzle of an aircraft engine*. Journal of Geophysical Research-Atmospheres, **103**(D13): p. 16159-16174.
7. Rose, M., P. Schüpbach, and M. Mansour (2013), *The Thermodynamics of Wake Blade Interaction in Axial Flow Turbines: Combined Experimental and Computational Study*. Journal of Turbomachinery, **135**(3): p. 031015.
8. Lampart, P., S. Yershov, and A. Rusanov (2005), *Increasing flow efficiency of high-pressure and low-pressure steam turbine stages from numerical optimization of 3D blading*. Engineering optimization, **37**(2): p. 145-166.
9. Yılmaz, İ. (2009), *Evaluation of the relationship between exhaust gas temperature and operational parameters in CFM56-7B engines*. Proceedings of the Institution of Mechanical Engineers, Part G: Journal of Aerospace Engineering, **223**(4): p. 433-440.
10. Wey, C., et al. (NASA Glen Research Center TM-2006-214382, Cleveland, OH, 2006), *Aircraft particle emissions experiment (APEX)*.
11. Wey, C.C., et al. (2007), *Overview on the aircraft particle emissions experiment*. Journal of Propulsion and Power, **23**(5): p. 898-905.
12. Moniruzzaman, C.G. and F. Yu (2012), *A 0D aircraft engine emission model with detailed chemistry and soot microphysics*. Combustion and Flame, **159**(4): p. 1670-1686.

13. Bisson, J., et al. (2016), *Numerical Prediction of Gaseous Aerosol Precursors and Particles in an Aircraft Engine*. Journal of Propulsion and Power: p. 1-11.
14. Starik, A.M., et al. (2013), *Impact of operating regime on aviation engine emissions: Modeling study*. Journal of Propulsion and Power, **29**(3): p. 709-717.
15. Jones, R.E. (1978), *Gas turbine engine emissions—Problems, progress and future*. Progress in Energy and Combustion Science, **4**(2): p. 73-113.
16. Brown, R., et al. (1996), *Aircraft exhaust sulfur emissions*. Geophysical research letters, **23**(24): p. 3603-3606.
17. Wong, H.W., et al. (2011), *Design Parameters for an Aircraft Engine Exit Plane Particle Sampling System*. Journal of Engineering for Gas Turbines and Power-Transactions of the Asme, **133**(2).
18. Durbin, P. (1995), *Separated flow computations with the k-epsilon-v-squared model*. AIAA journal, **33**(4): p. 659-664.
19. Spalart, P.R. (2000), *Strategies for turbulence modelling and simulations*. International Journal of Heat and Fluid Flow, **21**(3): p. 252-263.
20. Guntupalli, K. (2011), *Development, validation and verification of the Momentum Source Model for discrete rotor blades*.
21. Rajagopalan, R.G. and S.R. Mathur (1993), *Three dimensional analysis of a rotor in forward flight*. Journal of the American Helicopter Society, **38**(3): p. 14-25.
22. LEW†, A.J., G.C. Buscaglia, and P.M. Carrica (2001), *A Note on the Numerical Treatment of the k-epsilon Turbulence Model**. International Journal of Computational Fluid Dynamics, **14**(3): p. 201-209.
23. Kersken, H.-P., et al. (2012), *Time-linearized and time-accurate 3D RANS methods for aeroelastic analysis in turbomachinery*. Journal of Turbomachinery, **134**(5): p. 051024.
24. Kersken, H.-P., et al. (2014). *Nonreflecting boundary conditions for aeroelastic analysis in time and frequency domain 3D RANS solvers*. in *ASME Turbo Expo 2014: Turbine Technical Conference and Exposition*. American Society of Mechanical Engineers.
25. Pomraning, E., K. Richards, and P. Senecal (2014), *Modeling turbulent combustion using a RANS model, detailed chemistry, and adaptive mesh refinement*, SAE Technical Paper.
26. Tucker, P. (2013), *Trends in turbomachinery turbulence treatments*. Progress in Aerospace Sciences, **63**: p. 1-32.

27. Foroutan, H. and S. Yavuzkurt (2013), *A Model for Simulation of Turbulent Flow With High Free Stream Turbulence Implemented in OpenFOAM®*. Journal of Turbomachinery, **135**(3): p. 031022.
28. Saad, Y. (2003), *Iterative methods for sparse linear systems*: SIAM.
29. Buekens, A. (2002), *Combustion: Physical and Chemical Fundamentals, Modeling and Simulation, Experiments, Pollutant Formation*. International Journal of Environment & Pollution, **17**(3): p. 291-291.
30. Kee, R.J., et al. (1986), *A Fortran computer code package for the evaluation of gas-phase multicomponent transport properties*. Sandia National Laboratories Report SAND86-8246, **13**: p. 80401-1887.
31. Mason, E. and L. Monchick (1962), *Transport Properties of Polar-Gas Mixtures*. The Journal of Chemical Physics, **36**(10): p. 2746-2757.
32. Coull, J.D., N.R. Atkins, and H.P. Hodson (2014), *Winglets for Improved Aerothermal Performance of High Pressure Turbines*. Journal of Turbomachinery, **136**(9): p. 091007.
33. Demeulenaere, A. and R. Van den Braembussche (1996). *Three-dimensional inverse method for turbomachinery blading design*. in *ASME 1996 International Gas Turbine and Aeroengine Congress and Exhibition*. American Society of Mechanical Engineers.
34. Yershov, S. and A. Rusanov (1996), *The application package FlowER for the calculation of 3D viscous flows through multistage turbomachinery*. Certificate of state registration of copyright, Ukrainian state agency of copyright and related rights, February, **19**.
35. Yershov, S., et al. (1998), *Numerical simulation of 3D flow in axial turbomachines*. Task Quarterly, **2**(2): p. 319-347.
36. Denton, J. and W. Dawes (1998), *Computational fluid dynamics for turbomachinery design*. Proceedings of the Institution of Mechanical Engineers, Part C: Journal of Mechanical Engineering Science, **213**(2): p. 107-124.
37. Dornberger, R., et al. (2000), *Multidisciplinary turbomachinery blade design optimization*. AIAA paper, **838**: p. 2000.
38. Ashihara, K. and A. Goto (2001). *Turbomachinery blade design using 3-D inverse design method, CFD and optimization algorithm*. in *ASME Turbo Expo 2001: Power for Land, Sea, and Air*. American Society of Mechanical Engineers.

39. Susan-Resiga, R., S. Muntean, and A. Bosioc (2008). *Blade Design for Swirling Flow Generator*. in *Proceedings of the 4th German–Romanian Workshop on Turbomachinery Hydrodynamics (GRoWTH)*.
40. Koini, G.N., S.S. Sarakinos, and I.K. Nikolos (2009), *A software tool for parametric design of turbomachinery blades*. *Advances in Engineering Software*, **40**(1): p. 41-51.
41. Korakianitis, T., et al. (2012), *Design of high-efficiency turbomachinery blades for energy conversion devices with the three-dimensional prescribed surface curvature distribution blade design (CIRCLE) method*. *applied Energy*, **89**(1): p. 215-227.
42. Grindle, T.J. and F.W. Burcham Jr (2003), *Engine damage to a NASA DC-8-72 airplane from a high-altitude encounter with a diffuse volcanic ash cloud*.
43. Nijdam, T. and R.v. Gestel (2011), *Service experience with single crystal superalloys for high pressure turbine shrouds*.
44. Yu, G., C. Xin-feng, and L. Nan), *Failure Analysis on HPT Blade of CFM56-7B*.
45. Hall, K.C., et al. (2013), *Harmonic balance methods applied to computational fluid dynamics problems*. *International Journal of Computational Fluid Dynamics*, **27**(2): p. 52-67.
46. Erdos, J.I., E. Alzner, and W. McNally (1977), *Numerical solution of periodic transonic flow through a fan stage*. *AIAA journal*, **15**(11): p. 1559-1568.
47. Gerolymos, G., G. Michon, and J. Neubauer (2002), *Analysis and application of chorochronic periodicity in turbomachinery rotor/stator interaction computations*. *Journal of Propulsion and Power*, **18**(6): p. 1139-1152.
48. Montomoli, F., H. Hodson, and L. Lapworth (2011), *RANS–URANS in axial compressor, a design methodology*. *Proceedings of the Institution of Mechanical Engineers, Part A: Journal of Power and Energy*, **225**(3): p. 363-374.
49. Giles, M.B. (1988), *Calculation of unsteady wake/rotor interaction*. *Journal of Propulsion and Power*, **4**(4): p. 356-362.
50. Giles, M. (1991), *Unsflo: A numerical method for the calculation of unsteady flow in turbomachinery*: Citeseer.
51. Freitag, L.A. (1997), *On combining Laplacian and optimization-based mesh smoothing techniques*. *ASME APPLIED MECHANICS DIVISION-PUBLICATIONS-AMD*, **220**: p. 37-44.

52. Batdorf, M., L.A. Freitag, and C. Ollivier-Gooch (1997). *Computational study of the effect of unstructured mesh quality on solution efficiency*. in *Proc. 13th AIAA Computational Fluid Dynamics Conf.*
53. Brewer, M.L., et al. (2003). *The Mesquite Mesh Quality Improvement Toolkit*. in *IMR*.
54. Zhang, Y., C. Bajaj, and B.-S. Sohn (2005), *3D finite element meshing from imaging data*. *Computer methods in applied mechanics and engineering*, **194**(48): p. 5083-5106.
55. Zhang, Y. and C. Bajaj (2006), *Adaptive and quality quadrilateral/hexahedral meshing from volumetric data*. *Computer methods in applied mechanics and engineering*, **195**(9): p. 942-960.
56. Brummell, N.H., N.E. Hurlburt, and J. Toomre (1998), *Turbulent compressible convection with rotation. II. Mean flows and differential rotation*. *The Astrophysical Journal*, **493**(2): p. 955.
57. Sotensen, J.N.r. and W.Z. Shen (2002), *Numerical modeling of wind turbine wakes*. *Journal of fluids engineering*, **124**(2): p. 393-399.
58. Shyy, W., S. Thakur, and J. Wright (1992), *Second-order upwind and central difference schemes for recirculating flow computation*. *AIAA journal*, **30**(4): p. 923-932.
59. Schumann, U. (1995), *The impact of NOX emissions from aircraft upon the atmosphere at flight altitudes 8–15 km (AERONOX)*. CEC Report.
60. Goldstein, M.a.J.R.H.), “*Boundary Conditions for the Diffusion Solution of Coupled Conduction-Radiation Problems*”, in *NASA Technical Note, NASA TN D-4618*.
61. Dakhel, P.M., et al. (2005), *Post-combustion evolution of soot properties in an aircraft engine*. *Proceedings of the ASME Turbo Expo 2005, Vol 2*: p. 787-795.
62. Mueller, M., R. Yetter, and F. Dryer (2000), *Kinetic modeling of the CO/H₂O/O₂/NO/SO₂ system: Implications for high-pressure fall-off in the SO₂+ O (+ M)= SO₃ (+ M) reaction*. *International Journal of Chemical Kinetics*, **32**(6): p. 317-339.
63. Westley, F., J. Herron, and R. Cvetanovic (1987), *Compilation of chemical kinetic data for combustion chemistry. Part 2. Non-aromatic C, H, O, N, and S containing compounds (1983)*, National Bureau of Standards, Washington, DC (USA). Chemical Kinetics Div.

64. Tsang, W. and R. Hampson (1986), *Chemical kinetic data base for combustion chemistry. Part I. Methane and related compounds*. Journal of Physical and Chemical Reference Data, **15**(3): p. 1087-1279.
65. Tsang, W. and J.T. Herron (1991), *Chemical Kinetic Data-Base for Propellant Combustion .I. Reactions Involving No, No2, Hno, Hno2, Hcn and N2o*. Journal of Physical and Chemical Reference Data, **20**(4): p. 609-663.
66. DeMore, W., et al. (1994), *Chemical kinetics and photochemical data for use in stratospheric modeling, JPL Pub. Evaluation*, (12).
67. Yetter, R.A., et al. (1995), *Development of Gas-Phase Reaction-Mechanisms for Nitramine Combustion*. Journal of Propulsion and Power, **11**(4): p. 683-697.
68. Glarborg, P., et al. (1996), *Impact of SO2 and NO on CO oxidation under post-flame conditions*. International Journal of Chemical Kinetics, **28**(10): p. 773-790.
69. Hunter, S. (1982), *Formation of SO3 in gas turbines*. Journal of Engineering for Power, **104**(1): p. 44-50.
70. Harris, B. (1990), *Conversion of sulfur dioxide to sulfur trioxide in gas turbine exhaust*. Journal of Engineering for Gas Turbines and Power, **112**(4): p. 585-589.
71. Lee, D., et al. (2010), *Transport impacts on atmosphere and climate: Aviation*. Atmospheric Environment, **44**(37): p. 4678-4734.
72. Peeters, P., et al. (2016), *Are technology myths stalling aviation climate policy?* Transportation Research Part D: Transport and Environment, **44**: p. 30-42.
73. Lee, J.J., et al. (2001), *Historical and future trends in aircraft performance, cost, and emissions*. Annual Review of Energy and the Environment, **26**(1): p. 167-200.
74. Timmis, A.J., et al. (2015), *Environmental impact assessment of aviation emission reduction through the implementation of composite materials*. The International Journal of Life Cycle Assessment, **20**(2): p. 233-243.
75. Wong, H.-W., et al. (2008), *Microphysical modeling of ground-level aircraft-emitted aerosol formation: roles of sulfur-containing species*. Journal of Propulsion and Power, **24**(3): p. 590-602.
76. Kärcher, B., et al. (2015), *The microphysical pathway to contrail formation*. Journal of Geophysical Research: Atmospheres, **120**(15): p. 7893-7927.
77. Zhang, C., et al. (2016), *Recent development in studies of alternative jet fuel combustion: Progress, challenges, and opportunities*. Renewable and Sustainable Energy Reviews, **54**: p. 120-138.

78. Wey, C.C., et al. (2007), *Overview on the aircraft particle emissions experiment (APEX)*. Journal of Propulsion and Power, **23**(5): p. 898-905.
79. YERSHOV, S., et al. (1999). *A numerical method for 3D calculations of turbomachinery flows*. in *International symposium on experimental and computational aerothermodynamics of internal flows*.
80. Rose, M., P. Schüpbach, and M. Mansour (2009). *The Thermodynamics of Wake Blade Interaction in Axial Flow Turbines: Combined Experimental and Computational Study*. in *ASME Turbo Expo 2009: Power for Land, Sea, and Air*. American Society of Mechanical Engineers.
81. Gaugler, R. and L. Russell (1984), *Comparison of visualized turbine endwall secondary flows and measured heat transfer patterns*. Journal of Engineering for Gas Turbines and Power, **106**(1): p. 168-172.
82. Strickland, J.H., B.T. Webster, and T. Nguyen (1979), *A Vortex Model of the Darrieus Turbine: An Analytical and Experimental Study*. Journal of fluids engineering, **101**(4): p. 500-505.
83. Goldstein, R.J. and R.A. Spores (1988), *Turbulent Transport on the Endwall in the Region Between Adjacent Turbine Blades*. Journal of Heat Transfer, **110**(4a): p. 862-869.
84. Sieverding, C.H., H. Richard, and J.-M. Desse (2003), *Turbine blade trailing edge flow characteristics at high subsonic outlet mach number*. Journal of Turbomachinery, **125**(2): p. 298-309.
85. Marchal, P. and C. Sieverding (1977), *Secondary flows within turbomachinery bladings*. AGARD Secondary Flows in Turbomachines 20 p(SEE N 78-11083 02-07).
86. Langston, L. (1980), *Crossflows in a turbine cascade passage*. Journal of Engineering for Power, **102**(4): p. 866-874.
87. Sieverding, C. (1985), *Recent progress in the understanding of basic aspects of secondary flows in turbine blade passages*. Journal of Engineering for Gas Turbines and Power, **107**(2): p. 248-257.
88. Sonoda, T. (1985). *Experimental investigation on spatial development of streamwise vortices in a turbine inlet guide vane cascade*. in *ASME 1985 International Gas Turbine Conference and Exhibit*. American Society of Mechanical Engineers.
89. Wei, N. (2000), *Significance of loss models in aerothermodynamic simulation for axial turbines*.

90. Kacker, S. and U. Okapuu (1982), *A mean line prediction method for axial flow turbine efficiency*. Journal of Engineering for Power, **104**(1): p. 111-119.
91. Moustapha, S., S. Kacker, and B. Tremblay (1990), *An improved incidence losses prediction method for turbine airfoils*. Journal of Turbomachinery, **112**(2): p. 267-276.
92. Denton, J.D. (1993). *Loss mechanisms in turbomachines*. in *ASME 1993 International Gas Turbine and Aeroengine Congress and Exposition*. American Society of Mechanical Engineers.
93. Denton, J.D. (1990), *Entropy generation in turbomachinery flows*, SAE Technical Paper.
94. Schobieri, T. and M. Abouelkheir (1992), *Row-by-row off-design performance calculation method for turbines*. Journal of Propulsion and Power, **8**(4): p. 823-828.
95. Okan, M. and D. Gregory-Smith (1992). *A simple method for estimating secondary losses in turbines at the preliminary design stage*. in *ASME 1992 International Gas Turbine and Aeroengine Congress and Exposition*. American Society of Mechanical Engineers.
96. Yaras, M. and S. Sjolander (1990). *Prediction of tip-leakage losses in axial turbines*. in *ASME 1990 International Gas Turbine and Aeroengine Congress and Exposition*. American Society of Mechanical Engineers.
97. De Cecco, S., M. Yaras, and S. Sjolander (1995). *Measurements of the tip-leakage flow in a turbine cascade with large clearances*. in *ASME 1995 International Gas Turbine and Aeroengine Congress and Exposition*. American Society of Mechanical Engineers.
98. Wehner, M., et al. (1997). *Measurement and prediction of tip leakage losses in an axial-flow transonic turbine*. in *ASME 1997 International Gas Turbine and Aeroengine Congress and Exhibition*. American Society of Mechanical Engineers.
99. P. Chaluvadi, V., et al. (2001), *Blade-row interaction in a high-pressure turbine*. Journal of Propulsion and Power, **17**(4): p. 892-901.
100. Hutton, S. (1967), *Introduction to the Theory of Flow Machines*. By A. BETZ. Pergamon 1966. 281 pp. 75s. *Fluid Mechanics of Turbomachinery*. By SL DIXON. Pergamon, 1966. 213 pp. 25s. *Axial Flow Turbines*. By JH HORLOCK. Butterworth, 1966. 275 pp. 97s. 6d. Journal of Fluid Mechanics, **28**(04): p. 824-826.

101. Liebeck, R.H., et al. (1995), *Advanced subsonic airplane design and economic studies*.
102. Lyon, T. and D. Bahr (1981), *CF6-50 Engine Emissions Testing with Traverse Probe*, DTIC Document.
103. Howard, R., J. Wormhoudt, and P. Whitefield (1996), *Experimental characterization of gas turbine emissions at simulated flight altitude conditions*, DTIC Document.
104. Zeschky, J. and H. Gallus (1993), *Effects of stator wakes and spanwise nonuniform inlet conditions on the rotor flow of an axial turbine stage*. Journal of Turbomachinery, **115**(1): p. 128-136.
105. Schulte, P., et al. (1997), *NOx emission indices of subsonic long-range jet aircraft at cruise altitude: In situ measurements and predictions*. Journal of Geophysical Research, **102**: p. 21431-21442.
106. Dhatchanamoorthy, C., et al. (2015), *Study and performance analysis of gas turbine combustion chamber and improving combustion efficiency by using ceramic composite material coating*. International Journal of Mechanical Engineering and Robotics Research, **4**(1): p. 195.
107. Mark, C.P. and A. Selwyn (2016), *Design and analysis of annular combustion chamber of a low bypass turbofan engine in a jet trainer aircraft*. Propulsion and Power Research.
108. Leżański, T., J. Sęczyk, and P. Wolański (2015), *Influence of compression ratio on combustion, turbulence, swirls into model combustion chamber of SI engines*. Journal of KONES, **22**.
109. Anton, N. and W. Wiberg (2013), *Aerodynamic design of a gas turbine rotor blade for the KTH test turbine*. ISRN LUTMDN/TMHP--13/5284--SE.
110. Denton, J. and N. Cumpsty (1987), *Loss Mechanisms in Turbomachines*, ImechE Paper, No. C260/87.
111. Timko, L. (1984), *Energy efficient engine high pressure turbine component test performance report*.
112. Leach, K. (1983, NASA Report No. CR-168189), *Energy efficient engine high-pressure turbine component rig performance test report*.
113. Halila, E., D. Lenahan, and T. Thomas (1982, NASA Report No. CR-167955), *Energy efficient engine high pressure turbine test hardware detailed design report*.

114. Shakariyants, S.A. (PhD thesis, Faculty of Mechanical, Maritime and Materials Engineering, TU Delft, Netherland, 2008), *Generic methods for aero-engine exhaust emission prediction*. .
115. Authority, U.C.A. (2006), *Aircraft Engine Emissions Individual Datasheets*. ICAO Aircraft Engine Emissions Databank at <http://www.caa.co.uk>.
116. Dewangan, R., et al. (2015), *Gas turbines blades- A critical review of failure on first and second stages*. International Journal of Mechanical Engineering and Robotics Research, **4**(1): p. 216.
117. Albert, J.E., D.G. Bogard, and F. Cunha (2004). *Adiabatic and overall effectiveness for a film cooled blade*. in *ASME Turbo Expo 2004: Power for Land, Sea, and Air*. American Society of Mechanical Engineers.
118. Albert, J.E. and D.G. Bogard (2013), *Measurements of Adiabatic Film and Overall Cooling Effectiveness on a Turbine Vane Pressure Side With a Trench*. Journal of Turbomachinery, **135**(5): p. 051007.
119. Ito, S., R. Goldstein, and E. Eckert (1978), *Film cooling of a gas turbine blade*. Journal of Engineering for Power, **100**(3): p. 476-481.
120. Butler, T., et al. (1989), *Redistribution of an inlet temperature distortion in an axial flow turbine stage*. Journal of Propulsion and Power, **5**(1): p. 64-71.
121. Kerrebrock, J.L. and A. Mikolajczak (1970), *Intra-stator transport of rotor wakes and its effect on compressor performance*. Journal of Engineering for Power, **92**(4): p. 359-368.
122. Shang, T. and A.H. Epstein (1997), *Analysis of hot streak effects on turbine rotor heat load*. Journal of Turbomachinery, **119**(3): p. 544-553